PATTERNING AND CHARACTERIZATION APPROACHES OF POLYMER THIN FILMS

A Dissertation

Presented to the Faculty of the Graduate School

of Cornell University

In Partial Fulfillment of the Requirements for the Degree of

Doctor of Philosophy

by

Marvin Young Paik

May 2010

PATTERNING AND CHARACTERIZATION APPROACHES OF POLYMER THIN FILMS

Marvin Young Paik, Ph. D.

Cornell University 2010

Polymers have been used in thin film coatings as a way to produce tailor made surfaces. These thin films have been explored for use in a variety of applications to produce antifouling coatings, corrosion resistant coatings, biocompatible surfaces, and biomedical devices. Polymer brushes, polymer chains tethered to a substrate or surface, synthesized by surface-initiated polymerization have gained significant attention in recent years. As brushes offer a new pathway towards the preparation of functional surfaces and offer long term stability, even in adverse environments, they are attractive for use as high-tech coatings.

Patterned polymer thin films have also seen growing interest for various applications. This dissertation will focus on the top-down direct patterning of polymer brushes and the bottom-up self-assembly of block copolymer thin films. A new approach to creating patterned polymer brushes is highlighted, which is a simpler approach than what is conventionally done. Various polymer brushes were patterned directly using electron beam lithography to create high resolution patterned polymer brushes in a single step. This method was then used to demonstrate the unique ability to create sub-surface patterns within the brush. Additionally, direct patterning was used to create high resolution patterned binary polymer brushes of PMMA and PEGMA. With this binary patterned surface, a surface that responds to its local environment was created.

This thesis also details characterization techniques used in probing polymer thin films to better understand how to improve block copolymer self-assembly. By using a powerful technique called grazing incidence small angle X-ray scattering (GISAXS) on solvent vapor annealed block copolymer thin films while monitoring the solvent vapor swollen film thickness and controlling the film swelling with a nitrogen counterflow, the work presented demonstrates how to accurately determine the processing conditions necessary for the annealing process to take place. This process also provides information as to what changes are occurring during the annealing process. Another characterization technique known as near edge X-ray absorption fine structure (NEXAFS) is also highlighted. A more exact calculation of the electron escape depth (EED) for NEXAFS is done using polymer brushes as the calibration sample. With this information, we can do composition depth profiling on our polymer thin films to identify what is at the surface.

BIOGRAPHICAL SKETCH

Marvin Young Paik spent the majority of his life living in Southern California with his mother and sister. For middle school, he moved to Seoul, South Korea to live with his father, but returned to the U.S three years later and attended high school at Diamond Bar High School. It was there that Marvin was inspired by his teacher, Gloria Putnam, to pursue a career in science. With the support of his friends and family, he started his college life at the University of California at Berkeley and entered into the Department of Physics to begin his formal education in the sciences. While at Berkeley, he began research in a laboratory and was fortunate to join the Experimental Systems Group (ESG) at the Advanced Light Source (ALS) under the guidance of Howard Padmore and Simon Clark. In 2003, Marvin shifted interests towards materials science and was accepted into the Department of Materials Science and Engineering at Cornell University under the supervision of Professor Christopher Ober. During his time in the Ober research group, Marvin's work has focused on the characterization of many different polymer systems, using a wide variety of techniques and tools. After enjoying six and a half years in New York, Marvin now looks to return to the west coast to escape the endless winters of Ithaca and start a new life with his fiancé, Joanna Shi.

To my family and Joanna, for all their support, love, and patience throughout the years.

ACKNOWLEDGMENTS

I would like to thank, first and foremost, my thesis advisor, Professor Christopher Ober for his advice and support during my time at Cornell. I would also like to thank Professor Joel Brock and Professor Ulrich Wiesner for participating on my committee and Professor Emmanuel Giannelis for serving as a proxy for Professor Wiesner in my Master's thesis defense. I would also like to mention that this work was supported in part by the National Science Foundation (NSF) under agreement DMR-0518785 with additional support from the Office of Naval Research (ONR) through award #N00014-02-1-0170.

My appreciation also goes to Sitaraman Krishnan for our countless discussions and his guidance. My thanks also go to Peter Busch and Detlef Smilgies for their help and expertise in X-ray studies carried out at CHESS (Cornell High Energy Synchrotron Source). I would like to thank my friends and family for their love and support. Without them, my life would have been empty and I would never have been able to find the motivation to move forward in life. In particular I'd like to acknowledge my fiancé, Joanna Shi, for the love and patience she has given me. Also, I'd like to thank the entire Ober group, past and present. Everyone has helped mold me into the person I am today. Lastly, I'd am thankful for the opportunities to collaborate and work with people from many different institutions. Thank you everyone once again.

TABLE OF CONTENTS

BIOGRAPHICAL SKETCH iii

DEDICATION iv

ACKNOWLEDGEMENTS v

TABLE OF CONTENTS vi

LIST OF FIGURES ix

LIST OF TABLES xv

CHAPTER 1: BACKGROUND ON POLYMER THIN FILM PATTERNING AND CHARACTERIZATON 1

1.0 Introduction 1

1.1 Polymer Brushes 2

1.1.1 Polymer Brush for Biological Application 3

1.1.2 Polymer Brush for Antifouling Applications 6

1.1.3 Polymer Brush for Electronic Applications 7

1.1.4 Other Polymer Brush Applications 8

1.2 Patterned Polymer Brushes 8

1.2.1 Polymer Brush Patterning Approaches 10

1.3 Polymer Thin Film Characterization 21

1.3.1 GISAXS 21

1.3.2 NEXAFS 30

1.4 Conclusion 35

REFERENCES 36

CHAPTER 2: PATTERNING OF POLYMER BRUSHES – A DIRECT APPROACH TO COMPLEX, 3D STRUCTURES 42

2.0 Introduction 42
2.1 Experimental 45
2.2 Results and Discussion 48
2.3 Conclusion 57
2.4 Acknowledgements 60
REFERENCES 61

CHAPTER 3: DIRECTLY PATTERNED BINARY BRUSHES 64
3.0 Introduction 64
3.1 Experimental 67
3.2 Results and Discussion 70
3.3 Conclusion 75
3.4 Acknowledgements 77
REFERENCES 78

CHAPTER 4: REVERSIBLE MORPHOLOGY CONTROL IN BLOCK COPOLYMER FILMS VIA SOLVENT VAPOR PROCESSING: AN IN-SITU GISAXS STUDY 81
4.0 Introduction 81
4.1 Experimental 83
4.2 Results and Discussion 86
4.2.1 Anneal in THF 88
4.2.2 Anneal in Acetone 95
4.2.3 Reversible Morphology Switching 99
4.3 Conclusion 103
4.4 Acknowledgements 103

REFERENCES 105

CHAPTER 5: DEPTH PROFILING OF POLYMER BRUSHES USING NEAR EDGE X-RAY ABSORPTION FINE STRUCTURE SPECTROSCOPY 109

5.0 Introduction 109

5.1 Experimental 111

5.2 Theory 118

5.3 Results and Discussion 121

5.4 Conclusion 128

5.5 Acknowledgements 132

REFERENCES 133

LIST OF FIGURES

1.1 Graphical representation of the (a) “grafting to” and (b) “grafting from” approaches to polymer brush fabrication. 4

1.2 A combination of contact molding and surface initiated polymerization is presented to manipulate the size and chemistry of nanoscopic features. 9

1.3 Patterned surface-initiated polymerization of sodium acrylate. 12

1.4 Schematic of the parylene patterning used to fabricate patterned polymer brushes. 13

1.5 Binary brush fabrication approach involving the deprotection of the poly(t-butyl acrylate) brush through the photopatterning of a sacrificial photoresist loaded with a photoacid generator. 15

1.6 Polymer brush patterning using electron beam lithography. a) Using e-beam lithography to pattern a resist, backfilled with gold, followed by immobilization of thiol initiator onto the patterned gold arrays. b) Using an e-beam to chemically pattern a SAM, an ATRP initiator is bound to the patterned regions followed by SI-ATRP. 17

1.7 Schematic representation of dip-pen nano-lithography. 18

1.8 Scheme of the microcontact printing polymer brush patterning process. 20

1.9 Magnitude of the electric field inside the scatterer, as a function of angle of incidence. Note that there is significant signal enhancement near the critical angle. 23

1.10 Top) Illustration of the zone casting procedure. Bottom) AFM of the perpendicular lamellae along with the GISAXS scattering images. 25

1.11 The long streaks, also called Bragg rods, are characteristic of perpendicular structures. 26

1.12 a) GISAXS scattering image of hexagonally packed lying cylinders. b) AFM of the lying cylinders displaying the characteristic “fingerprint” pattern. c) Real space model of the hexagonally packed cylinder orientation. d) The expected peak positions from the cylinders modeled in (c). 27

1.13 GISAXS scattering image a) after PLA removal. b) before PLA removal. c) after titanium oxide deposition. (d-f) The corresponding indexed scattered peak positions. 29

1.14 An illustration of the production the fluorescence photons and Auger electrons detected using NEXAFS spectroscopy. 31

1.15 NEXAFS spectra of a two-armed semi-fluorinated liquid crystalline block copolymer. TOP) The partial electron yield reveals the surface composition. BOTTOM) The fluorescence yield details the bulk composition. 32

1.16 NEXAFS spectra of a) PI-F6 before UV exposure. b) PI-F6 during UV exposure. c) PSPI-F6 before UV exposure. d) PSPI-F6 during UV exposure. The peak at 285.5 eV corresponds to the signal from the PS backbone, whereas the peak at 293 eV corresponds to the signal from the fluorinated segment. 34

2.1 Direct patterning of polymer brush procedure compared to conventional lithographic methods. 44

2.2 Normalized thickness vs. electron beam exposure dose of PMMA and PHEMA brushes. 52

2.3 AFM height images of a patterned 19 nm thick PMMA brush. a) 50 nm exposed lines with 100 nm pitch. b) 20 nm exposed lines with a 60 nm pitch. 53

2.4 AFM height images of a patterned 50 nm thick PHEMA brush. a) 200 nm exposed lines with 400 nm pitch. b) 80 nm exposed lines with a 160 nm pitch. 56

2.5 An illustration representing the nano-channel fabrication process with the corresponding surface topography as imaged by AFM. A 200 nm channel with 600 nm pitch was patterned. a) The diblock brush before patterning. b) The diblock brush after electron beam exposure. c) The diblock brush after development. d) The diblock brush after oxygen plasma etching the polystyrene layer away. 58

2.6 a) The PHEMA-*b*-PS diblock brush before patterning. b) 1 μm channels with 1 μm pitch patterned into the diblock brush. c) 300 nm channels with 600 nm pitch patterned into the diblock brush. 59

3.1 Illustration of the patterned binary brush fabrication process. 66

3.2 AFM image of 100 nm lines with 200 nm pitch patterned into a PMMA brush. 72

3.3 Ellipsometric thickness of the PEGMA brush versus polymerization reaction time. A linear increase in brush thickness over time suggests that the brush growth is controlled. 73

3.4 AFM image of the patterned binary PMMA/PEGMA brush. a) The height image shows there is only a slight height difference between the polymer regions. b) The phase image confirms the two regions are two distinct materials. 74

3.5 AFM of 100 nm lines with 200 nm pitch patterned PMMA/PEGMA binary brushes. a,c,e) The height image before, after being immersed in DI water for 30 minutes, and after being sonicated in DI water for 3 hours. b,d,f) The corresponding phase images. 76

4.1 A film of PαMS-*b*-PHOST spin coated from PGMEA. a) The GISAXS profile of the as-spun block copolymer film. The Bragg rods suggests a 87

perpendicular cylindrical morphology, however, the absence of additional ordered peaks indicates short-range ordering of the cylinders. b) The corresponding AFM phase image confirms the morphology. The contrast scale for this image is 10˚.

4.2 In situ swelling of the block copolymer film with THF vapor as seen with GISAXS. a) The first-order peak disappears within 8 minutes of initial swelling suggesting the short range ordering that existed prior to annealing was disrupted during the rapid swelling of the film, and b) no further peaks form even after 20 minutes with a gradual increase in swelling. c) Upon rapid drying of the film, the peaks returns to a standing cylinder morphology, similar to the as-spun film. This behavior indicates that the swelling was insufficient for a change in morphology or orientation. 90

4.3 In situ swelling of the block copolymer thin film with THF vapor to a larger swelling ratio. a) 18 minutes after beginning controlled swelling, the swelling in the film results in a disappearance of Bragg rods, indicating a disordered film. b) As the swelling reaches 200%, peaks form on the Yoneda band in a similar position as the Bragg rods in the as-spun film. c) Upon further swelling, a new set of peaks form, both on the Yoneda and above the Yoneda, while the original peak begins to fade. d) The newly-formed peaks become more intense, while the first peak has fully faded, indicating fully formed morphology with a distinct parallel orientation. e) Quickly drying the film trapped in the swelled morphology and orientation, with the dried GISAXS pattern indicating the formation of parallel cylinders with shrinkage perpendicular to the substrate. f) AFM phase image after THF solvent vapor annealing. A change from perpendicular cylinders to parallel cylinders can be seen. 92

4.4 a-c) In situ swelling of the block copolymer thin film in acetone vapor. Upon swelling to a ratio of 2.47, a change from cylinders to spheres begins. After keeping the film swelled above 360 nm for one hour, individual peaks can be seen indicating a spherical morphology. d) Scattering from the swollen, spherical film along with an overlay of the modeled scattering from a stretched BCC lattice. e) The GISAXS profile of the dried film. Scattering consistent with a FCO spherical morphology is observed. f) AFM height image after processing in acetone vapor. The height scale is 10 nm. 96

4.5 Reversible morphology control through solvent processing as probed in situ and in real time with GISAXS. Thin films with spherical morphology obtained through acetone vapor treatment are shown to transition to parallel cylinders upon THF vapor annealing, and returned to a spherical morphology upon successive exposure to acetone vapor. 101

5.1 Schematic of the experimental geometry. D is the channeltron detector, which is at a fixed angle Δ with respect to the incident X-ray beam. The sample is rotated about an axis normal to the plane of the figure to vary the angle of incidence θ and the emission angle φ. 119

5.2 X-ray reflectivity measurements of the four block copolymer brushes prepared to determine the thicknesses of the PS and PTFEA layers. 122

5.3 High resolution XPS C 1s spectra of the R1 and R3 polymer brushes taken at an emission angle of 0°. The signal at ~293 eV is in good agreement with the characteristic binding energy of the $-CF_3$ group from the PTFEA layer. 125

5.4 Normalized NEXAFS C K-edge spectra of the R1 diblock copolymer brush. 126

5.5 Postedge intensity fitted to Eq 5.14. 127

5.6 Plot of the corrected C1s→π*$_{C=C}$ peak intensity vs $\cos^2\theta$. As the slope of the fit is close to zero, the phenyl groups from the polystyrene layer exhibit no orientational order. 129

5.7 The C1s→π*$_{C=C}$ peak intensity vs $\cos\varphi$. Using an h value of 0.9 gives the best fit curve to the data. 130

5.8 The C1s→σ*$_{C=O}$ peak intensity vs $\cos\varphi$ and the predicted values of a clean PTFEA surface. 131

LIST OF TABLE

1.1 Patterning techniques and bio-related applications. 11

4.1 The in-plane nearest-neighbor distances (nm) of the various self-assembled structures as obtained by AFM and GISAXS. 94

5.1 Thickness measurements of the polystyrene and poly(trifluoroethyl acrylate) layers. 123

CHAPTER 1

BACKGROUND ON POLYMER THIN FILM PATTERNING AND CHARACTERIZATION

1.0 Introduction

Patterning polymer thin films has been of particular interest to academic and industrial scientists as polymers exhibit good mechanical properties, can be engineered to possess specific traits, and are relatively cheap. The unending demand to obtain smaller features, denser packing, and cheaper fabrication has driven researchers to invest significant effort towards making continuous improvements in these areas. Within the last decade alone, rapid development of various strategies used to pattern polymer films has been accomplished.

Patterned polymer surfaces have also seen growing interest for a variety of applications. In the field of electronics, patterned polymers have found uses in organic light emitting diode (OLED) devices,[1, 2] semiconductor microelectronics fabrication,[3-5] and organic photovoltaics.[6] The patterning of polymer surfaces has also been used in bio-related applications such as anti-biofouling coatings,[7] biosensors,[8] and cell growth and adhesion studies.[9-11] Other areas of research dealing with information storage devices,[12] micro-fluidic devices,[13] optical components such as gratings and photonic crystals,[14, 15] and fundamental surface science have involved patterned polymer surfaces as well.

One particular type of polymer surface with unique structure and properties is a polymer brush. Polymer brushes offer the control over chemical functionality and density, improved adhesion stability of the polymer layer, and are well suited for micro- and nano-patterning. These characteristics have made polymer brushes better

suited the thin films used for many of the previously mentioned applications. The following sections of this chapter will provide an overview of polymer brushes, the different approaches towards fabricating patterned polymer brush thin films, and highlight the techniques used to characterize patterned polymer thin films, particularly grazing incidence small angle x-ray scattering (GISAXS) and near edge x-ray absorption fine structure (NEXAFS) spectroscopy. The following chapters will cover a new patterning approach to fabricating patterned polymer brushes, unique structures which can be created with this method, the generation of responsive surfaces using patterned polymer brushes, and the characterization of polymer thin films using GISAXS and NEXAFS.

1.1 Polymer Brushes

Polymer brushes refer to tethered polymer chains that are immobilized to a surface or an interface.[16, 17] This review will focus on end-tethered brushes in which the polymer chain is fixed to a surface at one end. The crowded tethering imparts sufficient constraints on the chains forcing them to stretch away from the surface or interface to avoid overlapping. Generally there are two approaches to fabricating polymer brushes: physisorption and covalent attachment. Polymer brushes manufactured through physisorption usually consists of block copolymers with one block strongly interacting with the surface.[17] However, these types of brushes exhibit poor stability in the presence of heat or a suitable solvent. Also, the grafting density of the chains tends to be relatively low and is limited by the thermodynamic equilibrium of the system. A more robust and stable approach towards making polymer brushes is through the covalent attachment of the chains. Covalent brush attachment can be accomplished through either a "grafting to" or "grafting from" approach,[18] as illustrated in Figure 1.1. In the "grafting to" method, preformed

polymer chain ends react with a reactive group on the substrate to generate polymer brushes with precise control over molecular weight and dispersity.[19] However, the tethering of polymer chains using this approach is limited by steric hindrance. This limitation often leads to brushes with low grafting density. With the "grafting from" method, initiator moieties are first immobilized onto the substrate or interface. These small molecules can be attached to the surface at a much higher density than the bulky polymer chains in the "grafting to" approach. Following initiator immobilization, *in situ* surface initiated polymerization is carried out to generate tethered polymers of high grafting density.[20]

Typically, polymer coatings consist of a tailored layer, designed for a specific application. Initially, these coatings were used as a protective layer towards adverse environmental conditions or to waterproof fabric or wood. Since then, functional coatings have enabled the development and progression of a number of high-tech applications such as microelectronics fabrication, information storage devices and bio-engineered coatings. Polymer brush surfaces have introduced a new approach towards the fabrication of custom surfaces. As these surfaces are chemically anchored to a surface, polymer brushes can be tailored to a range of grafting densities, can be fabricated to thicknesses down the ultra-thin regime, and concerns over exposure to solvents or delamination can be ignored. Polymer brushes first attracted attention in the 1950s when Van der Waarden showed that grafting polymer molecules to colloidal particles helped prevent flocculation.[21] Since then, several different applications have exploited polymer brushes for their surface tunablity potential.

1.1.1 Polymer Brush for Biological Applications

Considerable effort has been made to engineer surfaces possessing good mechanical properties and biocompatibility. In fact, many materials have already been developed; however, there remains plenty of room for improvements. For example,

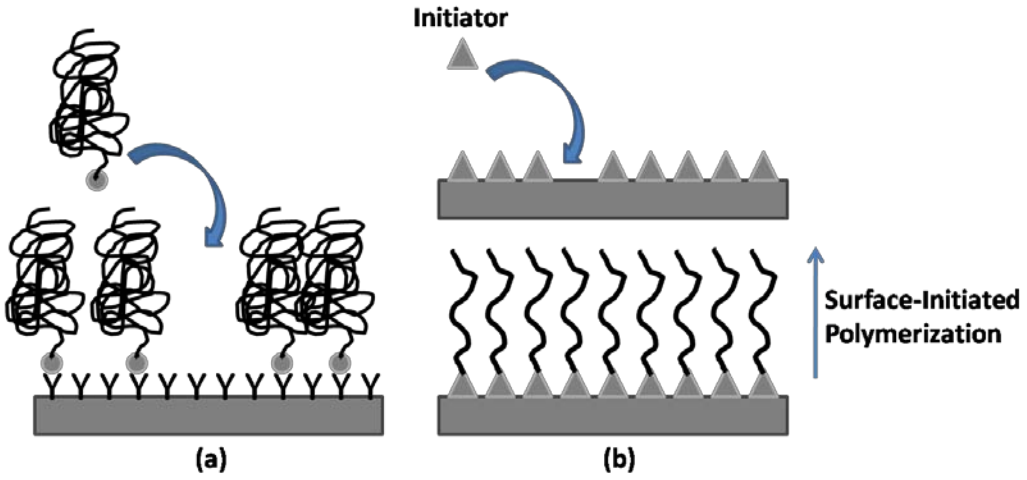

Figure 1.1 Graphical representation of the (a) “grafting to” and (b) “grafting from” approaches to polymer brush fabrication.

poly(vinylidene difluoride) (PVDF) is a biomaterial established for soft tissue applications and used in sutures. This biomaterial's properties make it well suited for this application, but the desire for improved protein and peptide adhesion to promote integrin mediated cell attachment has led researchers to investigate polymer brushes as an approach to tailor the surface for the desired functionality. By growing poly(acrylic acid) brushes on PVDF surfaces via plasma-induced surface initiated polymerization, followed by a conversion of the acid functionalized brush to a fibronectin coated surface, tissue compatibility was achieved. This material was studied by comparative exposure of the modified surface to primary human osteoblasts. Although cell attachment was enhanced on surfaces with physically adsorbed fibronection, enhanced proliferation and survival of the cells was only observed when fibronectin was covalently attached to the surface modified PVDF.[22]

Polymer brushes have recently been considered in the design of smart, or responsive, surfaces. The use of an external stimulus such as temperature, pH, electric field, etc. to change the properties in polymers is an effective approach towards controlling adhesion on surfaces. Temperature responsive polymer brush surfaces were created from poly(N-isopropylacrylamide), NIPPAM, to investigate the effects of surface conformation and wettability changes on the adhesive behavior of adherent inflammatory cells. The grafted poly(NIPPAM) chains pass through their lower critical solution temperature (LCST) and can either expand, creating a hydrophilic surface, or contract, creating a hydrophobic surface. At elevated temperatures, monocyte and macrophages were able to adhere and spread on the hydrophobic surfaces, and the formation of foreign body giant cells (FBGC) were observed). Detachment of these cells was accomplished by lowering the temperature of the polymer brush surface below its LCST, causing a change in the surface conformation

and wettability. This change induced a differential attachment of adherent cells that decreased with time.[23]

1.1.2 Polymer Brush for Antifouling Applications

In a related area, polymer brushes are being explored for use in antifouling applications as well. Concerns over the adhesion of bacteria on material surfaces are of considerable importance in ship hull fouling, medical devices, and membrane filtration systems. In one approach, defense peptides which are secreted by many living organisms exhibit anti-bacterial properties, making them promising in the fight against biofouling. Polymer brushes combining a non-adhesive copolymer of poly(2-(2-methoxyethoxy)ethyl methacrylate-*co*-(hydroxyl terminated oligo(ethylene glycol) methacrylate)) (poly(MEO_2MA-*co*-HOEGMA)) end functionalized with an antimicrobial peptide, magainin I, were studied as they offered the desired surface functionality while possessing the long term stability associated with the mechanical and chemical robustness offered from the brush. The antibacterial activity of the polymer brushes was tested against two strains of Gram positive-bacteria. These surfaces demonstrated a high efficiency in killing all adhered bacterial cells, even for lower grafting ratios in the magainin I peptide tested.[24]

In another approach, Jiang et al. have studied zwitterionic polymer brushes as antifouling surfaces. These surfaces were tested against protein adsorption from solutions of fibrinogen, lysozyme, and blood plasma and serum and were found to be highly resistant to non-specific protein adsorption. Additionally, the brushes exhibited high resistance to bacterial adhesion and biofilm formation.[25] Settlement, growth, and release studies were also done against marine algae. The zwitterionic brush surfaces exhibited very low settlement of the *Ulva* spores, and also low attachment strength of the sporelings (young plants). Testing against *Navicula* diatoms showed excellent antifouling behavior as well.[26] Busscher and coworkers studied the bacterial adhesion

and growth on polymer brush coatings. Using a tri-block copolymer of polyethylene oxide and polypropylene oxide grafted to silicone rubber, they tested three modified and unmodified surfaces with three bacterial strains (Staphylococcus aureus, Staphylococcus epidermidis and Pseudomonas aeruginosa). They observed the polymer brush coatings, compared to the pristine silicone rubber surfaces, reduced the adhesion of the bacteria, retarded the development of the biofilms, and produced an increase in detachment by high fluid shear.[27]

1.1.3 Polymer Brush for Electronic Applications

Polymer brushes have been used as both a conducting an insulating layer. In one application, conductive polymers were grafted to polyethylene and poly(styrenesulfonic) acid films to produce conductive poly(thiophene) and poly(ethylenedioxythiophene) (PEDOT) surfaces.[28, 29] Locklin et al. used catalyst-transfer polycondensation to prepare polymer brushes of poly(phenylene) and poly(thiophene).[30] One strategy towards fabricating conducting polymer and complementary gold microstructures involves the electrodeposition and wet chemical etching of photopatterned polymer brush templates. The polymer brush acts as an insulating layer, allowing the conducting polymer to be grown from the exposed area of the template.[31]

In microelectronics, polymer brushes have been used for a number of purposes as well. Efforts to enable low voltage organic field effect transistor (OFET) operation have been pursued through the use of polymer brushes acting as an ultra-thin gate insulator. Thin gate insulators are required for short channel FETs to operate efficiently, making the tailored growth and uniformity of surface initiated growth of polymer brushes a powerful technique.[32] Another concern in microelectronics is the need to produce smaller and smaller structures. Hawker et al. used surface initiated atom transfer radical polymerization (SI-ATRP) and nitroxide mediated

polymerization (NMP) to grow polymer brushes from nano-patterned surfaces to tune the feature sizes.[33] An illustration of the approach is shown in Figure 1.2.

1.1.4 Other Polymer Brush Applications

The nanoscale control of surface properties which polymer brushes offer have made them attractive for a number of other applications. They have been used in tribology applications, studying the lubrication and friction properties of the modified surfaces under different conditions.[34] Poly(NIPAAM) brushes have been used in cell culture to control the attachment of cells to a surface, followed by release after cooling the brushes below the LCST to cause a conformational surface change.[35] An application involving patterned polymer brushes involves the grafting of polystyrene chains to direct the self-assembly of spun coat PMMA-*b*-PS. By patterning the polymer brush layer, a chemical contrast is created on the substrate. The PMMA block of the spun coat block copolymer then preferentially wets the brush covered areas, driving the self-assembly to a standing orientation. Comparing the self-assembled structures to the chemical pattern, it was possible to increase the density by a factor of four, reduce the size by a factor of two, and significantly enhance the dimensional uniformity .[36] Polymer brushes offer a convenient approach towards tuning surface properties. However, by patterning polymer brushes they can be further exploited as a means of tailoring surface properties of materials for desired shape, functionality, and feature dimensions.

1.2 Patterned Polymer Brushes

Polymer patterning is of particular interest as various functions of polymer-patterned surfaces are being addressed with already existing synthetic and biological polymers and through the design of new polymers as well. Patterning of polymer brush surfaces is an emerging field of nanotechnology and its use is already being

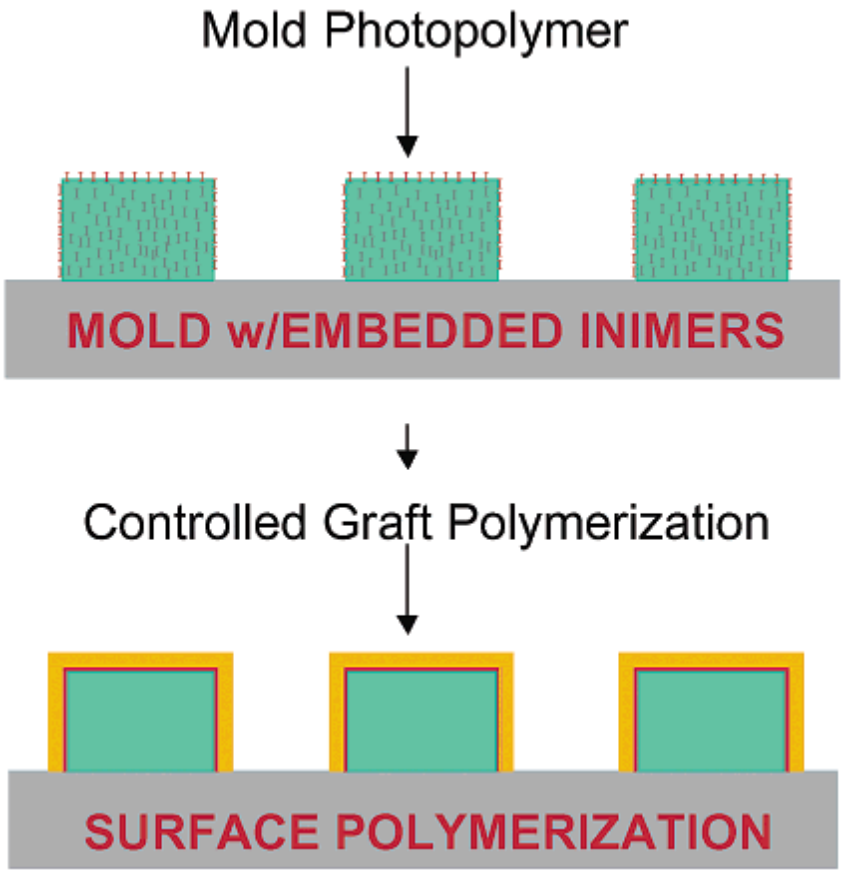

Figure 1.2 A combination of contact molding and surface initiated polymerization is presented to manipulate the size and chemistry of nanoscopic features. (Reprinted from Ref. #33 with permission from the American Chemical Society)

witnessed in a variety of different applications such as bio-selective surfaces,[10] nanofluidic devices,[13] microreaction vessel and drug delivery,[37] biomimetic material fabrication,[38] and cell growth control.[39]. Rapid development of numerous patterning strategies have emerged over the last decade, fulfilling many lithographic requirements demanded from an application.[40] Table 1.1 shows the length scales achievable by the various patterning techniques and the micron or nano-sized features required for different bio-inspired applications. The following section will detail some of the recent advances made in patterned brush surfaces and review some of the various techniques used to fabricate these patterned surfaces.

1.2.1 Polymer Brush Patterning Approaches

One of the most common approaches to fabricating patterned polymer brushes is through photolithography. Photolithography uses radiation to transfer a defined pattern from a photomask to a light sensitive layer (photoresist). In the irradiated areas of the photoresist, a photo-induced chemical reaction occurs that can cause cross-linking or decomposition of the material, resulting in a contrast in developer solubility in the exposed and unexposed regions. Using photolithography, Dong et al. fabricated patterned poly(acrylic acid) (PAA) brushes on a silicon substrate and demonstrated the ability to covalently attach biomolecules to the brush, creating a patterned biofunctional surface. Patterning was done by photo-patterning a photoresist, filling the patterned regions with poly(ethylene glycol) (PEG), followed by stripping the resist. An ATRP initiator was then immobilized onto the unexposed regions, and SI-ARTP was carried out to create patterned sodium acrylate brushes, which were then protonated to create poly(acrylic acid) brushes. Patterns down to 2 μm were achieved.[9] Figure 1.3 shows the photo-patterning process used.

Andruzzi and coworkers used a slightly different approach to fabricate patterned polymer brushes. Figure 1.4 illustrates the patterning method used. Using

Table 1.1 Patterning techniques and bio-related applications. (Table adapted from Ref. #40 with permission from the American Chemical Society)

Patterning Technique	Features	Applications	Substrate
1. Photolithography			
(a) photoresist coated substrate	< 10 μm	Alkyl- and amino-functionalized silanes for controlled cellular growth, protein immobilization and enzymatic assays	Silicon, SiO_x, fused silica, glass
(b) selective chemistry		Protein immobilization	Silicon/gold
2. UV Lithography			
a. deep UV (193 nm) radiation exposure to induce photochemical changes on functional silanes	100 μm	Controlled cell growth on EDA and perfluorinated alkylsilanes	Glass and fused silica
	1 μm	Protein immunoassays on OTMethoxysilane	SiO_x
	25 μm	Thiol-terminated silanes protein immunoassays	SiO_x
	100 μm	Controlled cell growth EDA and OTS	SiO_x
	100 μm	OTS and APTS and chemically modified amine with a synthetic peptide, derived from B2 chain of laminin	SiO_x
b. alkanethiols	208 μm grooves with 42 μm ridges	Biotin-streptavidin recognition using hydroxylated SAMs	Gold
	1 μm	Benzophenone-based SAMs for immunoassays	Gold
c. alkanesiloxanes	3 μm	Photobiotin-based silanized surfaces as immunoassays	SiOx
d.micromanipulation and UV lithography	~ 1 μm	Controlled protein adsorption and cell adhesion R-OEG_n alkane thiols and (R = CH3) and ionic (R = CO_2-, PO_3H-, 2-imidazolo)	Gold
3. microcontact printing	2-80 μm squares	Controlled adsorption of ECM proteins and cells onto patterned SAMs	Gold and silver
	10-90 μm lines	Controlled adsorption of fibronectin onto patterned methyl terminated SAMs	Gold
	5-40 μm squares and circles	Controlled adsorption of ECM proteins and bovine and human endothelial cells	Gold
	25-50 μm ridges and grooves	Fibronectin patterned hexadecanethiol SAMs	Gold
	50 μm lines	Astroglial cells attached selectively EDTA surfaces over OTS	Thin gold film on polyurethane
4. direct evaporation	70 μm	R = NH_2, COOH, and CH_3 for adhesion of embryonic chick dorsal root ganglia (DRG) neurons and PC12h cells	SiOx
5. dip pen	100-350 nm	Proteins adsorbed to MHDA arrays	Gold evaporated on a Petri dish
	Lines and circles	Specific immobilization of cysteine-labeled biomolecules through SAMs	Gold
6. nanoshaving		DNA immobilization through biotin to streptavidin SAMs	Gold
	400 nm x 4 μm trenches	Antibody nanotubes assembled on antigen-SAM arrays	Gold
7. low-energy electron beam lithography	300 nm	Protein patterning using OTS on silicon oxide and MHDA on gold and backfilled with amine-functionalized SAMs	SiO3, gold
8. parylene-based lift-off	~ 1 μm	Patterned RBL cells and bacterial cells	Silicon, glass, gold
9. electron beam lithography	1 μm - < 30 nm	Virus detection using nanoelectromechanical devices	Silicon, gold
10. focused ion beam	50 nm	Nanopipeting DNA/proteins for biological arrays	gold
11. nanoimprinting	75 nm	APTS functionalized with biotin-succinimidyl esters used for streptavidin detection	silicon

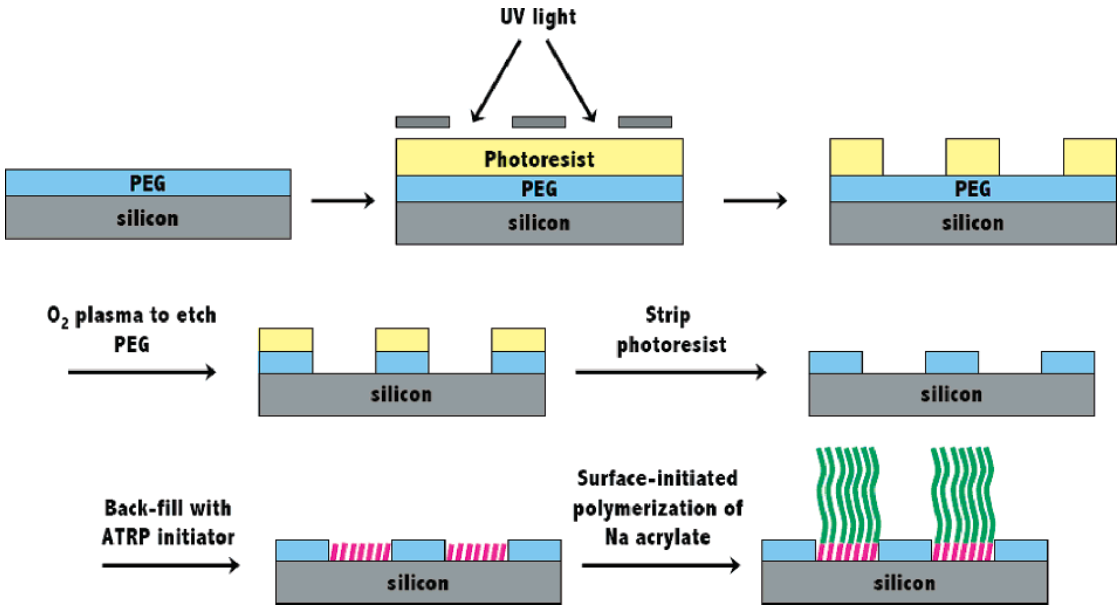

Figure 1.3 Patterned surface-initiated polymerization of sodium acrylate. (Reprinted from Ref. #9 with permission from the American Chemical Society)

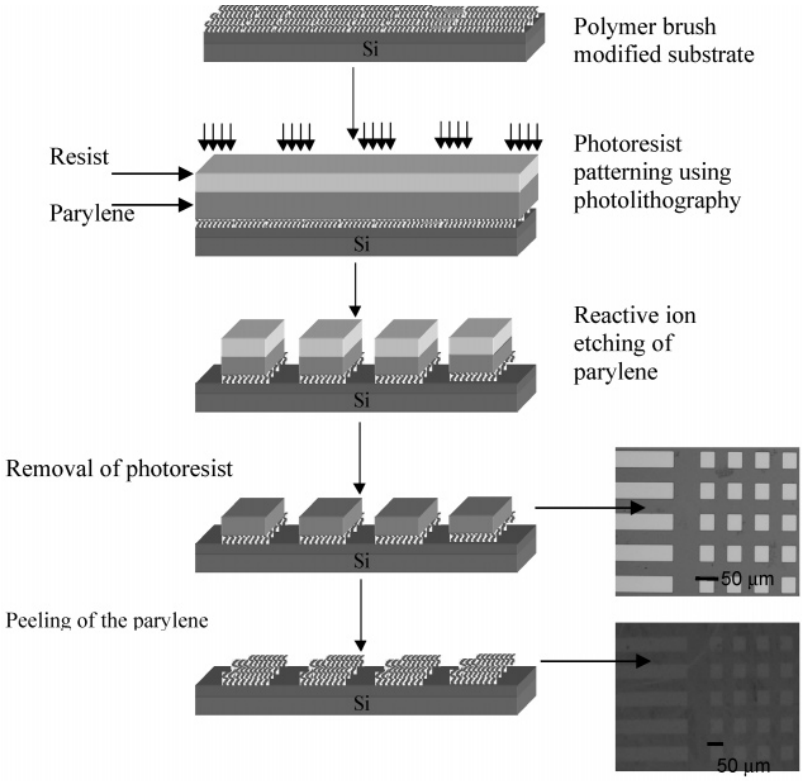

Figure 1.4 Schematic of the parylene patterning used to fabricate patterned polymer brushes. (Adapted from Ref. # 10 with permission from the American Chemical Society)

NMP, they grew brushes from a styrenic monomer containing oligo(ethylene glycol) moieties on a silicon substrate for protein and cell adhesion studies. Patterning of these surfaces was done using a modified photolithographic process involving the chemical vapor deposition of parylene on the brush followed by spin casting a photoresist on top of the parylene layer. The photoresist was then photo-patterned and developed. Reactive ion etching through the patterned resist, parylene and polymer brush was done, and the parylene was peeled away leaving behind a patterned polymer brush surface. Parylene was deposited as it acts as a protective layer for the brush from the patterning and etching process.[10]

A direct patterning process using photolithography was done by Zhou et al. Poly(methyl methacrylate) (PMMA) brushes were grown from a gold substrate to act as a thin dielectric and etch resistant layer. The brushes were then exposed to UV light through a mask for 6 hours to produce UV patterned PMMA brushes.[31] This approach was extended to produce binary brushes with patterned regions of PMMA and poly(2-hydroxyethyl methacrylate).[41] An alternate method to making binary patterned brushes using photolithography was demonstrated by Hawker and coworkers, as shown in Figure 1.5. They used NMP to grow poly(t-butyl acrylate) from a silicon substrate and spin coated a photoresist loaded with a photoacid generator (PAG). The PAG would generate acid in the exposed regions and would transfer to the polymer brush layer, deprotecting the tert-butyl ester group, converting the polymer to poly(acrylic acid). Upon stripping the resist, a patterned binary brush of poly(t-butyl acrylate) and PAA would remain.[42]

Another common approach towards patterning brushes is through electron beam lithography. This technique uses a high energy, focused electron beam to perform “direct patterning”. Although this method is a point-by-point patterning method, which can increase the patterning time significantly, it offers the benefit of

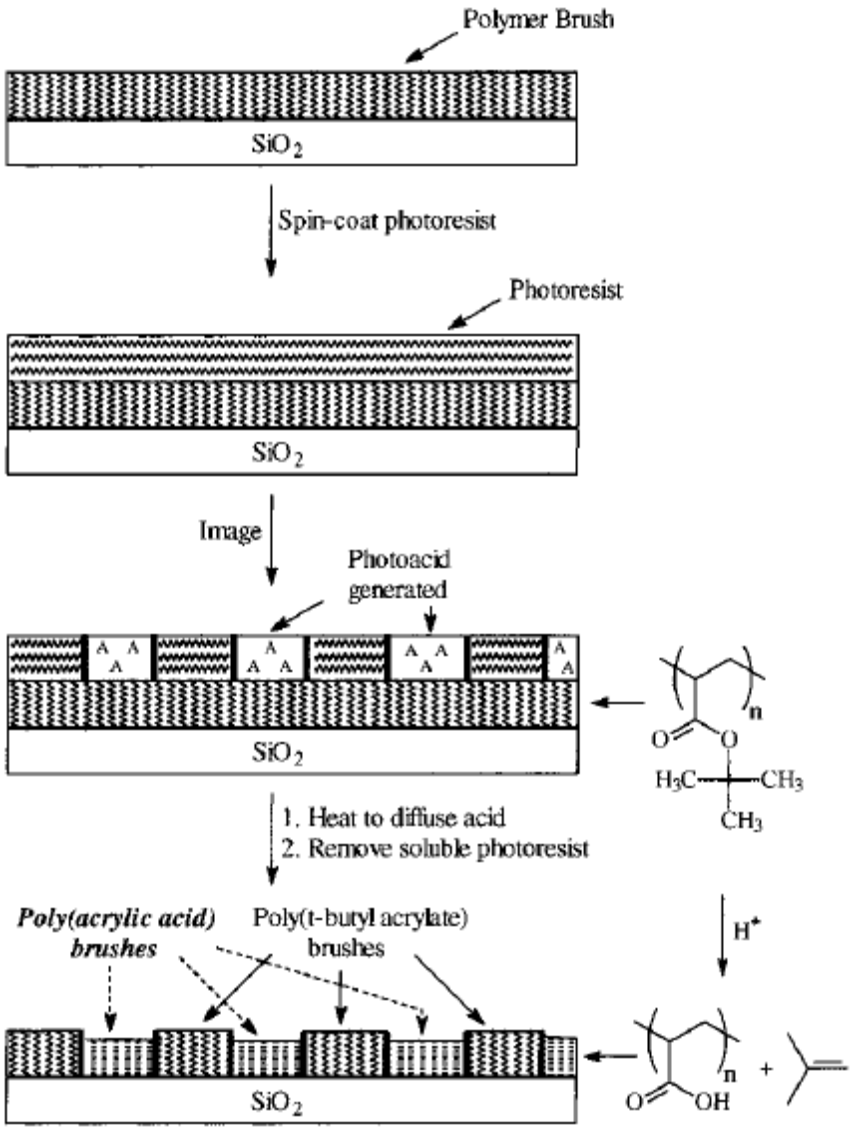

Figure 1.5 Binary brush fabrication approach involving the deprotection of the poly(t-butyl acrylate) brush through the photopatterning of a sacrificial photoresist loaded with a photoacid generator. (Reprinted from Ref. # 42 with permission from the American Chemical Society)

very high resolution patterning. Zauscher et al. used electron beam lithography write a pattern into spin coated PMMA, which was then developed, followed with deposition of gold into the patterned trenches, and stripped. A thiol ATRP initiator was then immobilized onto the patterned gold arrays and surface initiated polymerization of NIPAAM was carried out to create a patterned poly(NIPAAM).brush surface.[43] The patterning scheme is shown in Figure 1.6a.

A more direct approach to patterning brushes using electron beam lithography was done by Ulman and coworkers. Patterned polystyrene brushes were fabricated through the electron beam irradiation of self-assembled monolayers (SAMs) of 4'-nitro-1,1'-biphenyl-4-thiol (NBT). Upon e-beam exposure, NBT would cause the reduction of the nitro functionalities to amino groups, while the aromatic biphenyl layer is dehydrogenated and cross-linked. The amino groups of this chemically patterned surface were then derivatized to initiate the surface initiated polymerization of styrene. With this approach 70 nm isolated lines were obtained, although the required dose for successful irradiation of the NBT SAMs was 20,000 $\mu C/cm^2$ at 50 eV and 40,000 $\mu C/cm^2$ at 300 eV.[44] The reaction scheme of the NBT patterning and SIP of styrene is shown in Figure 1.6b.

Another "direct" patterning approach involves the use of dip-pen nanolithography (DPN). DPN was first established by Mirkin and coworkers. The DPN patterning technique is outlined in Figure 1.7. The process uses an atomic form microscope (AFM) tip as the "nib", dipped in a solution of molecules to be immobilized ("ink") which are then "written" onto a substrate ("paper"). By using capillary transport of the molecules from the AFM to the substrate, they managed to immobilize and directly write patterns of alkanethiols onto gold with linewidths as small as 30 nm.[45] This technique was extended by the same group to produce patterned polymer brush surfaces. 10-(Exo-5-norbornen-2oxy)decane-1-thiol

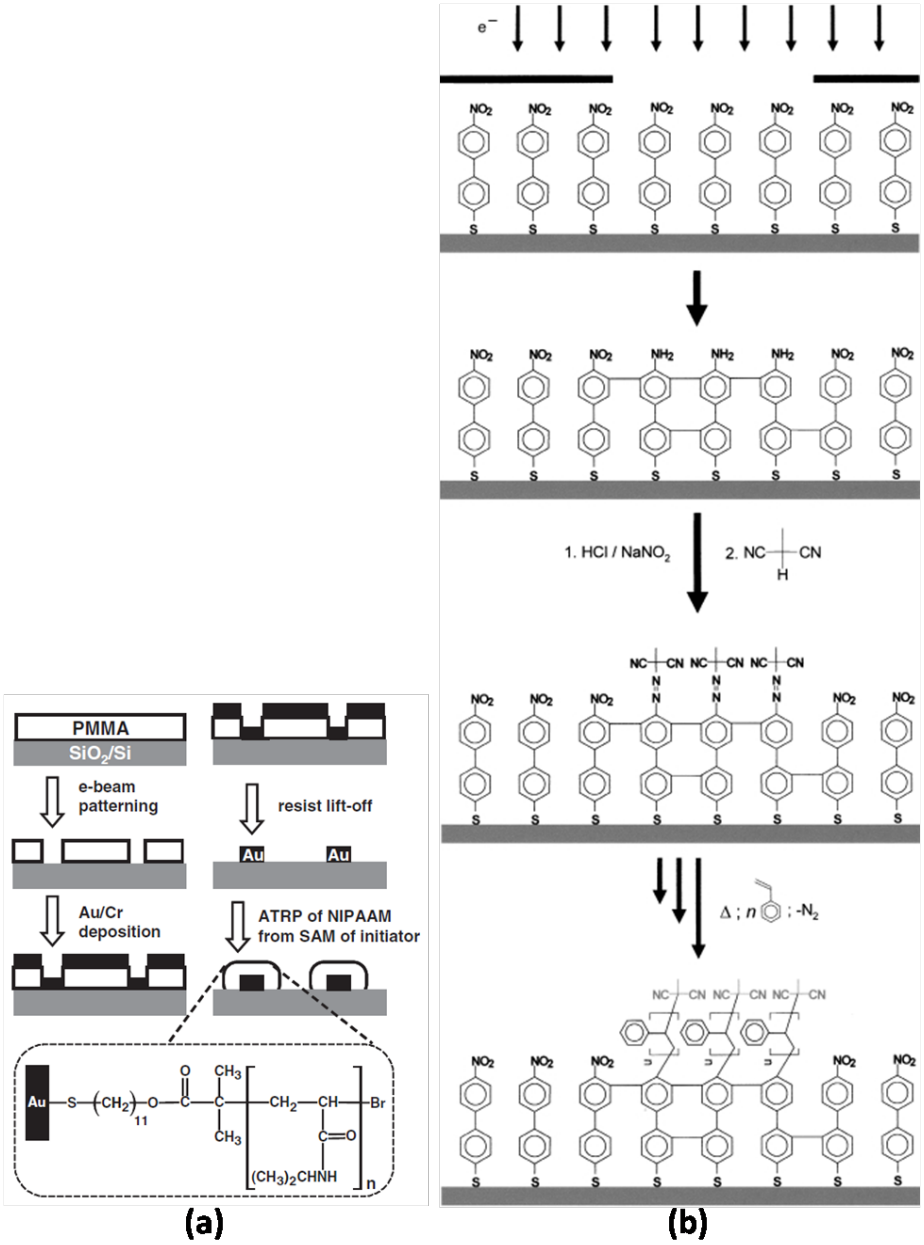

Figure 1.6 Polymer brush patterning using electron beam lithography. a) Using e-beam lithography to pattern a resist, backfilled with gold, followed by immobilization of thiol initiator onto the patterned gold arrays. b) Using an e-beam to chemically pattern a SAM, an ATRP initiator is bound to the patterned regions followed by SI-ATRP. (Reprinted from Ref. # 43 and #44 with permission from WILEY-VCH Verlag, GmbH & Co. KGaA, Weinheim)

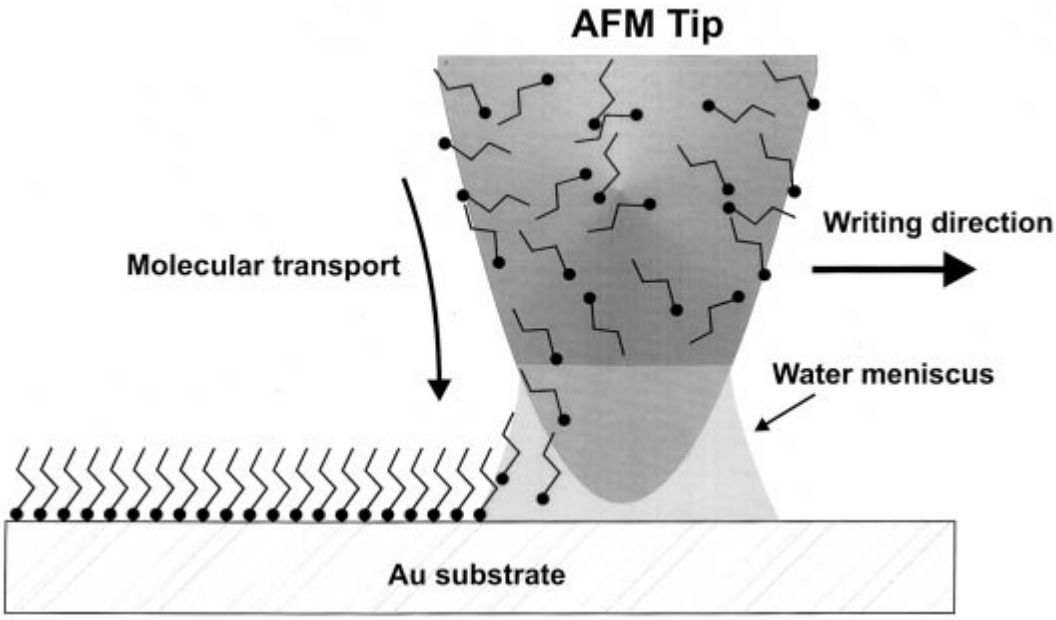

Figure 1.7 Schematic representation of dip-pen nano-lithography. (Reprinted from Ref. #45 with permission from Science Magazine)

molecules were patterned on a gold substrate using DPN. Ring-opening metathesis polymerization (ROMP) of exo-5-norbornen-2-ol was done on the patterned molecules to produce line and dot arrays of polymer brushes.[46]

Microcontact printing (μCP) is a soft lithography technique used as an alternative to the more conventional photo- and electron beam lithography. The procedure is simple and involves using an elastomeric stamp to transfer molecules, or "ink" material, to a surface by contact. Microcontact printing was first demonstrated in the patterning of SAMs of alkanethiolates on gold, resulting in well defined features with dimensions as small as 1 μm and regions as large as several square cm.[47] Since then, microcontact printing has been adapted to fabricate patterned polymer brushes. Figure 1.8 illustrates one of the μCP strategies to fabricate polymer brushes. This method was used by Abbot et al. to prepare patterned brushes through surface initiated ring-opening polymerization (ROP) of ε-caprolactone. A non-reactive SAM was first printed onto a gold substrate. A functionalized thiol was then selectively assembled into the bare regions of the gold surface by simple immersion into a solution of the molecule. ROP of ε-caprolactone from the patterned functionalized SAM was done to prepare a patterned polymer brush surface.[48] Since then, many other monomers have been polymerized using a variety of polymerization methods to make patterned brushes with μCP.[49-53] μCP was even used to achieve site-specific grafting of polymer chains to a surface, as opposed to the "grafting from" methods mentioned above.[54]

In addition to the techniques mentioned above, other less common patterning techniques have been reported. Nanoimprint lithography of copolymers bearing initiating groups,[55] contact molding,[33] capillary force lithography,[56] and microelectrochemical patterning[57] have been reported as methods to prepare patterned polymer brushes. "Bottom-up" self-assembly of diblock copolymer brushes has been simulated by Griffiths and coworker.[58] If produced, these brushes would possess the

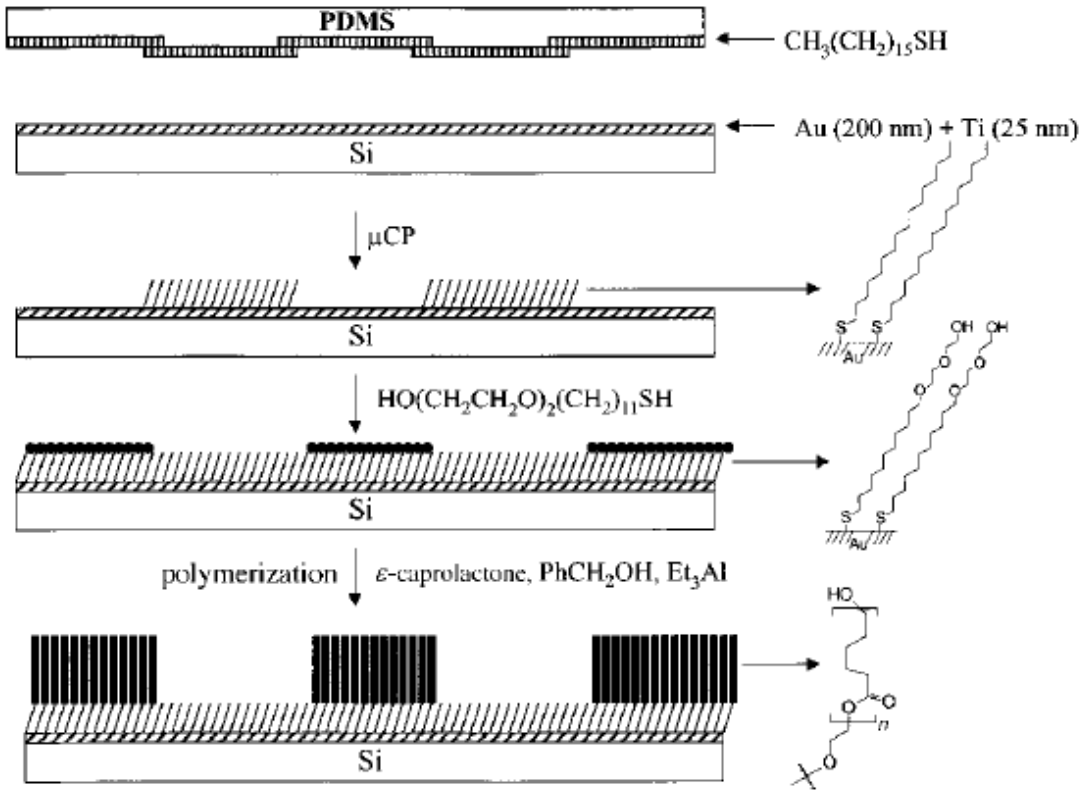

Figure 1.8 Scheme of the microcontact printing polymer brush patterning process. (Reprinted from Ref. #48 with permission from WILEY-VCH Verlag, GmbH & Co. KGaA, Weinheim)

templating nature offered by self-assembled block copolymers while exhibiting the robustness of the brush. However as with block copolymer thin films, the self-assembly must be well characterized if this approach is to be feasible.

1.3 Polymer Thin Film Characterization

Proper characterization is key to technical control and improvement of materials. Although there exists an immense number of techniques available to characterize polymer thin films, detailing them all is beyond the scope of this chapter. Thus, this section will concentrate on two powerful techniques, grazing incidence small angle x-ray scattering (GISAXS) and near edge x-ray absorption fine structure (NEXAFS) spectroscopy.

1.3.1 GISAXS

GISAXS is a versatile and powerful technique used to characterize nano-structured surfaces and thin films. It combines features offered by small angle x-ray scattering (SAXS), such as its accessible length scales and area detection, with the surface sensitivity of grazing incidence diffraction (GID). The technique was first introduced by Levine and coworkers in 1989, studying thin film growth.[59] It wasn't long before the technique evolved and began to be used to study quantum dots, nano-particles, and polymer thin films.

Surface sensitive x-ray scattering can be accomplished by choosing an angle of incidence, α_i, below the critical angle for total reflection of the film, α_c. In optics, Snell's law describes the relationship between the angles of incidence and refraction of light when passing through a boundary between two different media.

$$n_1 / n_2 = \cos \alpha_2 / \cos \alpha_1 \qquad (1.1)$$

Assuming medium 1 is air and medium 2 is the film material, n_1 / n_2 will be greater than 1, implying that unless α_1 is greater than some critical value, the light will be

totally externally reflected. However, in addition to the reflected beam, there is an evanescent beam which travels along the surface and penetrates only a few nanometers. This evanescent wave can then undergo scattering in the near surface region. Cho and coworkers first demonstrated this effect in 1979 with their structural study of the GaAs-Al interface.[60] Since then, surface sensitive GISAXS has been adapted to the study of islands dispersed on a flat surface or nanoparticles included in a thin film. Brault et al. used GISAXS as a complimentary tool to transmission electron microscopy (TEM) to characterize the nucleation and growth of platinum islands by plasma sputter deposition.[61]

Probing the film interior requires an α_i between the α_c of the film and the substrate, to obtain the largest scattering cross-section. However, multiple scattering effects must be taken into account to properly model the data. To deal with the refraction and reflection effects from the interfaces, calculations based on the distorted wave born approximation (DWBA) must be considered. The interested reader is referred to a comprehensive review on the topic by Sinha.[62] Another effect can be seen in two-dimensional area detection. A signal enhancement of the scattered beam arises when the exit angle is close to the critical angle of the film, which is termed the Yoneda band. This enhancement is due to the Vineyard effect and originates from the linear relationship between the amplitudes of the refracted and incident wave, and taking into consideration Snell's law.[63] Figure 1.9 displays the amplitude of the electric field, normalized to the incident field amplitude, as a function of incidence angle.

Adapting GISAXS to characterize polymer thin film morphology is useful as the GISAXS intensity map provides information about both the lateral and normal ordering within the film. Also, special sample preparation is not necessary, unlike

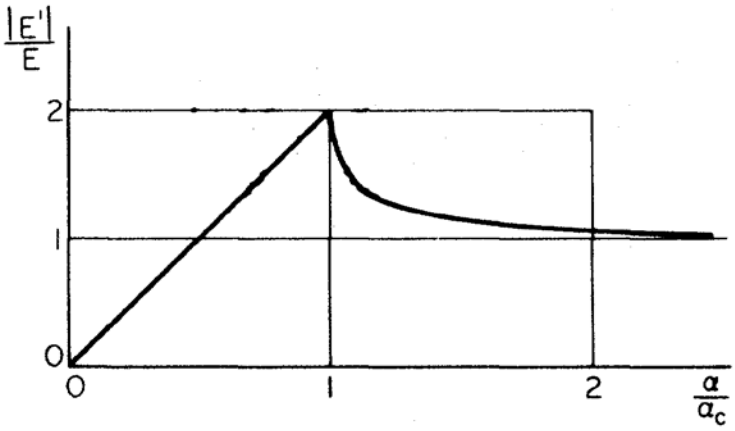

Figure 1.9 Magnitude of the electric field inside the scatterer, as a function of angle of incidence. Note that there is significant signal enhancement near the critical angle. (Reprinted from Ref. # 63 with permission from the American Physical Society)

TEM, other than thin film preparation making it a convenient characterization tool. Film thicknesses can range from a few nanometers to several hundred nanometers.

Polymers forming parallel and perpendicular oriented lamellae have been well characterized using a combination of atomic force microscopy (AFM) and GISAXS. Depending on the preference of one of the blocks to wet one or both interfaces, the lamellae will orient parallel to the substrate.[64] If there is no preferential wetting of either block to the interfaces, then the lamellae will orient perpendicular to the surface. Busch and coworkers studied lamellae forming poly(styrene-*b*-butadiene) (PS-PB) block copolymer thin films. They found that with lower molecular weight block copolymer samples, the lamellae were oriented parallel to the substrate, whereas the higher molecular weight samples possessed a perpendicular orientation.[65] In addition, they also investigated the peak splitting phenomenon associated with the refraction and reflection effects from the interfaces and modeled the scattering within the framework of the DWBA.[66] For parallel lamellae, peaks were expected at

$$q_z = k_o \left(\pm sin\,\alpha_i \pm \left\{ sin^2\,\alpha_{cP} + \left[\frac{(2m+1)\lambda}{D_{lam}} \pm (sin^2\,\alpha_i - sin^2\,\alpha_{cP})^{\frac{1}{2}} \right]^2 \right\}^{\frac{1}{2}} \right) \quad (1.2)$$

It has also been shown that external stimuli such as temperature or electric fields could affect the self-assembly in block copolymer thin films. Tang et al. demonstrated the fabrication of lamellar poly(*n*-butyl acrylate-*b*-acrylonitrile) (PBA-b-PAN) with perpendicular orientation and large-scale alignment.[67] By using a directional casting technique known as zone-casting, lamellae with a periodicity of 36 nm were almost perfectly preserved over distances of tens of micrometers. Figure 1.10 illustrates the zone-casting procedure, along with the AFM and GISAXS images of the thin film.

Cylinder forming block copolymers have also been well characterized using GISAXS. Li *et al.* investigated poly(α-methylstyrene-*b*-hydroxystyrene) (PαMS-*b*-PHOST) thin films for photolithography applications and observed a perpendicular

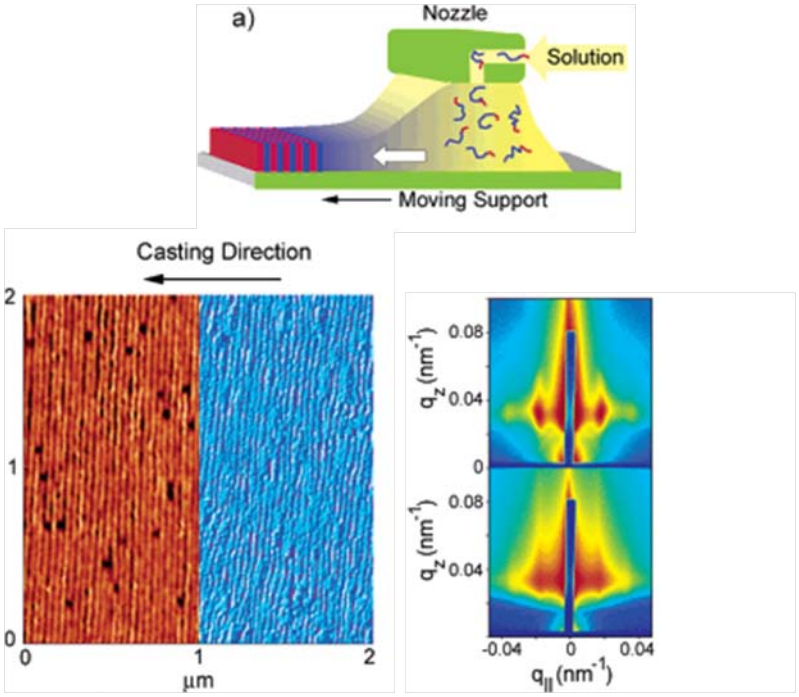

Figure 1.10 Top) Illustration of the zone casting procedure. Bottom) AFM of the perpendicular lamellae along with the GISAXS scattering images. (Reprinted from Ref. # 67 with permission from the American Chemical Society)

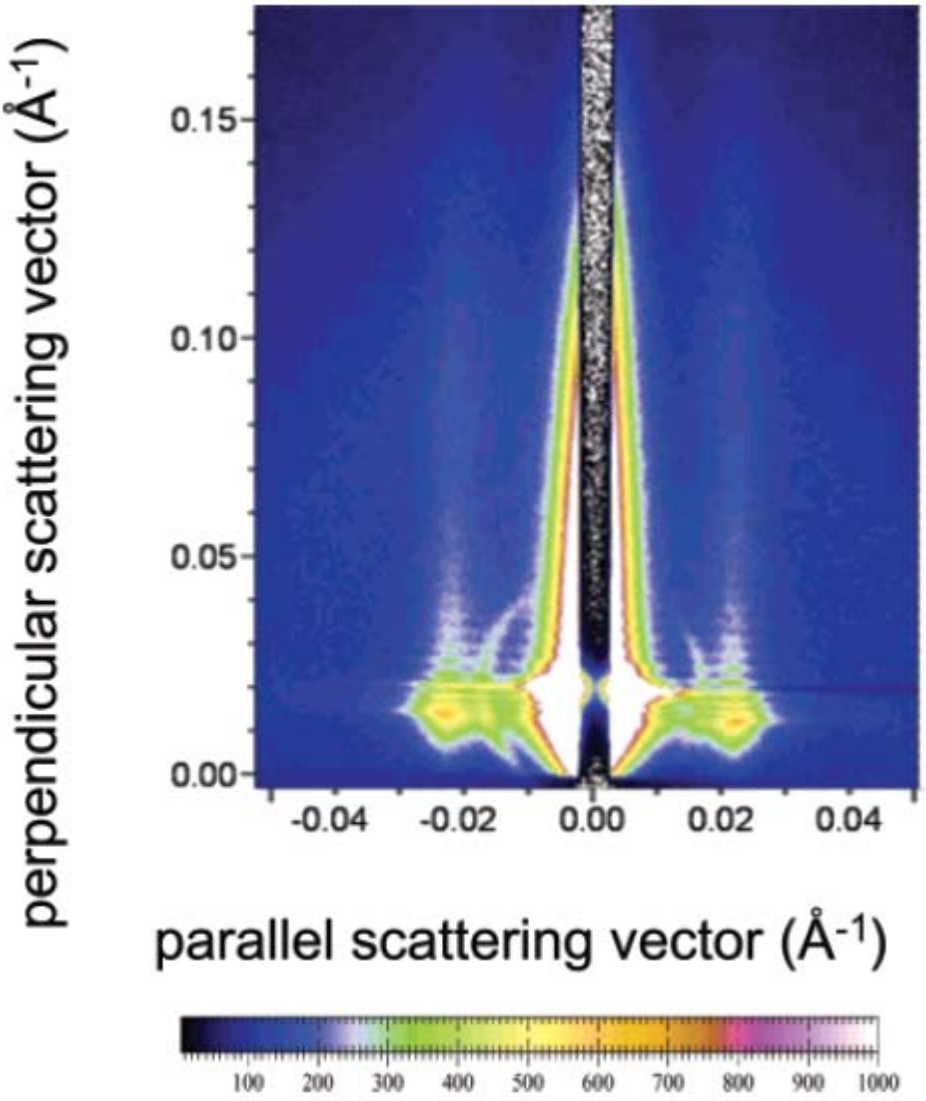

Figure 1.11 The long streaks, also called Bragg rods, are characteristic of perpendicular structures. (Reprinted from Ref. # 68 with permission from the American Chemical Society)

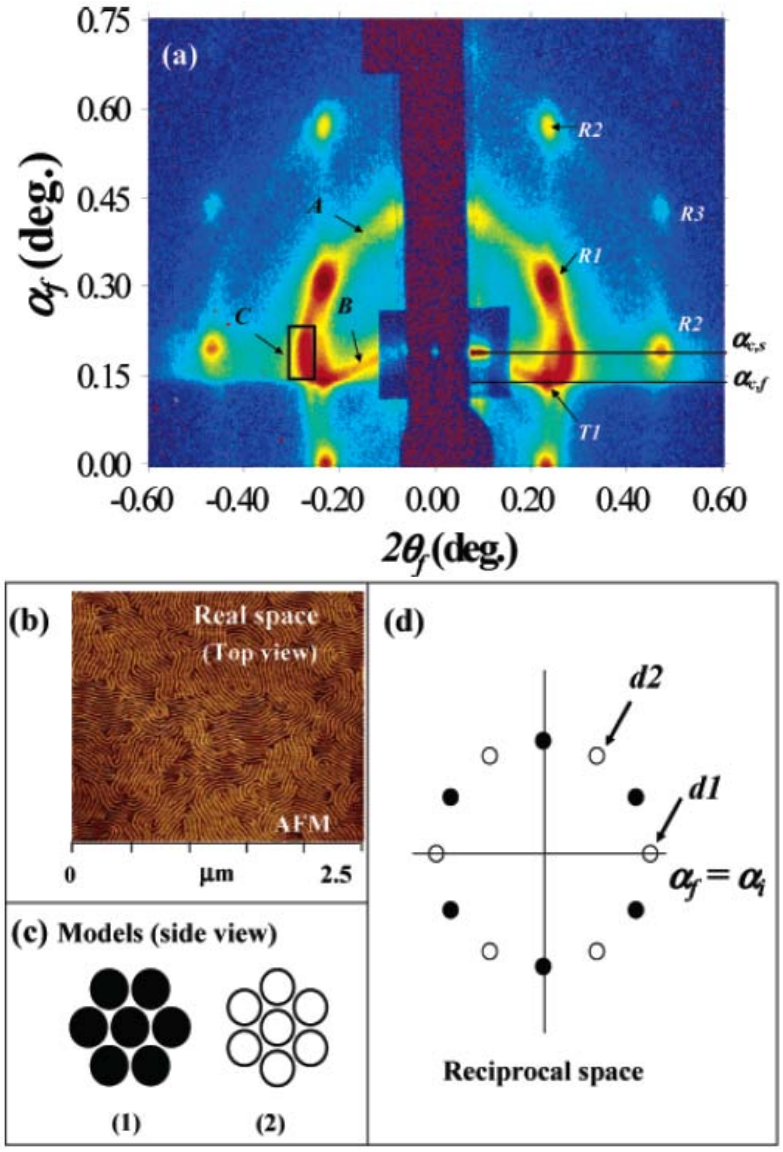

Figure 1.12 a) GISAXS scattering image of hexagonally packed lying cylinders. b) AFM of the lying cylinders displaying the characteristic "fingerprint" pattern. c) Real space model of the hexagonally packed cylinder orientation. d) The expected peak positions from the cylinders modeled in (c). (Reprinted from Ref. # 69 with permission from the American Chemical Society)

cylinder thin film morphology.[68] Characteristic vertical streaks in the GISAXS image consistent with cylinders oriented vertical to the substrate throughout the film can be seen in Figure 1.11. Block copolymer thin films with hexagonally packed lying cylinders were investigated by Lee and coworkers.[69] They not only modeled the scattering position from the hexagonally packed cylinders, but also modeled the peak splitting behavior within the DWBA. Figure 1.12 illustrates the real space model of the cylinders, the expected scattered peak positions in reciprocal space, and the experimental scattering image.

Other types of morphologies and ordered structures have also been investigated. Stein *et al.* studied the 2D to 3D packing in thin films, with a transition from hexagonally packed spheres to body centered cubic (BCC) spheres, depending on the number of layers.[70] Lee and coworkers also reported the scattering of hexagonally perforated lamellae (HPL) and a gyroid phase in PS-*b*-PI and indexed the scattered peaks.[69] Crossland et al. reported the use of a ordered bicontinuous gyroid semiconducting network in a hybrid bulk heterojunction solar cell.[6] They used poly(fluorostyrene-*b*-D,L-lactide) (PFS-*b*-PLA) as a template to fabricate a gyroid titania network and used GISAXS to characterize the structure of the film before and after PLA removal and after titanium oxide deposition, which is shown in Figure 1.13.

GISAXS is a powerful tool which does not require any difficult sample preparation and can be used to characterize the morphology of a film not only at the surface but also the film interior. While the technique has been used extensively to characterize thin film static structure, it is beginning to find use, through in-situ experiments, in studying how different stimuli affects the rearrangement within thin films. This ability only compounds the versatility which GISAXS possesses, making it even more attractive as a characterization tool for static and dynamic experiments.

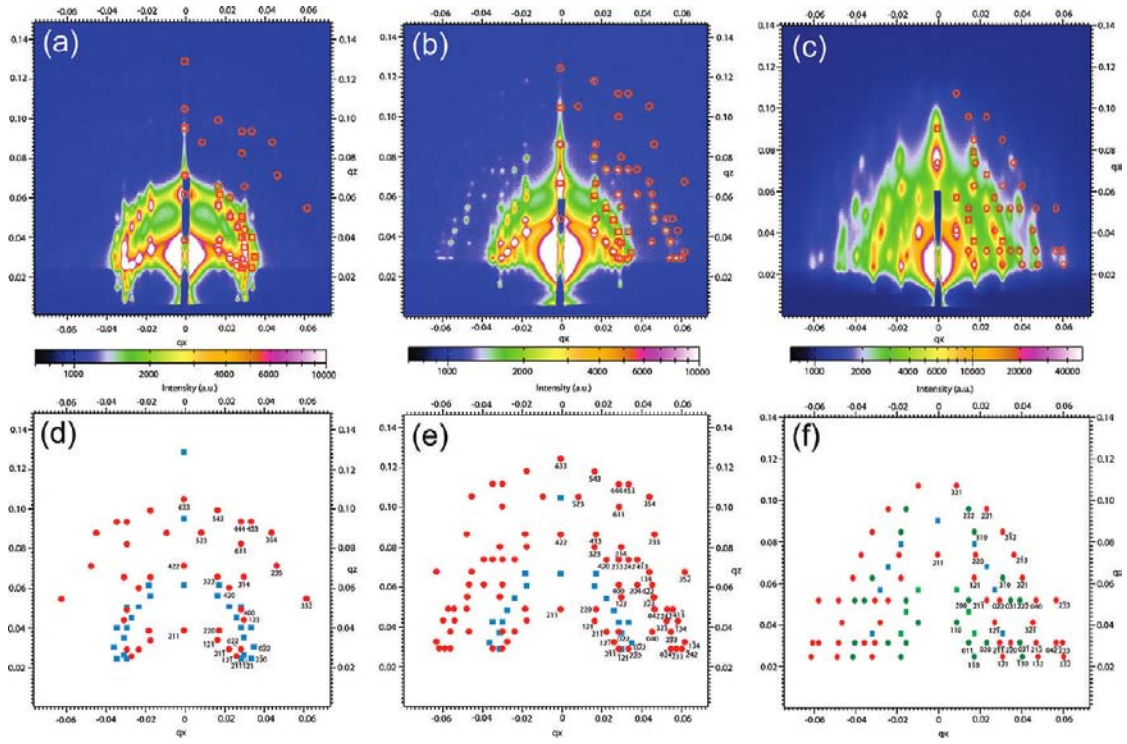

Figure 1.13 GISAXS scattering image a) after PLA removal. b) before PLA removal. c) after titanium oxide deposition. (d-f) The corresponding indexed scattered peak positions. (Reprinted from Ref. # 6 with permission from the American Chemical Society)

1.3.2 NEXAFS

NEXAFS spectroscopy is an ideal tool used to probe the chemical composition and molecular orientation of a surface. The technique involves the absorption of x-ray photons by a material of interest, resulting in the excitation of core level electrons to empty states above the Fermi level. The created holes can then be filled either through an Auger process or from an electron of a higher energy level followed by emission of a fluorescent photon as shown in Figure 1.14. NEXAFS spectra can thus be measured through the fluorescent yield, in which the emitted photons are monitored, or the electron yield where the emitted Auger electrons are recorded. The spectra measured via electron yield is very surface sensitive as electrons created beyond a certain depth will have lost too much energy to overcome the workfunction of the sample and the screening bias of the detector. Fluorescence yield detection permits the probing within the bulk of a material.

Information regarding the chemical composition of a sample can be determined as NEXAFS is element specific. X-ray absorption edges of different elements have different energies, so with a tunable soft x-ray source NEXAFS spectra of various elemental edges can be taken. Genzer *et al.* studied thin films of multi-armed semi-fluorinated side-chain liquid crystalline block copolymers.[71] In efforts to design material surfaces to possess low surface energy and enhance surface stability, the interplay between the liquid crystalinity of the semi-fluorinated groups and the microphase separated structures was studied. NEXAFS spectra of the two-armed liquid crystalline side-chain block copolymer thin films revealed segregation of the fluorinated segments to the surface (electron yield) compared to the bulk (fluorescence yield) of the film. Signals from the polystyrene phenyl rings show the opposite behavior. Figure 1.15 shows the partial electron and fluorescence yield of the thin film.

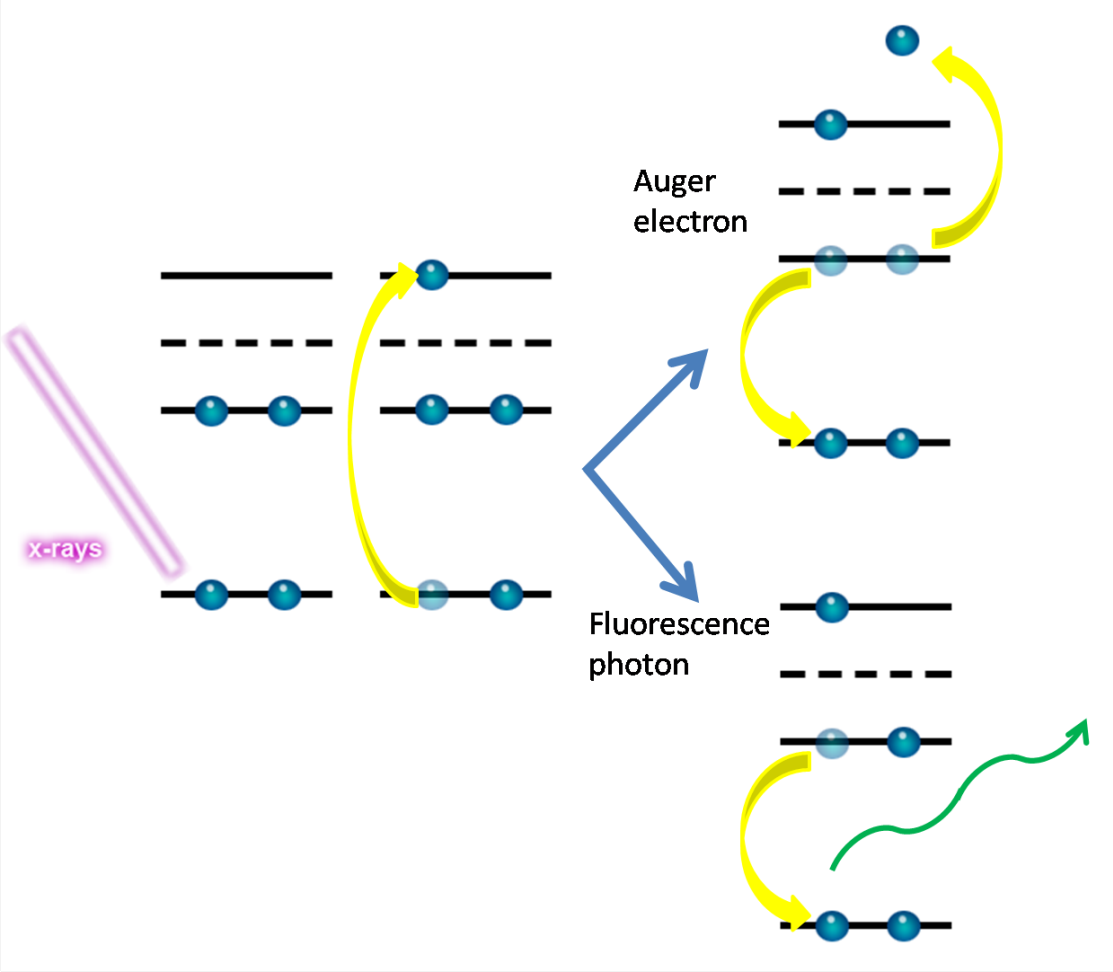

Figure 1.14 An illustration of the production the fluorescence photons and Auger electrons detected using NEXAFS spectroscopy.

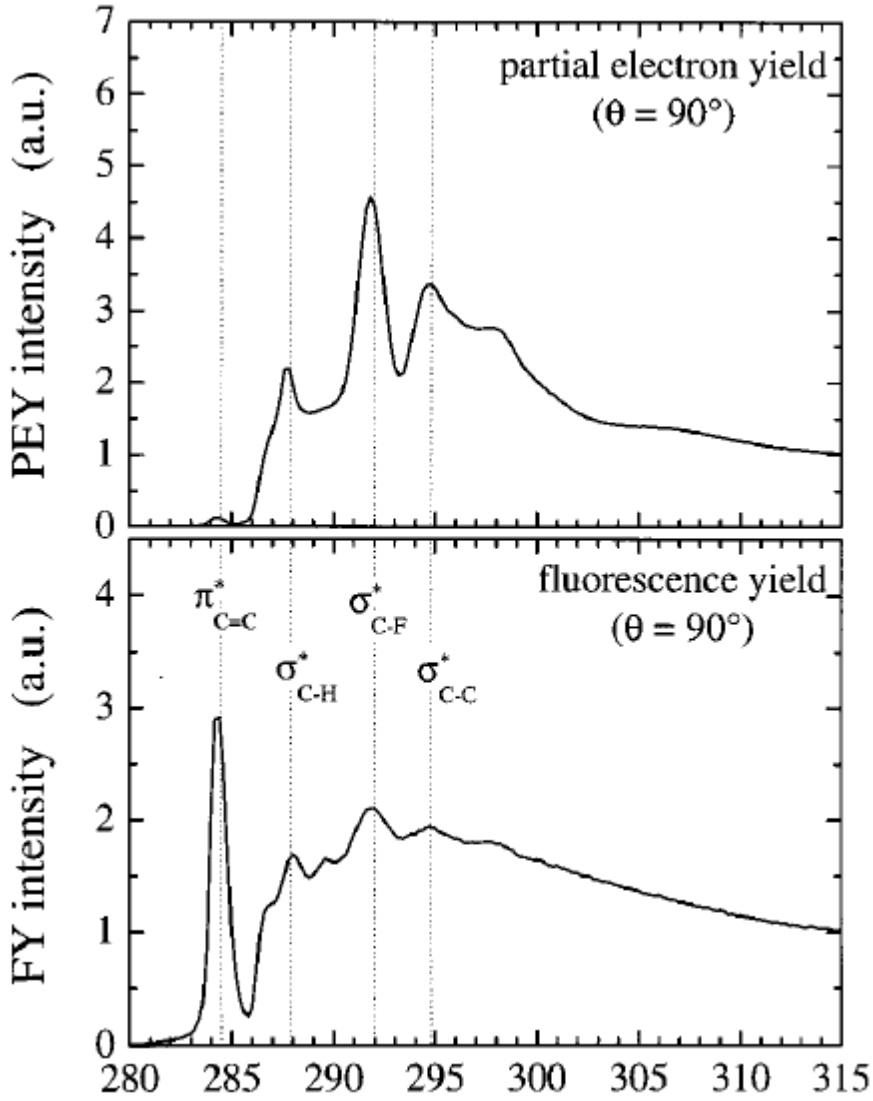

Figure 1.15 NEXAFS spectra of a two-armed semi-fluorinated liquid crystalline block copolymer. TOP) The partial electron yield reveals the surface composition. BOTTOM) The fluorescence yield details the bulk composition. (Reprinted from Ref. # 71 with permission from the American Chemical Society)

In addition to probing the chemical composition of a material, molecular orientation in ordered systems can be determined as well. As mentioned before, the absorption cross-section is dependent on the photon energy. However, it is also dependent on the angle between the transition dipole moment of the final orbital state of the excited atom and the electric field vector of the x-ray beam. By using a polarized light source, angle resolved NEXAFS spectra can be taken to determine the orientation of particular bonds. Paik *et al.* used angle resolved NEXAFS to determine how the surface stability of light responsive semi-fluorinated azobenzene liquid crystalline block copolymers affected the ability for the side-chains to reconstruct at the surface.[72] By comparing the NEXAFS spectra at varying angles before and after UV exposure, they were able to show that light induced surface changes could be inhibited with a sufficiently long side-chain fluorinated segment. Figure 1.16 shows the NEXAFS spectra before and after UV exposure of the homopolymer and block copolymer systems with 6 fluorocarbon repeat units (PI-F6 and PSPI-F6 respectively). Also, calculations of the orientational order parameter were determined for the $1s \rightarrow \pi^*_{C=C}$ and $1s \rightarrow \sigma^*_{C-F}$ transitions, and the average angle of the bonds were calculated.

In addition to being able to calculate the orientation of molecules at the surface, angle resolved NEXAFS can be used to do depth profiling experiments as well. By changing the angle between the sample surface and the partial electron yield detector, spectra at various electron emission angles can be taken. At larger emission angles, emitted electrons can penetrate a smaller sample depth before losing too much energy due to inelastic scattering. Genzer *et al.* used this technique to modify the building block model proposed by Outka and coworkers[73] for analyzing NEXAFS spectra to take into consideration the attenuation of the measured Auger yield.[74] Semi-

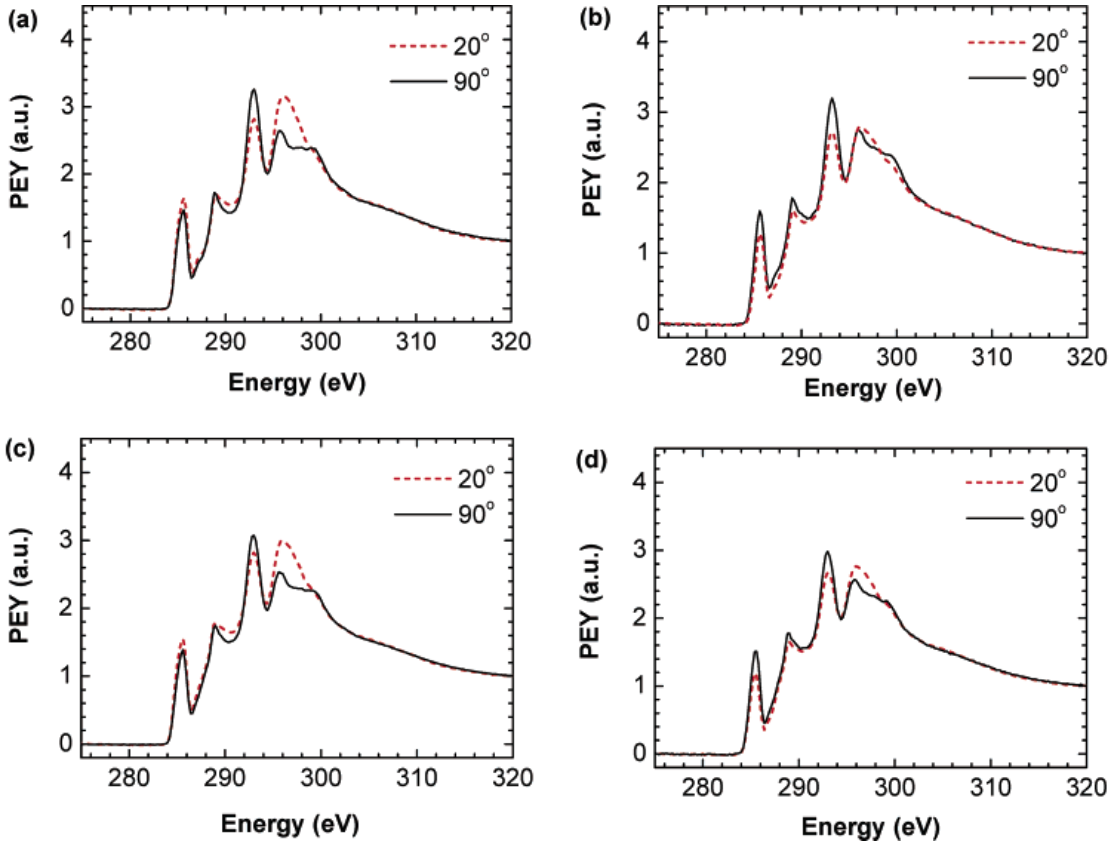

Figure 1.16 NEXAFS spectra of a) PI-F6 before UV exposure. b) PI-F6 during UV exposure. c) PSPI-F6 before UV exposure. d) PSPI-F6 during UV exposure. The peak at 285.5 eV corresponds to the signal from the PS backbone, whereas the peak at 293 eV corresponds to the signal from the fluorinated segment.

fluorinated SAMs on silicon were studied to model the orientational order parameter while taking into consideration the electron escape depth of the Auger electrons varying emission angles. Sohn *et al.* performed depth profiling experiments on a model system of highly oriented pyrolitic graphite (HOPG) with a very thin layer of perfluoropolyether.[75] They were able to experimentally determine the electron escape depth of the Auger electrons produced using the postedge partial electron yield intensity. Using this determined value, they also found a new method to determine the orientational order parameter.

1.4 Conclusion

With the growing demand for more sophisticated devices and the need for surfaces with tailored surface properties, much effort is being invested in research involving polymer thin film patterning. Of particular interest are polymer brushes, which offer chemical and mechanical robustness and longevity, and denser packing of desired functional groups. The patterning of polymer brushes has gained recent attention and these patterned surfaces have begun finding uses in a number of applications, some mentioned in the chapter. Numerous patterning techniques have emerged to accommodate the patterning length scales desired. However, with fabricated structures possessing dimensions in the nanometer regime, proper characterization must be done to confirm the structures produced. GISAXS and NEXAFS are newer techniques which offer surface sensitivity, the ability to identify molecular orientation, chemical composition, and hierarchical structure. These techniques are used to characterize our polymer thin film systems in more details in Chapters 4 and 5. In the following chapters, a new patterning technique is highlighted, and the versatility of this approach is explored.

REFERENCES

1. Shimoda, T.; Morii, K.; Seki, S.; Kiguchi, H., *Mater. Res. Soc. Bull.* **2003,** *28*, 821-827.

2. Huang, C.; Dong, B.; Lu, N.; Yang, B.; Gao, L.; Tian, L.; Qi, D.; Wu, Q.; Chi, L., *Small* **2009,** *5* (5), 583-586.

3. Bosworth, J. K.; Paik, M. Y.; Ruiz, R.; Schwartz, E. L.; Huang, J. Q.; Ko, A. W.; Smilgies, D.-M.; Black, C. T.; Ober, C. K., *ACS Nano* **2008,** *2* (7), 1396-1402.

4. Bosworth, J. K.; Black, C. T.; Ober, C. K., *ACS Nano* **2009,** *3* (7), 1761-1766.

5. Stoykovich, M. P.; Muller, M.; Kim, S. O.; Solak, H. H.; Edwards, E. W.; de Pablo, J. J.; Nealey, P. F., *Science* **2005,** *308* (5727), 1442-1446.

6. Crossland, E. J. W.; Kamperman, M.; Nedelcu, M.; Ducati, C.; Wiesner, U.; Smilgies, D.-M.; Toombes, G. E. S.; Hillmyer, M. A.; Ludwigs, S.; Steiner, U.; Snaith, H. J., *Nano Letters* **2008,** *0* (0), Article ASAP.

7. Finlay, J. A.; Krishnan, S.; Callow, M. E.; Callow, J. A.; Dong, R.; Asgill, N.; Wong, K.; Kramer, E. J.; Ober, C. K., *Langmuir* **2007,** *24* (2), 503-510.

8. Brizzolara, R. A., *Biosensors and Bioelectronics* **2000,** *15* (1-2), 63-68.

9. Dong, R.; Krishnan, S.; Baird, B. A.; Lindau, M.; Ober, C. K., *Biomacromolecules* **2007,** *8*, 3082.

10. Andruzzi, L.; Senaratne, W.; Hexemer, A.; Sheets, E. D.; Ilic, B.; Kramer, E. J.; Baird, B.; Ober, C. K., *Langmuir* **2005,** *21* (6), 2495.

11. Hollister, S. J., *Nature Materials* **2005,** *4*, 518-524.

12. Park, S.; Lee, D. H.; Xu, J.; Kim, B.; Hong, S. W.; Jeong, U.; Xu, T.; Russell, T. P., *Science* **2009,** *323* (5917), 1030-1033.

13. Adiga, S. P.; Brenner, D. W., *Nano Letters* **2005,** *5* (12), 2509.

14. Valkama, S.; Kosonen, H.; Ruokolainen, J.; Haatainen, T.; Torkkeli, M.; Serimaa, R.; ten Brinke, G.; Ikkala, O., *Nat Mater* **2004,** *3* (12), 872-876.

15. Campbell, M.; Sharp, D. N.; Harrison, M. T.; Denning, R. G.; Turberfield, A. J., *Nature* **2000,** *404*, 53-56.

16. Milner, S. T., *Science* **1991,** *251*, 905.

17. Zhao, B.; Brittain, W. J., *Progress in Polymer Science* **2000,** *25*, 677.

18. Minko, S., Grafting on Solid Surfaces: "Grafting to" and "Grafting from" Methods. In *Polymer Surfaces and Interfaces*, 2008; pp 215-234.

19. Huang, H.; Penn, L. S., *Macromolecules* **2009,** *38* (11), 4837.

20. Zhou, F.; Huck, W. T. S., *Physical Chemistry Chemical Physics* **2006,** *8*, 3815.

21. Van der Waarden, M. J., *Journal of Colloid Science* **1950,** *5* (4), 317.

22. Klee, D.; Adermovic, Z.; Bosserhoff, A.; Hoecker, H.; GMaziolis, G.; Erli, H.-J., *Biomaterials* **2003,** *224*, 3663-3670.

23. Collier, T. O.; Wesley, R. A.; Luginbuhl, R.; Denton, D. D.; Ratner, B. D., *J. Biomed. Mater. Res.* **2002,** *59*, 136-143.

24. Glinel, K.; Jonas, A. M.; Jouenne, T.; Leprince, J.; Galas, L.; Huck, W. T. S., *Bioconjugate Chem.* **2009,** *20*, 71-77.

25. Li, G.; Cheng, G.; Xue, H.; Chen, S.; Zhang, F.; Jiang, S., *Biomaterials* **2008,** *29*, 4592-4597.

26. Zhang, Z.; Finlay, J. A.; Wang, L.; Gao, Y.; Callow, J. A.; Callow, M. E.; Jiang, S., *Langmuir* **2009**.

27. Nejadnik, M. R.; van der Mei, H. C.; Norde, W.; Busscher, H. J., *Biomaterials* **2008,** *29*, 4117-4121.

28. Liu, M. L.; Bergbreiter, D. E., *J. Polym. Sci. Part A: Polym. Chem.* **2001,** *39*, 4119-4128.

29. Mulfort, K. L.; Ryu, J.; Zhou, Q., *Polymer* **2003,** *44*, 3185-3192.

30. Songtag, S. K.; Marshall, N.; Locklin, J., *Chem. Comm.* **2009,** (23), 3354-3356.

31. Zhou, F.; Liu, W.; Hao, J.; Xu, T.; Chen, M.; Xue, Q., *Adv. Funct. Mater.* **2003,** *13*, 938-942.

32. Pinto, J. C.; Whiting, G. L.; Khodabakhsh, S.; Torre, L.; Rodriguez, A. B.; Dalgliesh, R. M.; Higgins, A. M.; Andreasen, J. W.; Nielsen, M. M.; Geoghegan, M.; Huck, W. T. S.; Sirringhaus, H., *Advanced Functional Materials* **2008,** *18* (1), 36.

33. von Werne, T. A.; Germack, D. S.; Hagberg, E. C.; Sheares, V. V.; Hawker, C. J.; Carter, K. R., *Journal of the American Chemical Society* **2003,** *125* (13), 3831.

34. Casoli, A.; Brendle, M.; Schultz, J.; Auroy, P.; Reiter, G., *Langmuir* **2001,** *17*, 388-398.

35. Okano, T.; Yamada, N.; Okuhara, M.; Sakai, H.; Sakurai, Y., *Biomaterials* **1995,** *16* (4), 297-303.

36. Ruiz, R.; Kang, H.; Detcheverry, F. A.; Dobisz, E.; Kercher, D. S.; Albrecht, T. R.; de Pablo, J. J.; Nealey, P. F., *Science* **2008,** *321*, 936.

37. Shen, Y.; Zhan, Y.; Tang, J.; Xu, P.; Johnson, P. A.; Radosz, M.; van Kirk, E. A.; Murdoch, W. J., *American Institute of Chemical Engineers* **2008,** *54* (11), 2979.

38. Chen, M.; Briscoe, W. H.; Armes, S. P.; Cohen, H.; Klein, J., *ChemPhysChem* **2007,** *8* (9), 1303.

39. Gupta, B.; Plummer, C.; Bisson, I.; Frey, P.; Hilborn, J., *Biomaterials* **2002,** *23*, 863.

40. Senaratne, W.; Andruzzi, L.; Ober, C. K., *Biomacromolecules* **2005,** *6* (5), 2427.

41. Zhou, F.; Jiang, L.; Liu, W.; Xue, Q., *Macromolecular Rapid Communications* **2004,** *25* (23), 1979-1983.

42. Husemann, M.; Morrison, M.; Benoit, D.; Frommer, J.; Mate, C. M.; Hinsberg, W. D.; Hedrick, J. L.; Hawker, C. J., *Journal of the American Chemical Society* **2000,** *122*, 1844-1845.

43. Ahn, S. J.; Kaholek, M.; Lee, W.; LaMattina, B.; LaBean, T. H.; Zauscher, S., *Adv. Mater.* **2004,** *16*, 2141.

44. Schmelmer, U.; Jordan, R.; Geyer, W.; Eck, W.; Gölzhäuser, A.; Grunze, M.; Ulman, A., *Angewandte Chemie International Edition* **2003,** *42* (5), 559-563.

45. Piner, R. D.; Zhu, J.; Xu, F.; Hong, S.; Mirkin, C. A., *Science* **1999,** *283* (5402), 661-663.

46. Liu, X.; Guo, S.; Mirkin, C. A., *Angewandte Chemie* **2003,** *115* (39), 4933-4937.

47. Kumar, A.; Whitesides, G. M., *Applied Physics Letters* **1993,** *63* (14), 2002-2004.

48. Husemann, M.; Mecerreyes, D.; Hawker, C. J.; Hedrick, J. L.; Shah, R.; Abbott, N. L., *Angewandte Chemie International Edition* **1999,** *38* (5), 647-649.

49. Alarcon, C. d. l. H.; Farhan, T.; Osborne, V. L.; Huck, W. T. S.; Alexander, C., *Journal of Materials Chemistry* **2005,** *15* (21), 2089-2094.

50. Jones, D. M.; Smith, J. R.; Huck, W. T. S., *Adv. Mater.* **2002,** *14*, 1130.

51. Ma, H.; Hyun, J.; Stiller, P.; Chilkoti, A., *Advanced Materials* **2004,** *16* (4), 338-341.

52. Chen, T.; Zhang, J.; Chang, D. P.; Garcia, A.; Zauscher, S., *Advanced Materials* **2009,** *21* (18), 1825-1829.

53. Edmondson, S.; Huck, W. T. S., *Advanced Materials* **2004,** *16* (15), 1327-1331.

54. Yu, K.; Cong, Y.; Fu, J.; Xing, R.; Zhao, N.; Han, Y., *Surface Science* **2004,** *572* (2-3), 490-496.

55. Jhaveri, S. B.; Beinhoff, M.; Hawker, C. J.; Carter, K. R.; Sogah, D. Y., *ACS Nano* **2008,** *2* (4), 719-727.

56. Liu, Y.; Klep, V.; Luzinov, I., *Journal of the American Chemical Society* **2006,** *128* (25), 8106.

57. Slim, C.; Tran, Y.; Chehimi, M. M.; Garraud, N.; Roger, J.; Combellas, C.; Kanoufi, F., *Chem. Mater.* **2008,** *20*, 6677.

58. Matsen, M.; Griffiths, G., *The European Physical Journal E: Soft Matter and Biological Physics* **2009,** *29* (2), 219-227.

59. Levine, J. R.; Cohen, J. B.; Chung, Y. W.; Georgopoulos, P., *J. Appl. Cryst.* **1989,** *22*, 528-532.

60. Marra, W. C.; Eisenberger, P.; Cho, A. Y., *Journal of Applied Physics* **1979,** *50* (11), 6927-6933.

61. Andreazza, P.; Andreazza-Vignolle, C.; Rozenbaum, J. P.; Thomann, A. L.; Brault, P., *Surface and Coatings Technology* **2002,** *151-152*, 122-127.

62. Sinha, S. K.; Sirota, E. B.; Garoff, S.; Stanley, H. B., *Physical Review B* **1988,** *38* (4), 2297.

63. Vineyard, G. H., *Physical Review B* **1982,** *26* (8), 4146.

64. Anastasiadis, S. H.; Russell, T. P.; Satija, S. K.; Majkrzak, C. F., *Physical Review Letters* **1989,** *62* (16), 1852.

65. Busch, P.; Posselt, D.; Smilgies, D. M.; Rauscher, M.; Papadakis, C. M., *Macromolecules* **2007,** *40* (3), 630-640.

66. Busch, P.; Rauscher, M.; Smilgies, D.-M.; Posselt, D.; Papadakis, C. M., *Journal of Applied Crystallography* **2006,** *39* (3), 433-442.

67. Tang, C.; Tracz, A.; Kruk, M.; Zhang, R.; Smilgies, D.-M.; Matyjaszewski, K.; Kowalewski, T., *Journal of the American Chemical Society* **2005,** *127* (19), 6918-6919.

68. Li, M.; Douki, K.; Goto, K.; Li, X.; Coenjarts, C.; Smilgies, D. M.; Ober, C. K., *Chemistry of Materials* **2004,** *16* (20), 3800-3808.

69. Lee, B.; Park, I.; Yoon, J.; Park, S.; Kim, J.; Kim, K.-W.; Chang, T.; Ree, M., *Macromolecules* **2006,** *38* (4311-4323).

70. Stein, G. E.; Kramer, E. J.; Li, X.; Wang, J., *Macromolecules* **2007,** *40* (7), 2453-2460.

71. Genzer, J.; Sivaniah, E.; Kramer, E. J.; Wang, J.; Xiang, M.; Char, K.; Ober, C. K.; Bubeck, R. A.; Fischer, D. A.; Graupe, M.; Colorado, R.; Shmakova, O. E.; Lee, T. R., *Macromolecules* **2000,** *33* (16), 6068-6077.

72. Paik, M. Y.; Krishnan, S.; You, F.; Li, X.; Hexemer, A.; Ando, Y.; Kang, S. H.; Fischer, D. A.; Kramer, E. J.; Ober, C. K., *Langmuir* **2007,** *23* (9), 5110-5119.

73. Outka, D. A.; Stöhr, J.; Rabe, J.; Swalen, J. D.; Rotermund, H. H., *Physical Review Letters* **1987,** *59* (12), 1321.

74. Genzer, J.; Kramer, E. J.; Fischer, D. A., *Journal of Applied Physics* **2002,** *92* (12), 7070-7079.

75. Sohn, K. E.; Dimitriou, M. D.; Genzer, J.; Fischer, D. A.; Hawker, C. J.; Kramer, E. J., *Langmuir* **2009,** *25* (11), 6341-6348.

CHAPTER 2

PATTERNING OF POLYMER BRUSHES – A DIRECT APPROACH TO COMPLEX, SUB-SURFACE STRUCTURES

2.0 Introduction

Patterned polymer brushes can be exploited as a means to tailoring the surface properties of materials for desired shape, functionality, and feature dimensions. Polymer brushes in our study refer to tethered polymer chains that are immobilized by one end to a surface or an interface.[1, 2] The crowded tethering imparts sufficient constraints on the chains forcing them to stretch away from the surface or interface to avoid occupying the same volume. Polymer brushes first attracted attention in the 1950s when Van der Waarden showed that grafting polymer molecules to colloidal particles helped prevent flocculation.[3] In more recent studies, they have been considered for use in microelectronics as thin layer dielectric materials[4] and as a means to achieving extremely small feature sizes.[5] Other applications where they can be found useful are in bio-selective surfaces,[6] nanofluidic devices,[7] microreaction vessels and drug delivery,[8] biomimetic material fabrication,[9] and cell growth control.[10]

Conventionally, high resolution lithography of polymer brushes is done by first patterning an initiator layer on the substrate, followed by surface initiated polymerization of a suitable monomer from the initiator sites.[11] Several techniques have been used to fabricate patterned initiator monolayers such as microcontact printing,[12] initiator decomposition,[13] scanning probe microscopy techniques,[14] nano-imprint lithography,[15] and chemical lithography.[16] However, growth of patterned brushes in this way can lead to lower resolution features when the brush height is comparable in length to the pattern width due to chain relaxation into the voided

regions during growth.[17] Also, these approaches can involve time consuming, labor intensive steps which make them unattractive for practical use and also increase chances of surface contamination.

In order to overcome these shortcomings, we have studied the direct patterning of preformed polymer brushes. A single step patterning process not only remedies the drawbacks to conventional methods, but is expected to help improve the resolution of the patterned features as well. In this chapter we first report the direct patterning of polymer brushes in a single step using electron beam lithography. A schematic representation of the patterning process is shown in Figure 2.1. Poly(methyl methacrylate) (PMMA) and poly(2-hydroxyethyl methacrylate) (PHEMA) polymer brushes were grown on silicon surfaces via controlled atom transfer radical polymerization (ATRP). These PMMA and PHEMA homopolymer brushes were directly patterned via e-beam lithography to produce patterned polymer brush surfaces in a single step[18]. We have successfully formed polymer brush patterns as small as 20 nm using this single step approach.

We demonstrate, in addition, the ability to create sub-surface patterns in polymer brushes. Poly(methyl methacrylate)-b-polystyrene (PMMA-*b*-PS) and PHEMA-*b*-PS block copolymer brushes were grown by surface initiated atom transfer radical polymerization (ATRP) on preformed PMMA brushes. While neither is considered a modern high resolution resist, PMMA and PHEMA are known positive tone electron beam resists, and PS exhibits negative tone behavior[19]. These characteristics have been used by the block copolymer patterning community to create very small scale (~20 nm patterns) through self assembly[20]. By patterning a diblock copolymer brush using a negative tone upper block and a positive tone lower block, we demonstrate that sub-surface nano-channels can be formed by directly patterning

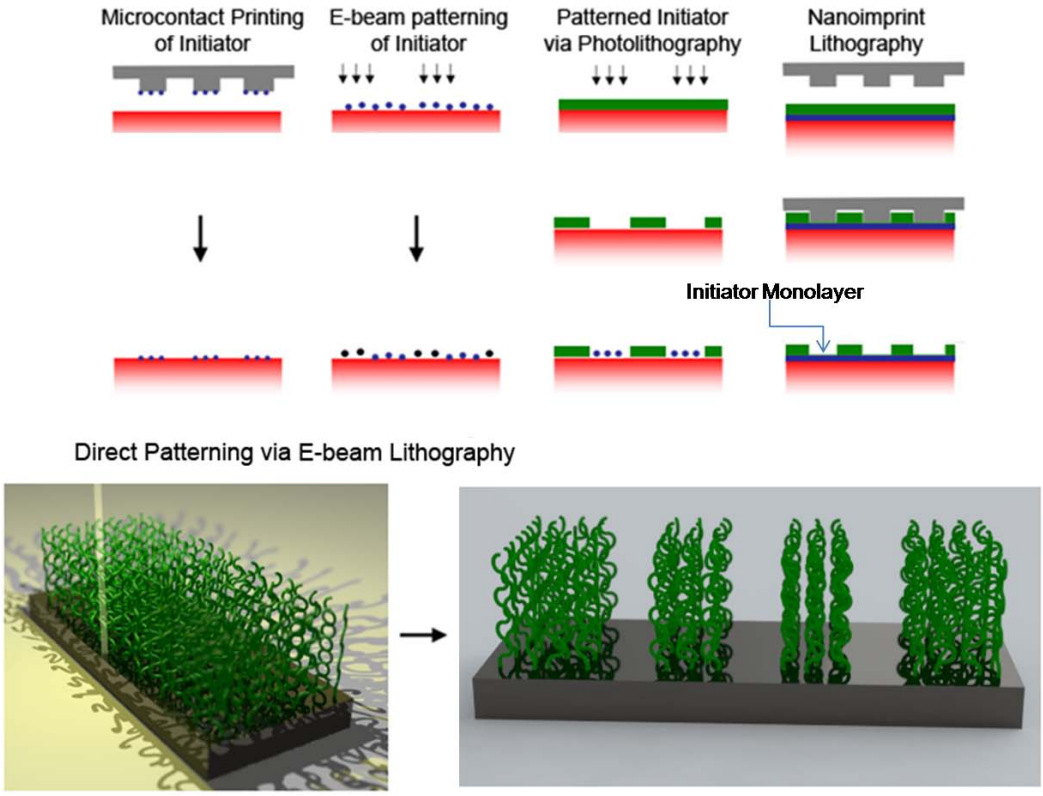

Figure 2.1 Direct patterning of polymer brush procedure compared to conventional lithographic methods.

these diblock copolymer brushes in a single step. No previously reported patterning technique can be used to produce these arbitrarily shaped sub-surface patterns, making the direct patterning process even more appealing. These patterned materials could be useful in such applications as nanofluidic devices,[21] waveguide materials,[22] and directed nanowire assembly.[23]

2.1 Experimental

Materials. Allyl-2-bromo-2-methylpropionate, chlorodimethylhydrosilane, Pt on activated carbon (10 wt %), triethylamine, copper (I) bromide, copper (II) dibromide, 2,2'-bipyridine, N, N, N′, N′, N′-pentamethyldiethylenetriamine (PMDETA), inhibitor remover packing material and anhydrous toluene were purchased from Sigma Aldrich and used without further purification. The monomers, methyl methacrylate (MMA) (inhibited with 10-100 ppm monomethyl ether hydroquinone (MEHQ)), 2-hydroxyethyl methacrylate (HEMA) (inhibited with 200 ppm MEHQ) and styrene, reagent plus™ (inhibited with 10-15 ppm 4-*tert*butyl catechol) were purchased from Sigma Aldrich. MMA and HEMA were purified by passing the monomers through a short column of MEHQ and HQ inhibitor remover packing material. Styrene was purified by passing it through a short column of basic alumina. Deionized water with a resistivity of 18.2 MΩ.cm at 25 °C was obtained from Millipore's Milli-Q® Synthesis A10 system. All other solvents for rinsing and cleaning were purchased from Fisher Scientific. Silicon wafers were obtained from Montco Silicon Technologies, Inc.

Synthesis and Immobilization of the Surface Initiator. Hydrosilylation of allyl 2-bromo-2-methylpropionate was carried out using a literature procedure to obtain the ATRP silane initiator, 3-(chlorodimethylsilyl)propyl 2-bromo-2-methylpropionate.[24] Silicon wafers were diced into 3 cm x 1 cm pieces and cleaned

by rinsing with acetone and dried under a nitrogen stream. To remove any organic residues on the surface, the substrates were further cleaned in Piranha solution (3:1 conc. H_2SO_4/30% H_2O_2 soln) for 30 minutes. (*Caution*: piranha solution reacts violently with organic materials and should be handled carefully). After rinsing with copius amounts of deionized water, the substrates were washed with dichloromethane and then dried in a vacuum oven for 10 min at 120 °C. The clean Si wafer pieces were immersed in a toluene solution of the silane initiator (2 mM) and triethyamine (0.05 mM) for 24 h. The wafers were then removed from the solution and washed with dichloromethane and left to stand in dichloromethane for 18 h. The initiator coated wafers were either used immediately or stored under standard conditions. No loss of activity was observed on storage for couple of weeks.

Preparation of Poly(methyl methacrylate) and Poly(2-hydroxyethyl methacrylate) Brushes. PMMA and PHEMA brushes were prepared using a modified literature procedure.[25] A typical reaction is described using PMMA brush as an example. In a typical reaction, two initiator coated silicon substrates (3 cm x 1cm) were placed in a 25 mL Schlenk flask under an argon atmosphere. The flask was evacuated and back filled with argon three times. CuBr (143 mg, 1.0 mmol), bipyridine (312 mg, 2.0 mmol) were taken in another 25 mL Schlenk flask equipped with a magnetic stir bar. The air in the flask was evacuated and replaced with argon three times. The solvent mixture (deionized water, 2 mL and methanol, 8 mL) and purified MMA (or HEMA) (10 g, 100 mmol) were purged separately with argon for about an hour and cannulated into the flask containing the ligand and copper salts. The reaction mixture was stirred at room temperature for 10 min to ensure the dissolution of the monomer and the copper-ligand complex in the solvent. This solution was then transferred into the flask containing the silicon wafer pieces. Polymerization was carried out for a set reaction time at 32 °C. After polymerization,

the substrates were removed from the flask and washed with dichloromethane and gently sonicated in dichloromethane for 5 min and dried under a stream of nitrogen.

Preparation of Poly(methyl methacrylate-b-styrene) and Poly(2-hydroxyethyl methacrylate-b-styrene) Brushes. In a typical reaction, two Si wafer pieces with PMMA (or PHEMA) brushes were placed in a 25 mL Schlenk flask under an argon atmosphere. The flask was evacuated and back filled with argon three times. CuBr (25 mg, 0.17 mmol) was taken in another 25 mL Schenk flask equipped with a magnetic stir bar. The air in the flask was evacuated and replaced with argon three times. For PMMA-*b*-PS, the solvent (anisole, 2.5 mL) and purified styrene (7.0 mL, 61.1 mmol) were purged separately with argon for about an hour and cannulated into the flask containing the copper salt. For PHEMA-*b*-PS, dimethylformamide (DMF) was used as the reaction solvent. PMDETA (67 μL, 0.32 mmol) was added and the reaction mixture was stirred at room temperature for 10 min to ensure the dissolution of the monomer and the copper-ligand complex in the solvent. This solution was then transferred into the flask containing the PMMA brushes. Polymerization was carried out for a set reaction time at 105 °C. After polymerization, the substrates were removed from the flask and washed with toluene and gently sonicated in toluene for 5 min and dried under a stream of nitrogen.

Characterization of Polymer Brushes. Polymer brushes were characterized by ellipsometry and atomic force microscopy (AFM). Thicknesses of the polymer brushes were measured using a Woollam variable angle spectroscopic ellipsometer at a 70° angle of incidence. A Cauchy model (Cauchy layer/silicon substrate) was used to fit the data, in which the Cauchy layer was representative of the polymer brush. Surface topography was analyzed and the root-mean-square (RMS) roughness was measured using a Veeco Dimension 3100 scanning probe microscope. Olympus

tapping mode etched silicon probes were used to acquire topographic images in air at room temperature.

Direct Patterning of Polymer Brushes. Patterning of the brushes was done at the Cornell Nanoscale Facility using the the Leica VB6-HR E and JEOL 9300 electron beam lithography systems. In order to get an estimate on the patterning conditions needed, contrast curves were generated from 10 μm x 1 μm areas exposed to the electron beam. A 0.5 nA beam current, 100 kV accelerating voltage, and 5 nm pixel size was used for the generation of the contrast curves and for higher resolution patterning. Doses ranging from 10 to 1200 $\mu C/cm^2$ were used in this study. The PMMA and diblock brushes were developed in a 1:3 methyl isobutyl ketone (MIBK) to isopropyl alcohol (IPA) mixture for 90 s followed by thorough rinsing in deionized water and then dried under a stream of nitrogen. PHEMA brushes were developed in a 0.09 N TMAH solution for 60 s followed by a rinsing in DI water and then dried under a stream of nitrogen. Imaging and depth measurements of the patterned surfaces were done with the Veeco Dimension 3100 scanning probe microscope, Olympus BX60/U-CFU real time confocal microscope, and the Zeiss Ultra 55 scanning electron microscope. Oxygen plasma etching of the PMMA homopolymer brush and diblock copolymer brush was done using the Plasmatherm Etcher SLR-720 with a flow rate of 30 sccm at a RF power of 25 W and a pressure of 60 mTorr. Etching was done for 40 seconds in 10 seconds intervals for the diblock brush and 20 seconds for the homopolymer brush.

2.2 Results and Discussion

The formation of a monolayer of initiator was confirmed by ellipsometry and AFM. The dry ellipsometric thickness of the covalently attached monolayer was measured to be 1.6 ± 0.3 nm (the error is due to uncertainties present during the

calculation of the film thickness from the optical data). This value is in good agreement with the theoretical height of the initiator containing SAM. The surface topography and roughness was measured by AFM. The RMS roughness of the initiator coated silicon substrate was 0.2 nm in a 0.5 x 0.5 μm^2 scanning area. This value is similar to the RMS roughness measured for clean bare silicon pieces.

PMMA and PHEMA homopolymer brushes were synthesized via ATRP based on the procedure described by Huck et al.[25] in an aqueous medium at room temperature. The reaction for the synthesis of the ATRP silane initiator and preparation of polymer brushes is shown in Scheme 2.1. No sacrificial initiator was added to the solvent mixture and the polymerization was surface initiated and surface confined, preventing the formation of undesirable polymer in solution and allowing clean surfaces to be obtained simply by washing the polymer brushes with water, acetone and ethanol. The polymerization appeared to be well controlled as reported previously by Jones and Huck as indicated by a linear increase in thickness of the brushes with polymerization reaction time[25]. The homopolymer brushes were characterized by ellipsometry and tapping mode AFM which indicated that the polymer brushes were homogeneous throughout the silicon substrate. PMMA brushes of ellipsometric thicknesses between 19-50 nm were used in this study. AFM of the PMMA brush surfaces revealed that the surfaces were very smooth with an RMS roughness of 0.34 nm. PHEMA brushes with ellipsometric thickness of 50 nm were used in this study. Tapping mode AFM of the PHEMA brushes showed an RMS roughness of 0.48 nm observed. All brushes showed increase in the ellipsometric thickness after re-initiation with styrene.

To investigate the feasibility of patterning polymer brushes in a single step, brushes of PMMA and PHEMA were directly patterned using electron beam lithography. As PMMA and PHEMA are known positive tone electron beam and UV

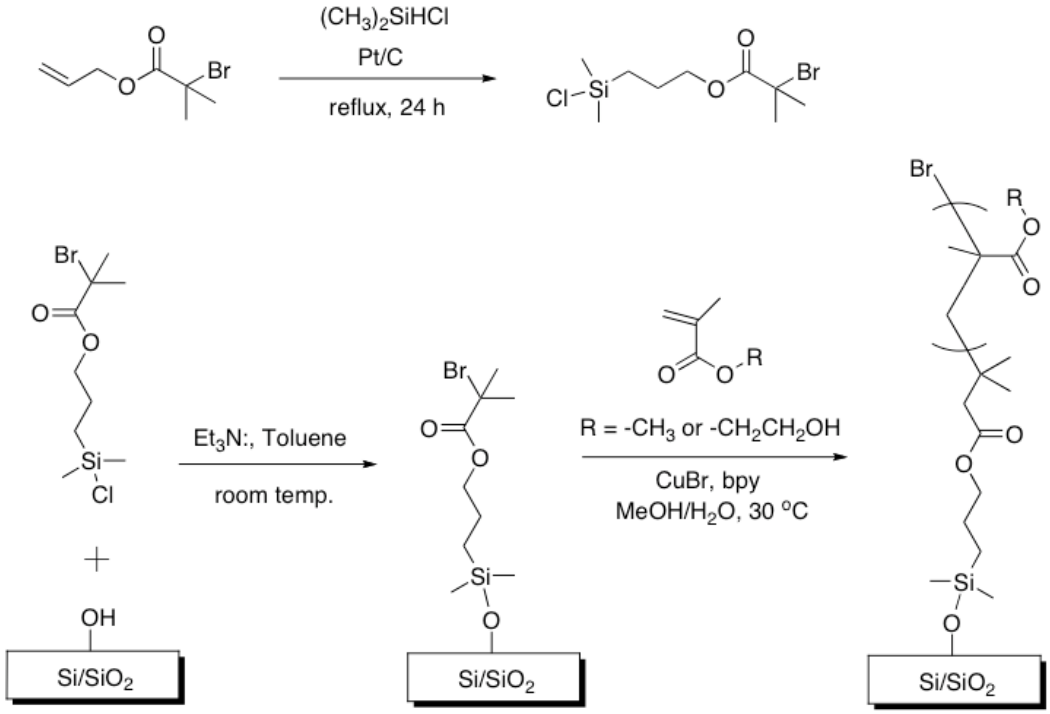

Scheme 2.1 Surface initiated ATRP reaction scheme for the synthesis of the PMMA and PHEMA homopolymer brushes as well as the PMMA-b-PS diblock copolymer brush.

resists,[26, 27] we chose these two corresponding monomers to demonstrate that direct patterning of these polymer brushes is also possible. The patterned polymer brushes were characterized and imaged through the use of tapping mode AFM.

PMMA brushes were successfully patterned in a single step on exposure to an electron beam. A 0.5 nA beam current, 100 kV accelerating voltage, and 5 nm pixel size was used for the generation of the contrast curves and for higher resolution patterning. Doses ranging from 10 to 1200 $\mu C/cm^2$ were used in this study. The PMMA and diblock brushes were developed in a 1:3 methyl isobutyl ketone (MIBK) to isopropyl alcohol (IPA) mixture for 90 s followed by thorough rinsing in deionized water and then dried under a stream of nitrogen. Pattern depths were measured using AFM and a contrast curve was generated as shown in Figure 2.2. Using the appropriate dose ascertained from the contrast curve, higher resolution lines of patterned PMMA brushes, were imaged using AFM as shown in Figure 2.3. Figure 2.3b shows a directly patterned PMMA brush with 20 nm lines with a pitch of 60 nm, demonstrating the ability of this polymer brush system to achieve high resolution patterned features in a single step.

Following the successful patterning of PMMA brushes, we also demonstrated the patterning of PHEMA brushes and compared their sensitivity towards e-beam patterning with that of PMMA brushes. PHEMA is a polymer that has also been demonstrated to exhibit positive tone patterning behavior under e-beam exposure conditions.[27] This polymer has pendent hydroxyl groups that can be easily functionalized through simple organic chemistry.[28] Thus, PHEMA brushes are a good candidate to prepare surfaces for applications that require controlled immobilization of chemical or biological moieties on patterned brushes. To understand the PHEMA brush character under electron beam exposure, similar patterning conditions were used to that for the PMMA brushes. PHEMA brushes ~50 nm in thickness were used in

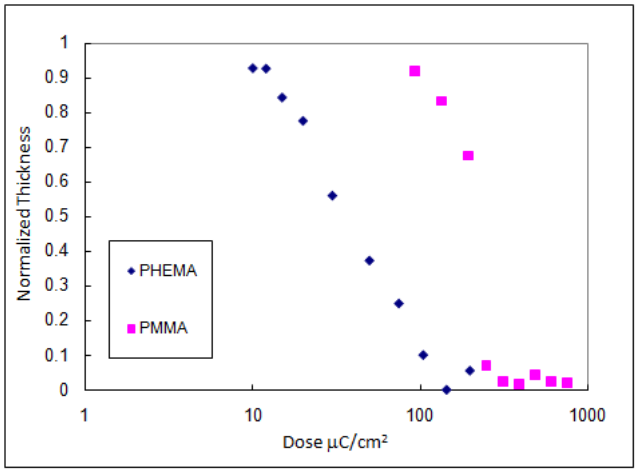

Figure 2.2 Normalized thickness vs. electron beam exposure dose of PMMA and PHEMA brushes.

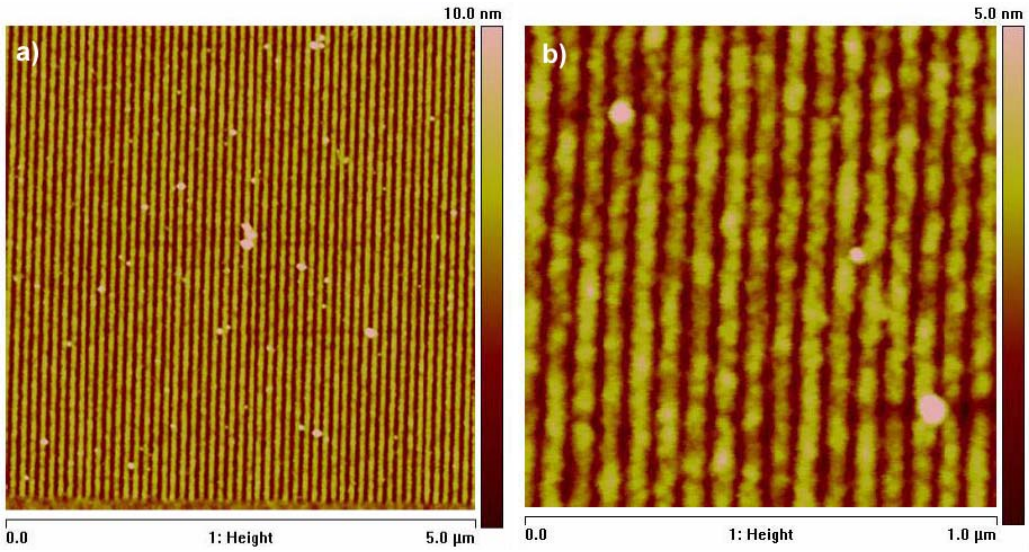

Figure 2.3 AFM height images of a patterned 19 nm thick PMMA brush. a) 50 nm exposed lines with 100 nm pitch. b) 20 nm exposed lines with a 60 nm pitch.

this study. The brushes were developed in a 0.09 N TMAH (tetramethylammonium hydroxide) solution for 60 s followed by a rinsing in DI water and then dried under a stream of nitrogen. A contrast curve was generated and is shown in Figure 2.2. Higher resolution patterns of PHEMA brushes are shown in Figure 2.4. Although the PHEMA brush appears to be more sensitive than the PMMA brush, its contrast is much poorer. Thus, the ultimate resolution of the patterned lines in this system appears to be lower in comparison as well. As the brushes are much lower in molecular weight in comparison to the typically spun coated electron beam resists, the polymer chains may be more susceptible to collapsing into the void areas. This increased susceptibility in combination with the loss of the constraint to force the chains to stretch away near the pattern edges, makes it reasonable that a more ideal developer would improve the patterned feature. However, many applications such as those in the biomaterials area, require only pattern features down to the micron regime, where line edge roughness of the patterned brushes is not very critical.

To study the versatility of the direct patterning technique, the single step patterning approach was investigated using diblock copolymer brushes of PMMA-*b*-PS and PHEMA-*b*-PS with an electron beam. Polystyrene has been shown to be a cross-linkable, negative tone electron beam resist.[19] By patterning a brush with a negative tone upper layer and a positive tone under layer, it should be possible to directly pattern stable nano-channels with precise control of the channel size and location. PMMA-*b*-PS and PHEMA-*b*-PS brushes were synthesized using surface initiated ATRP (see Supporting Information). The diblock copolymer brushes were grown from the characterized PMMA brushes (30 nm thick) and PHEMA brushes (50 nm thick) at 105 °C for 24 h and 14h, respectively. Ellipsometry clearly showed a change in thickness from 30 nm PMMA and 50 nm PHEMA brushes to 80 nm PMMA-*b*-PS and 80 nm PHEMA-*b*-PS brushes. The RMS roughness of the PMMA-

b-PS diblock copolymer brushes was measured to be 0.7 nm. The PHEMA-*b*-PS brushes were much rougher and appeared to form micelles at the surface.

PMMA patterning conditions were used for the PMMA-*b*-PS brush as PS is much more sensitive than the underlying PMMA layer. PMMA development conditions were also mimicked with immersion in a 1:3 MIBK to IPA mixture for 90 seconds. MIBK is known to be a very good solvent for polystyrene and can easily swell the cross-linked polymer.[29] This developer will penetrate the top PS layer and solubilize any scissioned PMMA fragments, allowing them to diffuse through the PS network. Previous work involving monitoring the diffusion rate of long polymer chains (M_n = 920 kg/mol) through a swollen cross-linked polystyrene network was done by Wu *et al*.[30] It was shown that the chain diffusion underwent three stages. In the first stage, the effective diffusion coefficient was even faster than the same chains in a free dilute solution and that the diffusion of longer chains through a small pore are accelerated by shorter chains that are present. Given that our system involves short scissioned polymer fragments with an original brush molecular weight of ~20 kg/mol, it is reasonable to assume the diffusion through the cross-linked PS upper layer to allow full development within the 90 second time-frame.

For the PHEMA-b-PS brushes, PHEMA patterning conditions were used. PHEMA development was done by sonicating the brush in DMF for 5 minutes. This development process was used as DMF is a good solvent for both the PS and scissioned PHEMA fragments and to ensure that the fragments would be able to penetrate through the swollen crosslinked PS layer.

To observe and confirm the resulting nano-channel layer in the PMMA-*b*-PS brush, etching of the PS was done using the SLR-720 Plasmatherm Etcher (see Supporting Information). Figure 5 shows the nano-channel patterning process and the corresponding topology during each step of the procedure. Not until the PS layer was

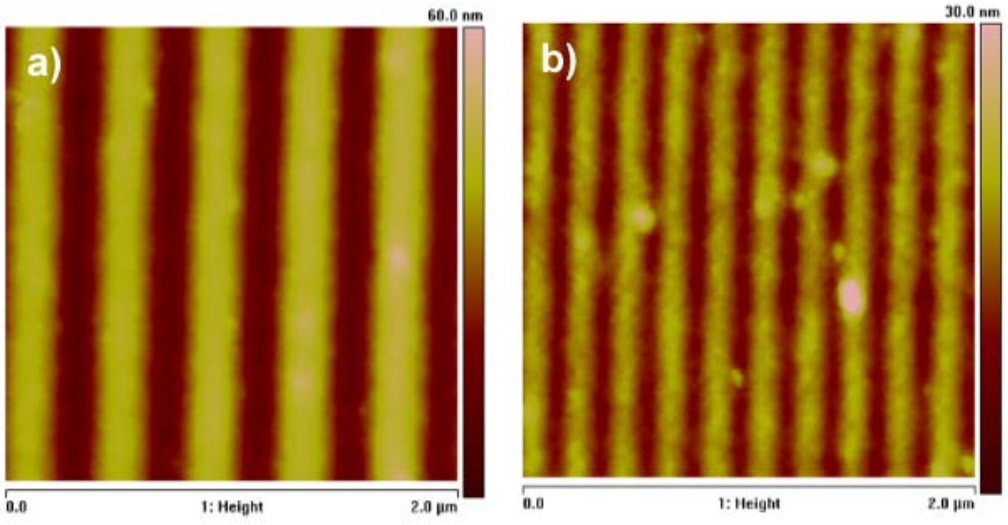

Figure 2.4 AFM height images of a patterned 50 nm thick PHEMA brush. a) 200 nm exposed lines with 400 nm pitch. b) 80 nm exposed lines with a 160 nm pitch.

etched away did any topological features appear under AFM. Even after development no topological change was observed, even with the cross-linked polystyrene undergoing swelling and de-swelling (Figure 2.5). The absence of topographical changes is understandable as Berger *et al.* studied the mechanical effects taking place after multiple swelling cycles of cross-linked polystyrene beads and saw that the beads retained their shape.[31] To eliminate the possibility that the etching process removed the scissioned PMMA instead of the development step, etching was done on a PMMA brush which was exposed to an electron beam but not developed. We found that the polymer fragments from the exposed regions did not get removed significantly faster than the unexposed brush as shown by comparisons between optical microscope images of the exposed, etched brush before and after development (see Supporting Information). Once the polystyrene layer was removed we were able to confirm the existence of the directly patterned nano-channels with AFM as seen in Figure 2.5c. Characterization of the nano-channels formed in the PHEMA-b-PS brush was more straightforward. Due to the harsher development process used in this system, the cross-linked PS layer sunk into the empty channel below. The sunken PS layer was imaged using AFM as seen in Figure 2.6. However, the uniformity of the channels was much poorer with this second system.

2.3 Conclusion

To conclude, we have successfully demonstrated the ability to directly pattern polymer brushes using electron beam lithography. Homopolymer brushes of PMMA and PHEMA exhibited electron beam resist behavior more sensitive to their spun coat counterparts. Also, the ability to directly pattern polymer brushes in a single step brings with it the advantages of simplicity, environmental benefits, and lower surface contamination risk. We speculate that improvements to the ultimate resolution

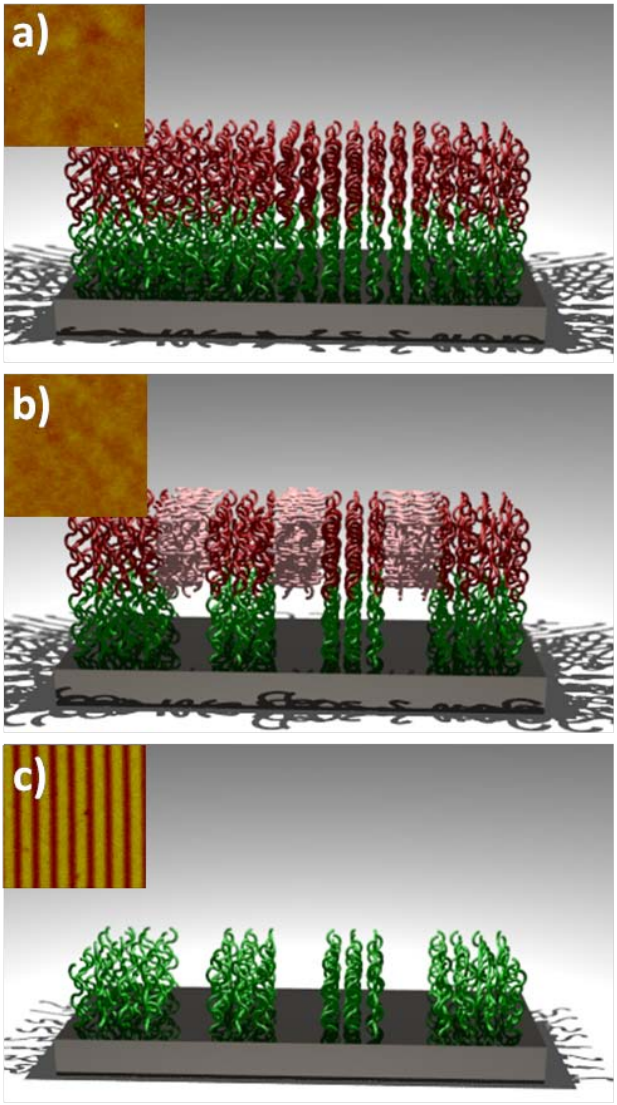

Figure 2.5 An illustration representing the nano-channel fabrication process with the corresponding surface topography as imaged by AFM. A 200 nm channel with 600 nm pitch was patterned. a) The diblock brush before patterning. b) The diblock brush after electron beam exposure. c) The diblock brush after development. d) The diblock brush after oxygen plasma etching the polystyrene layer away.

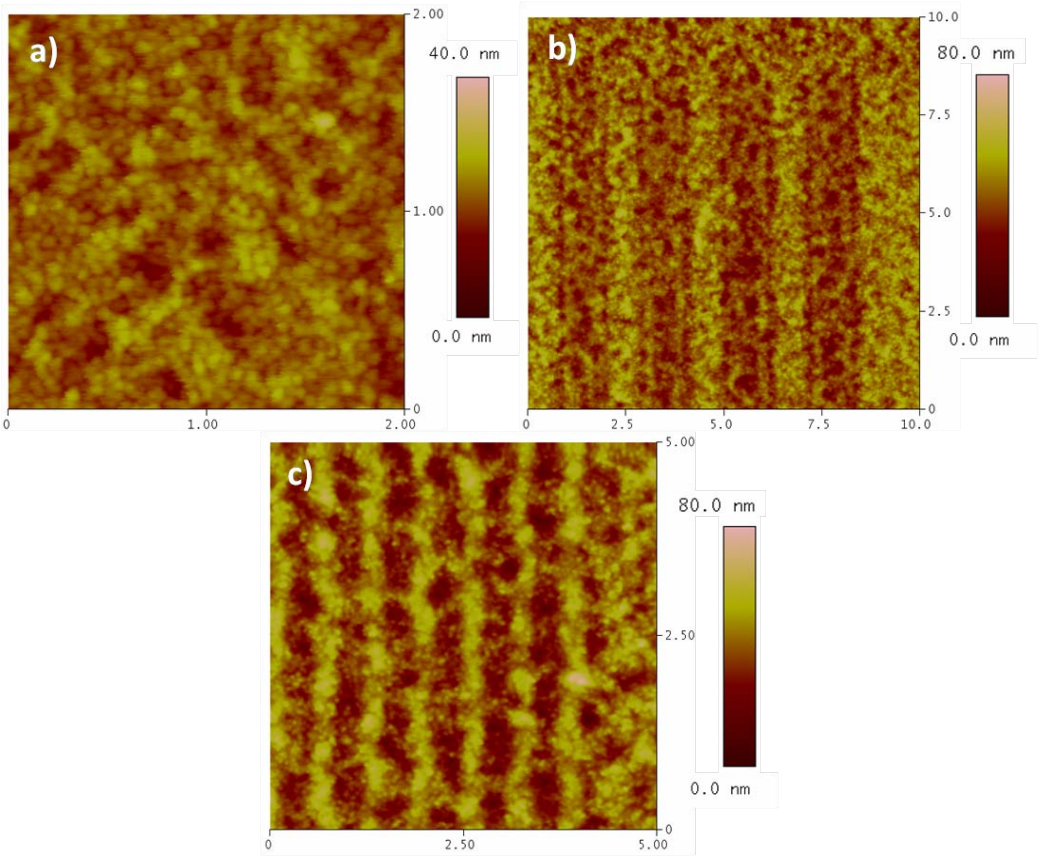

Figure 2.6 a) The PHEMA-*b*-PS diblock brush before patterning. b) 1 µm channels with 1 µm pitch patterned into the diblock brush. c) 300 nm channels with 600 nm pitch patterned into the diblock brush.

achievable can be made by investigating different development conditions. Furthermore, we showed that this direct patterning technique could uniquely create sub-surface patterned brushes. By exploiting the fact that the polymer chains are tethered to the substrate, using a system where the upper layer is a cross-linkable, negative tone resist with a scissionable, positive tone under layer, nano-channels could be directly written. In the next chapter, we use this technique to create patterned binary brushes and show how these binary surfaces can exhibit a responsive nature to its environment.

2.4 Acknowledgements

This work was supported by the National Science Foundation under agreement DMR-0518785. We also acknowledge Cornell NanoScale Science and Technology Facility (CNF) and the Cornell Center for Materials Research (CCMR) for use of their facilities.

REFERENCES

1. Milner, S. T., *Science* **1991,** *251*, 905.

2. Zhao, B.; Brittain, W. J., *Progress in Polymer Science* **2000,** *25*, 677.

3. Van der Waarden, M. J., *Journal of Colloid Science* **1950,** *5* (4), 317.

4. Pinto, J. C.; Whiting, G. L.; Khodabakhsh, S.; Torre, L.; Rodriguez, A. B.; Dalgliesh, R. M.; Higgins, A. M.; Andreasen, J. W.; Nielsen, M. M.; Geoghegan, M.; Huck, W. T. S.; Sirringhaus, H., *Advanced Functional Materials* **2008,** *18* (1), 36.

5. von Werne, T. A.; Germack, D. S.; Hagberg, E. C.; Sheares, V. V.; Hawker, C. J.; Carter, K. R., *Journal of the American Chemical Society* **2003,** *125* (13), 3831.

6. Andruzzi, L.; Senaratne, W.; Hexemer, A.; Sheets, E. D.; Ilic, B.; Kramer, E. J.; Baird, B.; Ober, C. K., *Langmuir* **2005,** *21* (6), 2495.

7. Adiga, S. P.; Brenner, D. W., *Nano Letters* **2005,** *5* (12), 2509.

8. Shen, Y.; Zhan, Y.; Tang, J.; Xu, P.; Johnson, P. A.; Radosz, M.; van Kirk, E. A.; Murdoch, W. J., *American Institute of Chemical Engineers* **2008,** *54* (11), 2979.

9. Chen, M.; Briscoe, W. H.; Armes, S. P.; Cohen, H.; Klein, J., *ChemPhysChem* **2007,** *8* (9), 1303.

10. Gupta, B.; Plummer, C.; Bisson, I.; Frey, P.; Hilborn, J., *Biomaterials* **2002,** *23*, 863.

11. Senaratne, W.; Andruzzi, L.; Ober, C. K., *Biomacromolecules* **2005,** *6* (5), 2427.

12. Jones, D. M.; Smith, J. R.; Huck, W. T. S., *Adv. Mater.* **2002,** *14*, 1130.

13. Tsujii, Y.; Ejaz, M.; Yamamoto, S.; Fukuda, T.; Shigeto, K.; Mibu, K.; Shinjo, T., *Polymer* **2002,** *43* (13), 3837-3841.

14. Kaholek, M.; Lee, W.; LaMattina, B.; Caster, K. C.; Zauscher, S., *Nano Letters* **2004,** *4*, 373.

15. Liu, Y.; Klep, V.; Luzinov, I., *Journal of the American Chemical Society* **2006,** *128* (25), 8106.

16. He, Q.; Kller, A.; Grunze, M.; Li, J., *Langmuir* **2007,** *23* (7), 3981.

17. Patra, M.; Linse, P., *Nano Letters* **2006,** *6* (1), 133.

18. Rastogi, A.; Paik, M. Y.; Tanaka, M.; Ober, C. K., *ACS Nano* **2009,** (Accepted).

19. Austin, M. D.; Zhang, W.; Ge, H.; Wasserman, D.; Lyon, S. A.; Chou, S. Y., *Nanotechnology* **2005,** *16*, 1058.

20. Ruiz, R.; Kang, H.; Detcheverry, F. A.; Dobisz, E.; Kercher, D. S.; Albrecht, T. R.; de Pablo, J. J.; Nealey, P. F., *Science* **2008,** *321*, 936.

21. Cannon Jr, D. M.; Flachsbart, B. R.; Shannon, M. A.; Sweedler, J. V.; Bohn, P. W., *Applied Physics Letters* **2004,** *85* (7), 1241-1243.

22. Matsui, T.; Komatsu, K.; Sugihara, O.; Kaino, T., *Opt. Lett.* **2005,** *30* (9), 970-972.

23. Kim, E.-U.; Baeg, K.-J.; Noh, Y.-Y.; Kim, D.-Y.; Lee, T.; Park, I.; Jung, G.-Y., *Nanotechnology* **2009,** *20* (35), 355302.

24. Ramakrishnan, A.; Dhamodharan, R.; Ruhe, J., *Macromolecular Rapid Communications* **2002,** *23* (10), 612.

25. Jones, D. M.; Huck, W. T. S., *Advanced Materials* **2001,** *13* (16), 1256.

26. Yasin, S.; Hasko, D. G.; Ahmed, H., *Applied Physics Letters* **2001,** *78* (18).

27. Vasilopoulou, M.; Boyatzis, S.; Raptis, I.; Dimotikalli, D.; Argitis, P., *Journal of Materials Chemistry* **2004,** *14*, 3312.

28. Diamanti, S.; Arifuzzaman, S.; Elsen, A.; Genzer, J.; Vaia, R. A., *Polymer* **2008,** *49*, 3770.

29. Lei, C. P.; Long, T.; Obendorf, S. K.; Rodriguez, F., *Polymeric Materials Science and Engineering* **1992,** *66*, 113-114.

30. Song, Q.; Zhang, G.; Wu, C., *Macromolecules* **2007,** *40*, 8061-8065.

31. Zhang, R.; Cherdhirankorn, T.; Graf, K.; Koynov, K.; Berger, R., *Microelectronic Engineering* **2008,** *85*, 1261-1264.

CHAPTER 3

ENVIRONMENTAL RESPONSE OF DIRECTLY PATTERNED BINARY POLYMER BRUSHES

3.0 Introduction

Self-assembled monolayers (SAMs) and polymer brushes have garnered much attention leading to significant research in the past decade.[1-14] As these moeities are covalently attached to the surface, they not only provide the surface with desired functionality but are also robust and resistant to a variety of environments. SAMs and polymer brushes can also achieve dense packing while maintaining relatively smooth surfaces.[15] However, polymer brushes possess a more resilient architecture as they can be grown to larger thicknesses than SAMs, insuring complete surface coverage and an increase in overall density of the functional groups of interest. While polymer brushes have been considered in a variety of applications such as electronics,[9] anti-fouling coatings,[16] and bio-selective surfaces,[10] patterned polymer brushes can be exploited further to create surfaces with tailored surface properties.

Various patterning methods have been used to fabricate patterned polymer brushes. The most conventional methods involve patterning of surface immobilized initiator followed by surface initiated polymerization. The more popular initiator patterning techniques include microcontact printing,[17-20] nano-imprint lithography,[21] and chemical lithography.[22] However, limited work involving the fabrication of patterned binary brushes has been demonstrated in the literature. Hawker *et al.* demonstrated that with the combination of surface initiated polymerization (SIP) and photolithography, a surface with discrete hydrophobic and hydrophilic domains could be generated.[23] By irradiating a poly(*tert*-butyl acrylate) brush surface covered with a

photoresist loaded with a photoacid generator sensitive to 248 nm light, the acid generated in the exposed regions could react with the underlying polymer brush to produce domains of poly(acrylic acid). Zhou and coworkers used a two step process to generate patterned binary surfaces of poly(methyl methacrylate) (PMMA) and poly(2-hydroxyethyl methacrylate) (PHEMA) as small as 50 μm. They directly patterned PMMA brushes through a transmission electron microscope grid with UV light to etch the brush at a rate of 10 nm/hr followed by SIP of a second monomer.[24] Luzinov *et al.* demonstrated a technique involving no irradiation to fabricate patterned binary brush surfaces.[25] Using capillary force lithography, a patterned mask of polystyrene (PS) was generated and initiator immobilization and subsequent polymerization was done to produce the first patterned brush. The PS layer was then removed and initiator was grafted to the bare substrate followed by SIP of the second monomer.

In this chapter we report a different approach towards producing high resolution patterned binary polymer brushes of PMMA and PEGMA. The method we use involves the direct patterning, detailed in the previous chapter, of the first polymer brush using electron beam lithography, a technique capable of yielding patterns as small as 20 nm. The initial patterning is followed by immobilization of initiator to the exposed patterned substrate and then SIP of the second monomer. Figure 3.1 illustrates the binary polymer brush fabrication process used. In contrast to the methods reported thus far in the literature, this new method yields advantages in the fact that the ultimate resolution of the features patterned are in the nanometer regime and the patterning process is done in a single step. The polymerization reaction as a result does not have the reaction environment limitation which is present in the capillary force lithography approach.

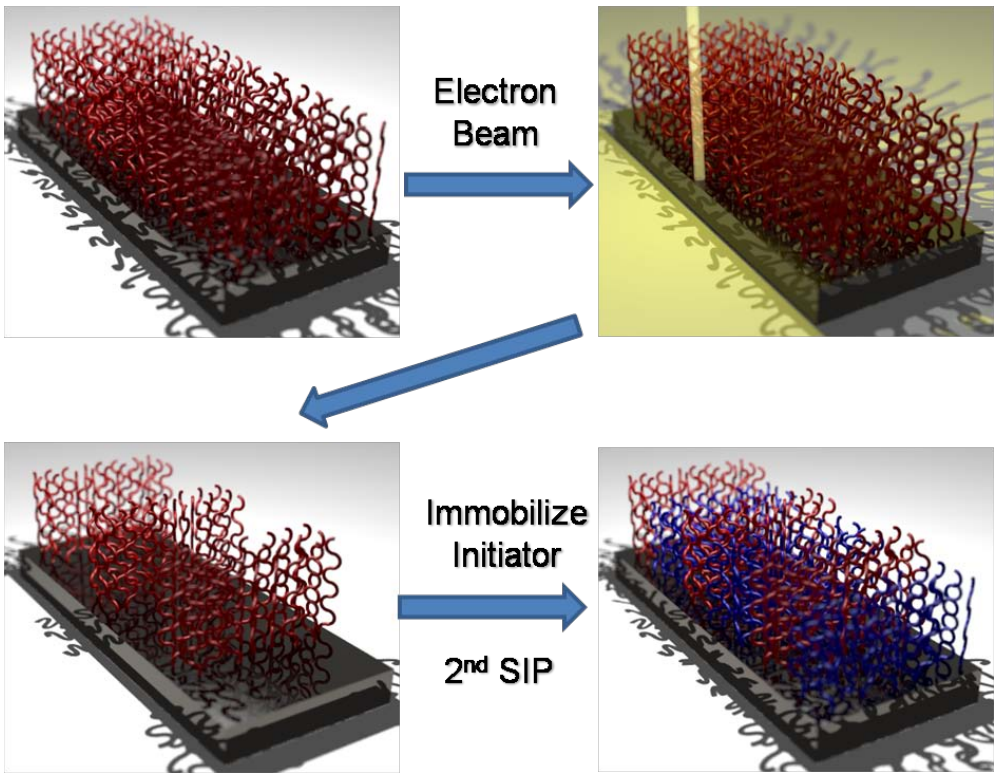

Figure 3.1 Illustration of the patterned binary brush fabrication process.

Additionally, we report the environmentally responsive nature of these binary brushes by immersion in water. By immersing the thin films in different environments, the brushes undergo swelling or contraction, possibly allowing one polymer to dominate the surface as shown in Scheme 3.1. Such responsive surfaces are relevant in areas such as biotechnological and biomedical applications,[26, 27] sensors,[28] chemical gating,[29] and anti-fouling.[30] We demonstrate this reconstructive behavior in PMMA/PHEMA patterned binary brushes immersed in water and characterize the changes occurring with underwater AFM.

3.1 Experimental

Materials. Allyl-2-bromo-2-methylpropionate, chlorodimethyl- hydrosilane, Pt on activated carbon (10 wt %), triethylamine, copper (I) bromide, copper (II) dibromide, 2,2′-bipyridine, inhibitor remover, anhydrous toluene, sodium azide, methyl methacrylate (MMA) and poly(ethylene glycol) methyl ether methacrylate (PEGMA) (average number-average molecular weight 475) were purchased from Sigma Aldrich and used without purification unless stated otherwise. MMA and PEGMA were passed through inhibitor remover and basic alumina, respectively, before use. Deionized water with a resistivity of 18.2 MΩ•cm at 25 °C was obtained from Millipore's Milli-Q® Synthesis A10 system. All the other solvents were purchased from Fisher Scientific. Doped silicon wafers were obtained from Montco Silicon Technologies, Inc. The ATRP initiator was prepared according to the literature, and was stored as a stock solution in anhydrous toluene (concentration 0.5 M).

Immobilization of initiators. A four-inch whole wafer was first treated with Piranha solution (H_2SO_4/30% H_2O_2 , v:v = 7:3) for 40 minutes, to remove any organic residues on the surface and generate silanol groups. After rinsing with large amount of

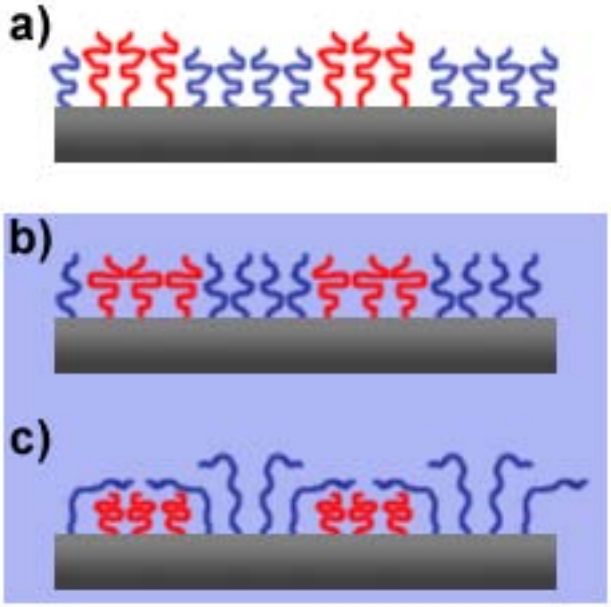

Scheme 3.1 Illustration of the reconstruction occurring within the patterned binary polymer brush in response to its environment. a) Original patterned binary brush. b) After immersion in a solvent that swells one of the polymers and causes the other polymer brush to start taking a "mushroom" conformation. c) After immersion for a longer time. The polymer which dislikes the solvent compresses further, while the other polymer has fully swollen and covered the surface.

deionized water, it was washed with ethanol and dichloromethane, and then dried in a vacuum oven for 10 min at 120 °C. The clean Si wafer was then immersed in a toluene solution of the silane initiator (2 mM) and triethyamine (0.05 mM) for 24 h. Afterwards, the wafer was removed from the solution and washed with water, ethanol and dichloromethane and was kept in dichloromethane overnight. It was dried by the nitrogen flow before the polymerization.

Preparation of PMMA brush. PMMA brushes were prepared using a literature procedure.[31] After the polymerization, the polymer brush on the whole wafer was rinsed with ethanol and dichloromethane, and further dried by nitrogen flow. Small pieces of PMMA brush wafers (2cmx1cm) were cut from the whole wafer for further use.

Deactivation of the PMMA chain-end. Four pieces of PMMA brushes were placed in the sodium azide/N, N-dimethyl formamide (40mg/20mL) for 24 hours. The wafers were then washed with deionized water, ethanol and dichloromethane, and dried in nitrogen flow.

Patterning of the PMMA brushes by electron beam lithography. Patterning of the PMMA brushes were done using the JEOL 9300 electron beam lithography system at the Cornell Nanoscale Science and Technology Facility (CNF). Patterning conditions as reported in previous studies were used.[32] Pattern profiles were confirmed using the Veeco Dimension 3100 scanning probe microscope.

Re-immobilization of initiators. ATRP initiator was re-immobilized to the patterned PMMA brushes using the procedures described above for the whole wafer.

Preparation of PMMA/PPEGMA binary brushes. PPEGMA were grown form the patterned area of the PMMA brush. In a typical procedure, PEGMA (5g) and deionized water (5mL) were mixed in a pear-shaped flask and purged with argon for 30min. A Schlenk-tube loaded with Copper (I) bromide (71.5mg), copper (II)

dibromide(7.5 mg) and 2,2′-bipyridine (156mg) was subjected to three pump/argon purge cycles (each for 20min). One piece of re-immobilized patterned PMAA brush was put in another Schlenk-tube and was also subjected to the pump/argon purge cycle for 3 times (each for 20min). The solution was then transferred to the tube with the catalysts and ligand by a cannula in the protection of argon. The mixture was vigorously stirred for 15min before transferred to the tube with the wafer. The tube was then sealed and kept in oil bath (temperature 32^{o}C) for varying times, depending on the desired thickness. The wafer was then taken out and rinsed with water, ethanol and dichloromethane. It was finally dried by nitrogen flow.

Characterization of Polymer Brushes. Thicknesses of the PMMA polymer brushes were measured using a Woollam variable angle spectroscopic ellipsometer at a 70° angle of incidence. A Cauchy model (Cauchy layer/silicon substrate) was used to fit the data, in which the Cauchy layer was representative of the polymer brush. PMMA brushes with an ellipsometric thickness of ~90 nm were used in this study. Tapping mode underwater AFM was done using the Molecular Imaging PicoPlus Scanning Probe Microscope. Images of the patterned binary brush surfaces were taken before immersion in DI water, after 30 minutes of immersion, and after 3 hours of sonication in water. MAClever type I probes were used to acquire topographic images in air at room temperature.

3.2 Results and Discussion

In this work we demonstrate the ability to create patterned binary brushes of PMMA and PEGMA in two steps with nanometer resolution. PMMA is a conventional positive tone electron beam resist and based on our previous experience involving these brushes, this polymer was chosen as the directly patternable polymer

brush.[32] PEGMA was chosen to backfill the patterned regions as this polymer can readily swell in water.

PMMA brushes were grown on a entire wafer via surface initiated polymerization using a literature procedure.[31] Direct patterning of PMMA brush-covered wafer pieces was done using electron beam lithography, under conditions reported in our previous brush patterning study.[32] Characterization of the surface topography after direct patterning was carried out using AFM. Figure 3.2 shows 100 nm lines with 200 nm pitch patterned into the PMMA brush.

In order to optimize the polymerization of the PEGMA brush to create a flat, patterned binary brush surface, surface initiated ATRP was performed on bare silicon regions with various reaction times. Figure 3.3 shows the ellipsometric thickness versus reaction time for the PEGMA brush. With this information, we tailored the reaction time to yield a PEGMA brush of thickness similar to the starting PMMA brush thickness. After patterning the PMMA brush, ATRP initiator was immobilized onto the exposed areas, and surface initiated polymerization of PEGMA was carried out to create a patterned binary surface. Figure 3.4 shows the AFM image of the patterned binary surface. The contrast in the phase image proves we have distinct patterned regions of two materials. Using this two step patterning and polymerization process, a patterned binary surface was fabricated with nanometer resolution.

To demonstrate the responsive nature of patterned binary brushes, the PMMA/PEGMA brushes were immersed in DI water and underwater AFM was done to probe the changes occurring at the surface. The patterned surfaces were imaged after being immersed for 30 minutes and after 3 hours of sonication. The 3 hour sonication time was chosen as a result of a study done by Chang et al., where they had observed a compaction of a film of PMMA brushes after sonication in DI water for 3 hours.[33] Figure 3.5 shows the underwater AFM images of the patterned surface

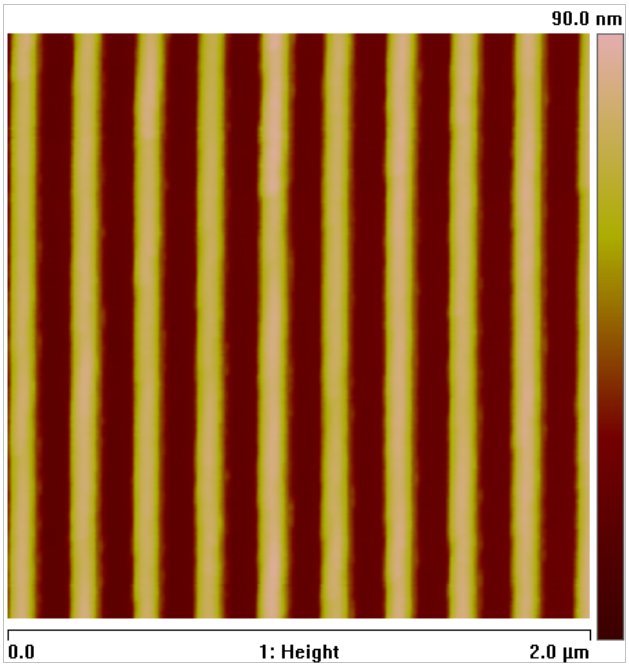

Figure 3.2 AFM image of 100 nm lines with 200 nm pitch patterned into a PMMA brush.

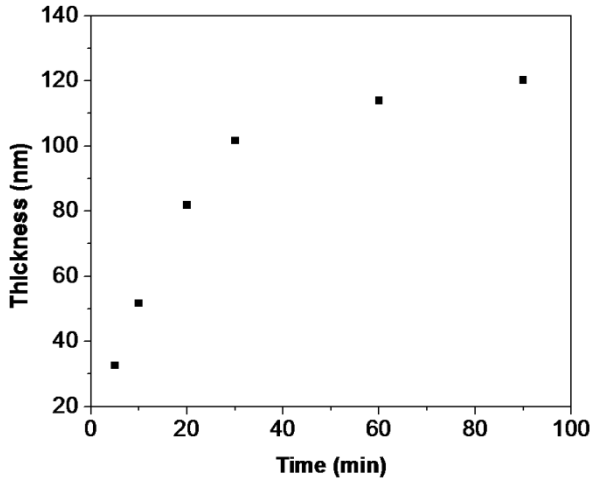

Figure 3.3 Ellipsometric thickness of the PEGMA brush versus polymerization reaction time. A linear increase in brush thickness over time suggests that the brush growth is controlled.

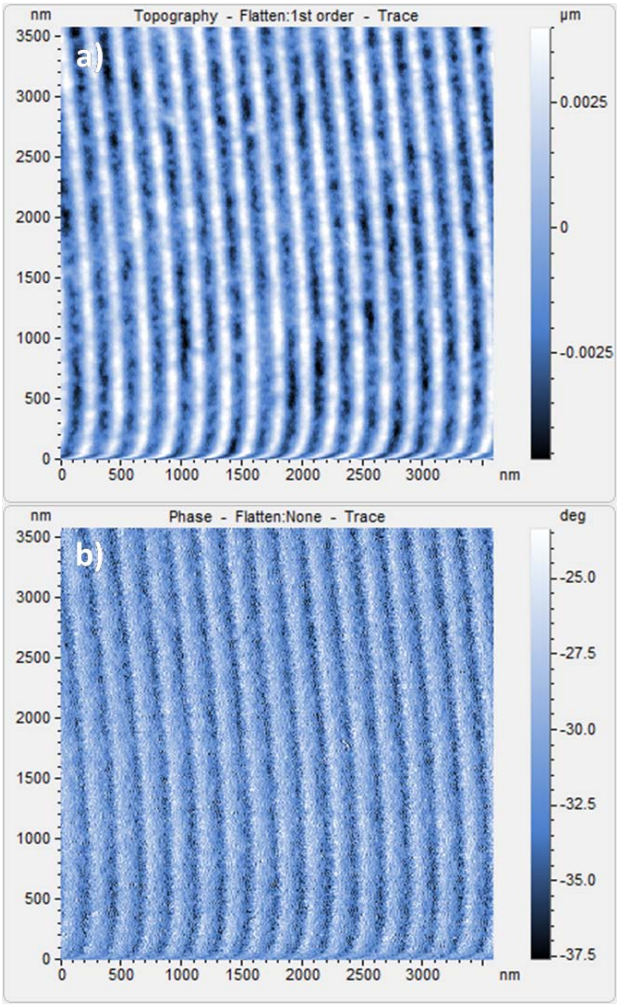

Figure 3.4 AFM image of the patterned binary PMMA/PEGMA brush. a) The height image shows there is only a slight height difference between the polymer regions. b) The phase image confirms the two regions are two distinct materials.

before, after 30 minutes of immersion, and after 3 hours of sonication. The pattern dimensions are 100 nm with 200 nm pitch. As illustrated in Scheme 1, the PMMA brush regions are initially thicker than the PEGMA regions. After immersion in water for 30 minutes, the PEGMA becomes swollen and the film thickness difference between the two regions is decreased. Also, the phase image possesses a more homogeneous surface, possibly due to the PEGMA beginning to swell over the PMMA region. After sonication, the PMMA regions have become thinner due to the compaction of the chains from prolonged exposure to a bad solvent. Thus, the PEGMA regions are now thicker than the PMMA regions, as observed from the AFM height image. In addition, the phase image shows an even more homogeneous surface as the contrast is almost completely gone. This suggests the surface is completely covered by the PEGMA brush, completely switching the surface from a binary surface to an essentially PEGMA surface.

3.3 Conclusion

We have shown the ability to fabricate patterned binary polymer brush surfaces using ATRP and a two step process. Also, using PMMA/PEGMA patterned binary brushes, we have demonstrated that these surfaces can undergo virtual switching at the surface when immersed in water. We used underwater AFM to show the responsive nature of these surfaces. In the future, complimentary evidence could be achieved using a method described in chapter 5. In future work, we also plans to show how patterns with much larger length scales than reported here can resist total surface reconstruction as the swollen polymer chains cannot completely cover the other polymer regions. By tailoring the pattern length scales, one can design surfaces which will undergo surface reconstruction, or possess patterned regions of different functionality.

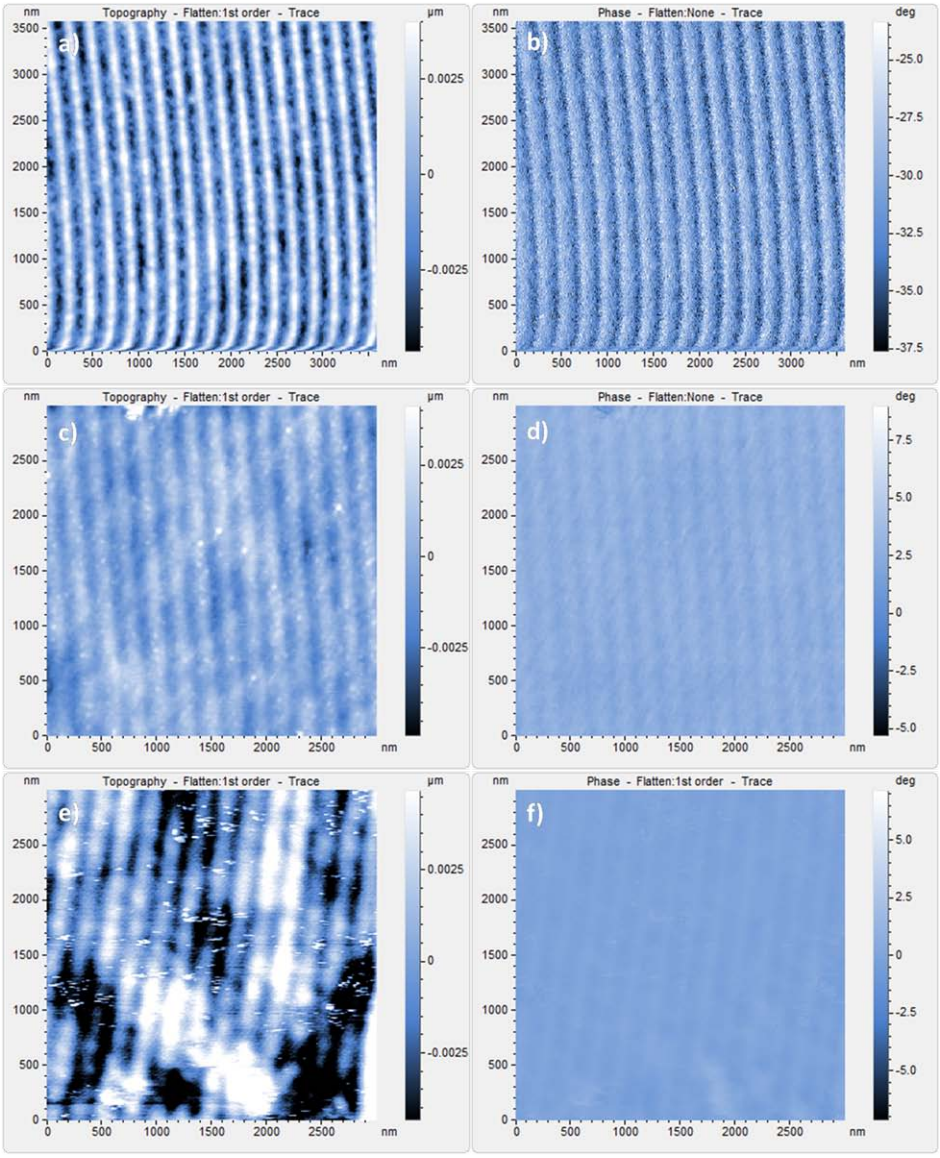

Figure 3.5 AFM of 100 nm lines with 200 nm pitch patterned PMMA/PEGMA binary brushes. a,c,e) The height image before, after being immersed in DI water for 30 minutes, and after being sonicated in DI water for 3 hours. b,d,f) The corresponding phase images.

3.4 Acknowledgements

This work was supported by the National Science Foundation under agreement DMR-0518785. We also acknowledge Cornell NanoScale Science and Technology Facility (CNF) and the Cornell Center for Materials Research (CCMR) for use of their facilities.

REFERENCES

1. de Boer, B.; Hadipour, A.; Mandoc, M. M.; van Woudenbergh, T.; Blom, P. W. M., *Advanced Materials* **2005,** *17* (5), 621.

2. Campbell, I. H.; Kress, J. D.; Martin, R. L.; Smith, D. L.; Barashkov, N. N.; Ferraris, J. P., *Applied Physics Letters* **1997,** *71* (24), 3528.

3. Tokuhisa, H.; Liu, J.; Omori, K.; Kanesato, M.; Hiratani, K.; Baker, L. A., *Langmuir* **2009,** *25* (3), 1633.

4. Furuya, M.; Haramura, M.; Tanaka, A., *Bioorganic and Medicinal Chemistry* **2005,** *14* (2), 537.

5. Senaratne, W.; Andruzzi, L.; Ober, C. K., *Biomacromolecules* **2005,** *6* (5), 2427.

6. Hutt, D. A.; Liu, C., *Applied Surface Science* **2005,** *252* (2), 400.

7. Alagta, A.; Felhosl, I.; Bertoti, I.; Kalman, E., *Corrosion Science* **2008,** *50* (6), 1644.

8. Ladd, J.; Zhang, Z.; Chen, S.; Hower, J. C.; Jiang, S., *Biomacromolecules* **2008,** *9* (5), 1357.

9. Pinto, J. C.; Whiting, G. L.; Khodabakhsh, S.; Torre, L.; Rodriguez, A. B.; Dalgliesh, R. M.; Higgins, A. M.; Andreasen, J. W.; Nielsen, M. M.; Geoghegan, M.; Huck, W. T. S.; Sirringhaus, H., *Advanced Functional Materials* **2008,** *18* (1), 36.

10. Andruzzi, L.; Senaratne, W.; Hexemer, A.; Sheets, E. D.; Ilic, B.; Kramer, E. J.; Baird, B.; Ober, C. K., *Langmuir* **2005,** *21* (6), 2495.

11. Adiga, S. P.; Brenner, D. W., *Nano Letters* **2005,** *5* (12), 2509.

12. Shen, Y.; Zhan, Y.; Tang, J.; Xu, P.; Johnson, P. A.; Radosz, M.; van Kirk, E. A.; Murdoch, W. J., *American Institute of Chemical Engineers* **2008,** *54* (11), 2979.

13. Chen, M.; Briscoe, W. H.; Armes, S. P.; Cohen, H.; Klein, J., *ChemPhysChem* **2007,** *8* (9), 1303.

14. Gupta, B.; Plummer, C.; Bisson, I.; Frey, P.; Hilborn, J., *Biomaterials* **2002,** *23*, 863.

15. Mansky, P.; Liu, Y.; Huang, E.; Russel, T. P.; Hawker, C., *Science* **1997,** *275* (5305), 1458.

16. Glinel, K.; Jonas, A. M.; Jouenne, T.; Leprince, J.; Galas, L.; Huck, W. T. S., *Bioconjugate Chem.* **2009,** *20*, 71-77.

17. Alarcon, C. d. l. H.; Farhan, T.; Osborne, V. L.; Huck, W. T. S.; Alexander, C., *Journal of Materials Chemistry* **2005,** *15* (21), 2089-2094.

18. Jones, D. M.; Smith, J. R.; Huck, W. T. S., *Adv. Mater.* **2002,** *14*, 1130.

19. Ma, H.; Hyun, J.; Stiller, P.; Chilkoti, A., *Advanced Materials* **2004,** *16* (4), 338-341.

20. Chen, T.; Zhang, J.; Chang, D. P.; Garcia, A.; Zauscher, S., *Advanced Materials* **2009,** *21* (18), 1825-1829.

21. Jhaveri, S. B.; Beinhoff, M.; Hawker, C. J.; Carter, K. R.; Sogah, D. Y., *ACS Nano* **2008,** *2* (4), 719-727.

22. He, Q.; Kller, A.; Grunze, M.; Li, J., *Langmuir* **2007,** *23* (7), 3981.

23. Husemann, M.; Morrison, M.; Benoit, D.; Frommer, J.; Mate, C. M.; Hinsberg, W. D.; Hedrick, J. L.; Hawker, C. J., *Journal of the American Chemical Society* **2000,** *122*, 1844-1845.

24. Zhou, F.; Jiang, L.; Liu, W.; Xue, Q., *Macromolecular Rapid Communications* **2004,** *25* (23), 1979-1983.

25. Liu, Y.; Klep, V.; Luzinov, I., *Journal of the American Chemical Society* **2006,** *128* (25), 8106.

26. Bajpai, A. K.; Shukla, S. K.; Bhanu, S.; Kankane, S., *Progress in Polymer Science* **2008,** *33* (11), 1088-1118.

27. Alexander, C.; Shakesheff, K. M., *Advanced Materials* **2006,** *18* (24), 3321-3328.

28. Tokareva, I.; Minko, S.; Fendler, J. H.; Hutter, E., *Journal of the American Chemical Society* **2004,** *126* (49), 15950-15951.

29. Tokarev, I.; Minko, S., *Advanced Materials* **2009,** *21* (2), 241-247.

30. Martinelli, E.; Agostini, S.; Galli, G.; Chiellini, E.; Glisenti, A.; Pettitt, M. E.; Callow, M. E.; Callow, J. A.; Graf, K.; Bartels, F. W., *Langmuir* **2008,** *24* (22), 13138-13147.

31. Jones, D. M.; Huck, W. T. S., *Advanced Materials* **2001,** *13* (16), 1256.

32. Rastogi, A.; Paik, M. Y.; Tanaka, M.; Ober, C. K., *ACS Nano* **2009,** (Accepted).

33. Chen, J.-K.; Hsieh, C.-Y.; Huang, C.-F.; Li, P. M.; Kuo, S.-W.; Chang, F.-C., *Macromolecules* **2008,** *41* (22), 8729-8736.

CHAPTER 4

REVERSIBLE MORPHOLOGY CONTROL IN BLOCK COPOLYMER FILMS VIA SOLVENT VAPOR PROCESSING: AN IN SITU GISAXS STUDY

4.0 Introduction

In the previous chapters, I have highlighted how top-down patterning could be used to create patterned polymer thin films. However, with the growing need for controlled fabrication of structures at the nanoscale, the self assembly of block copolymers has also garnered much attention.[1-5] Block copolymers are an attractive alternative to advanced lithographic techniques due to their ability to form a variety of well-defined morphologies with length scales ranging from 10 nm to 100 nm. Not only do the length scales achievable make block copolymers relevant to many nanotechnology applications, but also their chemical structure may be tailored for desired functionality. Thus, self assembled block copolymers have found uses in micro-electronics,[6] storage devices,[5] solar cells,[3] molecular sieves,[7, 8] low-k dielectrics,[9] and organic semi-conductor applications[10, 11] among others.

However, many challenges remain in controlling the ordering of the self-assembled morphologies of block copolymers. Attaining a desired morphology can be difficult as the two blocks must be immiscible for phase separation to occur, and the volume fraction ratio must lie within an appropriate region within the phase diagram.[12, 13] For example, achieving a gyroidal morphology is exceptionally challenging as there is a narrow range of parameters which lead to this regime.[14] Thus, through synthesis alone, morphology control can be difficult to accomplish. Nevertheless, the ability to tune the morphology is attractive. Similarly, ordering can be a complicated issue as well. In certain cases, long range ordering is difficult to

achieve, as thermal annealing cannot be used with block copolymers possessing a lower thermal degradation temperature than glass transition temperature for one or both of the blocks.

The use of solvent annealing, rather than thermal annealing, to induce long range ordering in block copolymer thin films has received recent attention,[4, 5, 15-17] as it not only induces orientation and ordering, but the self-assembled morphology may be tuned as well. The swelling of both blocks provides sufficient mobility for the chains to rearrange.[18] If the chosen solvent displays selectivity to one of the blocks, the resulting volume change in the swollen state may lead to an order-order transition from the bulk morphology. The newly attained phase may then be kinetically trapped upon fast evaporation of the solvent.[4, 19]

The pathway by which the block copolymer undergoes an order-order transition from one morphology to another during the solvent annealing process has not been fully explored. One initial study of selective solvent vapor annealing reports that the transition from cylinders to spheres occurrs due to selective interactions between the solvent vapors and the individual blocks, causing one block to isolate itself resulting in the formation of spherical micelles.[19] Another study reports the solvent vapor annealing of a monolayer of spherical micelles of poly(styrene)-b-poly(4-vinylpyridine) (PS-b-P4VP) in tetrahydrofuran (THF) to control the fusion and fission of the micelles in order to alter the morphology in addition to improving the ordering of the self assembled structures.[20] However, in our study we are able to provide better insight as to what is occurring during the solvent annealing process.

We have previously reported the use of solvent annealing to induce long-range ordering in thin films of poly(α-methylstyrene)-*block*-poly(4-hydroxystyrene), or PαMS-b-PHOST.[4, 21] Annealing in THF and acetone vapors not only enhances ordering but also controls the morphology in the swollen and dried films: the

nonselective THF vapor leads to a cylindrical morphology with parallel orientation, while PHOST-selective acetone leads to a spherical morphology which can be kinetically-trapped upon solvent evaporation.[4] Previously we have demonstrated that films of PαMS-*b*-PHOST can be reversibly tuned between lying cylinders and ordered spheres by choice of annealing solvent with alternating solvent anneal sessions with THF and acetone.[4, 21] In this chapter, detailed insight into the mechanism of morphology formation and ordering of the self-assembled domains in solvent vapor through the use of in situ grazing incidence small angle X-ray scattering (GISAXS) is provided.[22-26] Using GISAXS to probe the film interior during the solvent annealing process in combination with using a film thickness monitor,[26, 27] a correlation between swelling ratio, solvent, and annealing time can be made. Here we show that sufficient chain mobility must be available to the polymer and the appropriate volume fraction ratio must be attained in order for ordering and morphology change to occur during solvent treatment.

4.1 Experimental

Polymer Synthesis. Poly(α-methylstyrene)-*block*-poly(tert-butoxystyrene) (PαMS-*b*-PtBuOS) was synthesized via sequential anionic polymerization; PαMS-*b*-PHOST is formed by subsequent deprotection, following a procedure described elsewhere in literature.[4, 8, 28]

Sample Preparation and Annealing. PαMS-*b*-PHOST was dissolved in propylene glycol monomethyl ether acetate (PGMEA, Aldrich) to make a 5% (w/v) solution. Thin films were prepared by spin-coating the solution at 2000 rpm onto silicon wafers. The wafers were then cut to 20mm x 20mm pieces to prepare samples of the appropriate dimension for in situ studies. Solvents (either THF or acetone) were

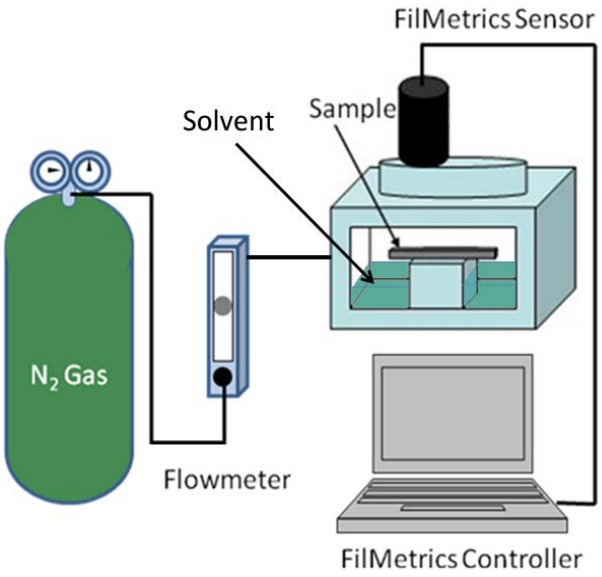

Scheme 4.1 Experimental setup of the in situ solvent annealing GISAXS study.

injected into a small chamber, and a controlled nitrogen counterflow determined the degree of swelling (Scheme 4.1).[26] The flow rates of the nitrogen were controlled using a Cole Parmer Aluminum Flowmeter with a high-resolution valve (143 sccm maximum flow for nitrogen). Film thickness was monitored using a Filmetrics F20 spectroscopic reflectometer. Rapid drying of the film is achieved by opening the sealed annealing chamber, which results in a rapid (less than 1 second) evaporation of the solvent, as observed visually by a change in optical appearance of the film.

Characterization. Synthesized polymer molecular weights were measured using gel permeation chromatography (GPC). Four Waters Styragel HT columns operating at 40˚C and Waters 490 ultraviolet (254 nm wavelength) and Waters 410 refractive index detectors were used to take the measurements. The PαMS block was found to have number average molecular weight (Mn) 7 kg/mol; the PαMS-b-PtBuOS was found to be 30.5 kg/mol, corresponding to a PHOST block M_n of 16 kg/mol after deprotection. Thus we refer to this PαMS-b-PHOST polymer as 7K/16K. Complete deprotection is confirmed using FTIR. Film topology and surface morphology were characterized using a Veeco Dimension 3100 Atomic Force Microscope in tapping mode.

GISAXS experiments were conducted at the Cornell High Energy Synchrotron Source (CHESS) at station G1, with initial results collected at D1 station. G1 station provides a high flux x-ray beam (typically 10^{13} photons/sec/mm^2) from a 50-pole wiggler in combination with a multilayer monochromator (2% band width) and harmonic rejection mirrors. A 2D Quantum 1 CCD detector was used to capture the scattered images at a beam energy of 10 keV. All images were taken at an incident angle (α_i) of 0.16 degrees, which is slightly higher than the critical angle (α_{cp}) of the polymer film. GISAXS images were taken at periodic increments of time to probe any changes occurring within the film. Because the beam was found to crosslink the film

after an exposure of several seconds, thus locking the morphology in the exposed spot, the film was moved slightly for each new exposure.[22]

The sample was housed in a custom-made vapor cell with an integrated film thickness monitor[26] that could be mounted on the sample goniometer (Scheme 4.1). The cell has inlets for liquid solvent as well as for nitrogen gas flow, and the solvent vapor concentration in the cell was controlled by adjusting the nitrogen flow rate. The in situ film thickness monitor is based on an optical spectroscopic reflectometer (Filmetrics F20). The spot on the film probed by the light beam of the instrument was not exposed to x-rays.

4.2 Results and Discussion

In this work we probe how the reorganization of the self-assembled domains occurs via solvent vapor annealing as well as the mechanism of reorganization using in situ real time GISAXS experiments. We studied the annealing of as-spun films in THF and acetone vapors, as well as the reversible control of the morphology by alternating annealing the films from one solvent to the next.

PαMS-b-PHOST with similar PαMS volume fraction, though larger molecular weight, directly spin-coated from PGMEA was previously found to form perpendicular cylinders, though without long range hexagonal packing.[4, 8] GISAXS and AFM confirm the same behavior for the 7k/16k polymer used here (Figure 4.1). The Bragg rods indicate a perpendicular cylinder morphology of the PαMS minor phase formed upon evaporation of the spinning solvent (Figure 4.1a). The presence of weak first order peaks suggests that while the cylinders are all oriented perpendicular to the sample surface, there is only short-range ordering laterally. The AFM image of the as-spun surface, as seen in Figure 4.1b, is in agreement with the GISAXS interpretation. The lighter dots observed in the AFM image are consistent with the

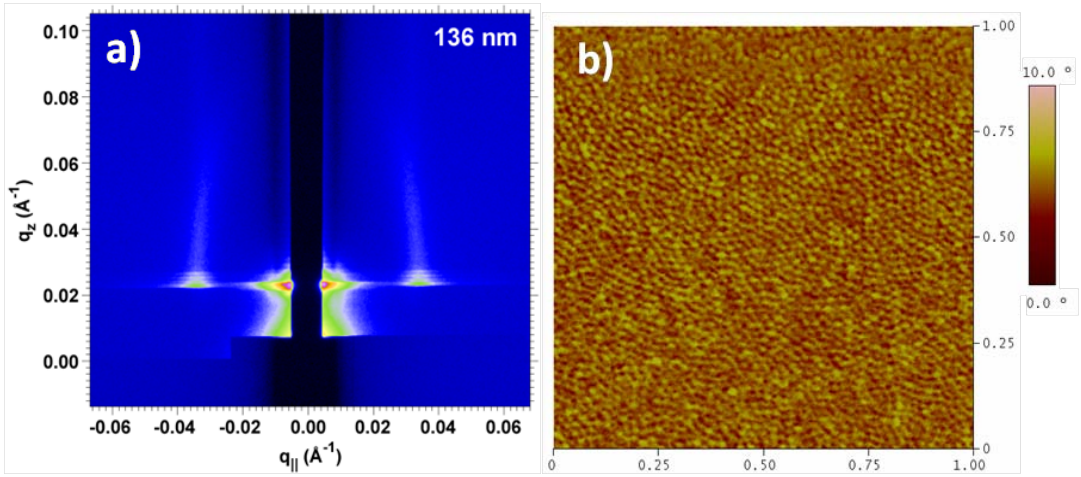

Figure 4.1 A film of PαMS-*b*-PHOST spin coated from PGMEA. a) The GISAXS profile of the as-spun block copolymer film. The Bragg rods suggests a perpendicular cylindrical morphology, however, the absence of additional ordered peaks indicates short-range ordering of the cylinders. b) The corresponding AFM phase image confirms the morphology. The contrast scale for this image is 10˚.

tops of perpendicular PαMS cylinders, and the lack of long-range hexagonal packing of these dots is consistent with the short-range order found in the GISAXS results.

Solvent annealing films of the 7k/16k PαMS-b-PHOST films used here in THF and acetone leads to the same behavior reported previously for similar molecular weights.[4, 21] Similar to our previous study, ex-situ solvent annealing experiments with THF leads to parallel cylinder formation, while annealing in acetone leads to a face-centered orthorhombic (FCO) spherical morphology kinetically trapped in the film after rapid drying. We interpret the FCO structure to be the result of uniaxial shrinkage of an equilibrium BCC spherical morphology in swollen films upon drying.[4]

4.2.1 Anneal in THF.

PαMS-*b*-PHOST films with a thickness far larger than the block period were used, in order to be able to distinguish spherical morphologies from perpendicular cylindrical morphologies via GISAXS; here, the periodicity of the block copolymer is 18.8 nm (by AFM) and the film thickness 136 nm (film thickness monitor). THF is a good solvent for both PαMS and PHOST, and thus we expected the blocks to swell nonselectively and the cylindrical morphology to be maintained.[29]

The solvent annealing apparatus is shown in Scheme 4.1.[26] Solvent is injected into the chamber through a Teflon capillary tube, and the vapor swells the film. A nitrogen gas counterflow controlled by a flowmeter moderates the solvent vapor concentration in the chamber and provides a very precise method of controlling the degree of swelling in the film. The film thickness was measured in situ with a spectroscopic reflectometer, and thus facilitates a direct correlation of GISAXS images with the degree of swelling.

From previous ex-situ observations of PαMS-*b*-PHOST swollen in THF, reordering is understood to occur due to the increased mobility the solvent vapor

imparts onto the individual polymer chains.[4] In order to better understand the nonselective solvent annealing mechanism, the films were swollen and held at several thicknesses before rapid drying of the film in air.

In the initial experiment, the PαMS-b-PHOST film was swollen to 214 nm (157% of the original thickness) and held for 20 minutes before drying the film to its original thickness. Within 8 minutes, the film thickness quickly increased to 174 nm, during which time the Bragg rods disappeared, leaving a featureless scattering image, seen in Figure 4.2a. The morphology present prior to annealing was disrupted upon the rapid swelling of the film, and no further peaks appeared during the remaining time as the thickness rose to 214 nm. Upon drying, the Bragg rods returned, but the overall intensity of those peaks had diminished significantly. While the film swelled to over 150% of its original thickness, there was apparently insufficient plasticization to induce any reordering of the self-assembled domains. The block copolymer film appears to have simply swelled and de-swelled, maintaining its previous cylindrical morphology and with perpendicular orientation, albeit with slightly less order, as suggested by slightly weaker scattering in the dried film.

The initial perpendicular orientation may be the result of solvent concentration gradients, as reported by Kim and Libera for fast evaporation during spin coating.[30] While this metastable structure has some stability with regard to gentle vapor processing, the perpendicular morphology is never obtained again after extended solvent processing in acetone and THF, as we will describe in the following.

To impart sufficient mobility to the chains for reorganization, a second film was swollen further to 297 nm (218% swelling) and held for 20 minutes. Like before, the Bragg rod intensity dropped within seconds upon swelling and completely disappeared after 16 minutes of the initial solvent injection, at a thickness of 216 nm (Figure 4.3a). However, upon reaching a thickness of 272 nm (200%), peaks

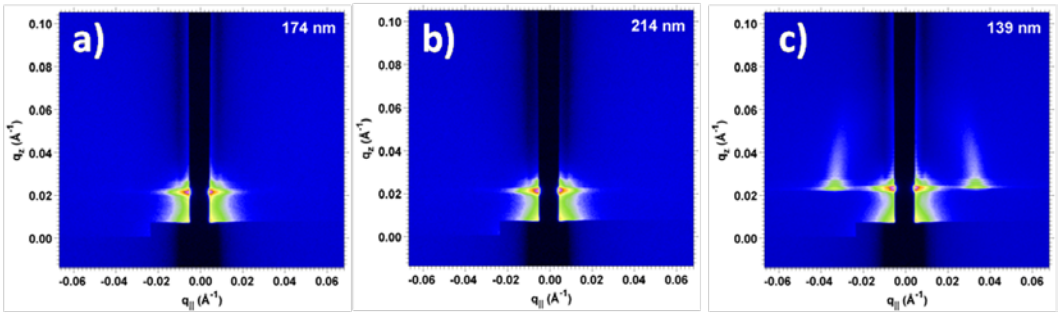

Figure 4.2 In situ swelling of the block copolymer film with THF vapor as seen with GISAXS. a) The first-order peak disappears within 8 minutes of initial swelling suggesting the short range ordering that existed prior to annealing was disrupted during the rapid swelling of the film, and b) no further peaks form even after 20 minutes with a gradual increase in swelling. c) Upon rapid drying of the film, the peaks returns to a standing cylinder morphology, similar to the as-spun film reform. This behavior indicates that the swelling was insufficient for a change in morphology or orientation.

reappeared at the same $q_{\|}$ position as the as-spun film, indicating that the initial perpendicular cylinder structure still exists but the periodic ordering had been obscured by the rapid swelling (Figure 4.3b). As the film swells further (288 nm, 212%) a new set of peaks appears in a different position, one on the Yoneda peak and one above the Yoneda peak (Figure 4.3c), and the new peaks grow stronger while the initial peaks fade and disappear (Figure 4.3d). Upon solvent evaporation, secondary peaks appear indicating parallel cylinder morphology (Figure 4.3e). The Bragg peaks in the dried films are again significantly shifted and elongated along q_z, both effects indicating an anisotropic shrinkage due to the evaporation of the film.

The preferential attraction of one of the blocks to the substrate, or a large difference in surface tension favoring alignment of the lower surface energy block at the air interface, has been known to drive parallel orientation in block copolymer thin film morphologies.[31, 32] In this case, the re-appearance of the initial peak followed by its disappearance and the appearance of new peaks gives insight into the mechanism of morphology reorientation in the swollen film from perpendicular to parallel cylinders. The initial peaks corresponding to perpendicular cylinders faded, while the new peaks corresponding to parallel cylinders appeared independently and became more intense. This suggests the possibility that the perpendicular cylinders coalesced with nearby perpendicular cylinders to form new parallel cylinders. The absence of an intermediate ring structure between the first peaks and the second peaks indicates that the initial perpendicular cylinders did not simply tilt over to become parallel cylinders.

Upon evaporation of the solvent, the initial Bragg rods did not re-appear, while peaks indicating cylinders oriented parallel to the surface remained. The double peak seen in Figure 4.3e can be attributed to the scattering of the direct beam and the reflected beam for $\alpha_i > \alpha_{cp}$: the peak in scattering intensity, thus, appears as a doublet and can be modelled within the framework of the distorted-wave Born approximation

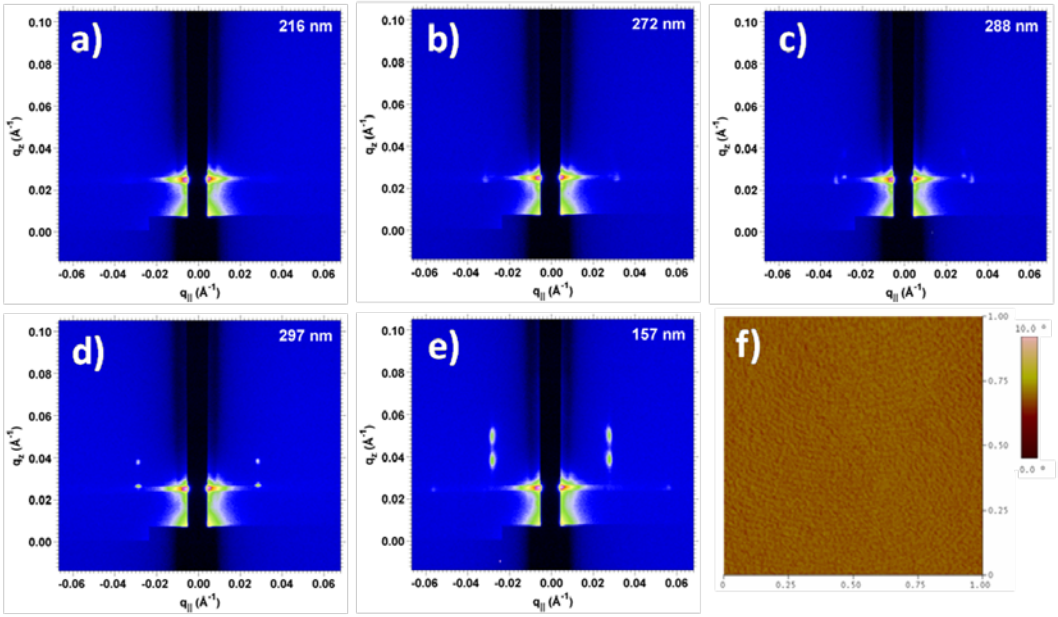

Figure 4.3 In situ swelling of the block copolymer thin film with THF vapor to a larger swelling ratio. a) 18 minutes after beginning controlled swelling, the swelling in the film results in a disappearance of Bragg rods, indicating a disordered film. b) As the swelling reaches 200%, peaks form on the Yoneda band in a similar position as the Bragg rods in the as-spun film. c) Upon further swelling, a new set of peaks form, both on the Yoneda and above the Yoneda, while the original peak begins to fade. d) The newly-formed peaks become more intense, while the first peak has fully faded, indicating fully formed morphology with a distinct parallel orientation. e) Quickly drying the film trapped in the swelled morphology and orientation, with the dried GISAXS pattern indicating the formation of parallel cylinders with shrinkage perpendicular to the substrate. f) AFM phase image after THF solvent vapor annealing. A change from perpendicular cylinders to parallel cylinders can be seen.

(DWBA).[33, 34] By swelling the films to 218% of the original thickness, the swollen polymer was sufficiently plasticized for self-reorganization to occur. The selective attraction of blocks to the air and substrate interfaces is expected to induce parallel orientation of cylinders, as observed here.[35]

An interesting thing to note is that the peak positions of the dried annealed film suggest an almost hexagonally-packed cylinder morphology, consistent with scattering from parallel cylinders as seen in literature.[36] However, the q_z positions of the elevated peaks do not lie at the exact position where scattering from a hexagonally packed lattice would appear. The theoretical positions of the peaks should lie at q_z = 0.0296 Å and 0.0385 Å, but the actual position is q_z = .0382 Å and .0498 Å. The discrepancy can be attributed to a uniaxial contraction in the fast drying the film.[4] In the swollen state, the film is expected to be ordered with parallel hexagonally-packed cylinders, but upon drying of the film the cylinders become compressed in the direction normal to the film surface. This compression causes the elevated peaks to shift to a slightly higher q_z position than what is expected for a perfect hexagonal lattice. After taking into account the 42% shrinkage from the swollen state upon drying along the substrate normal, the theoretical and experimental q_z positions appear to match well with the theoretical q_z = 0.0389 Å and 0.0493 Å.

Figure 4.3f shows the morphology of the film after annealing in THF vapor; the fingerprint pattern present in the AFM phase image confirms the change from perpendicular to parallel cylinders. The nearest neighbor spacing of the cylinders in the AFM image was found to be 23.3 nm, and this spacing is in good agreement with the modeled positions of the GISAXS peaks. Using a compressed hexagonally packed lattice model, the nearest neighbor spacing was found to be 22.5 nm. Comparisons between the nearest neighbor distances of the self-assembled structures obtained from AFM and GISAXS are shown in Table 4.1.

Table 4.1 The in-plane nearest-neighbor distances (nm) of the various self-assembled structures as obtained by AFM and GISAXS.

	Standing cylinders As-spun	Lying cylinders THF annealed	BCC(110) spheres Acetone Annealed	BCC(110) spheres THF → Acetone Annealed	Lying Cylinders Acetone → THF Annealed
AFM	18.8 ± 2.4	23.3 ± 2.0	24.2 ± 3.2	25.1 ± 2.7	23.2 ± 1.5
GISAXS	18.6 ± 1.7	22.5 ± 0.8	23.3 ± 1.1	23.5 ± 1.1	22.4 ± 0.9

4.2.2 Anneal in Acetone

Acetone, while a solvent for both PαMS and PHOST, displays a preference for the PHOST majority component, and annealing in this solvent causes an order-order phase transition from a cylindrical morphology to a spherical one.[4] Previous ex-situ work confirmed that annealing in acetone resulted in a face-centered orthorhombic spherical structure within the film upon drying. Similar to annealing in THF, a critical swelling ratio was required in acetone annealing before the polymer chains were sufficiently mobile for reordering to occur. We speculate for an order-order transition to occur, not only do the chains require adequate mobility to reorganize, but each block must also be swelled to posses the appropriate volume ratio within the polymer phase diagram which is the driving force of the transition.

In situ GISAXS images were once again taken at an incident angle $\alpha_i = 0.16^\circ$, higher than the critical angle of the film (Figure 4.4). The film thickness of the samples prior to annealing for this experiment was found to be 146 nm (film thickness monitor). Swelling to 392 nm (268% of the original thickness) was needed in order to obtain sufficient chain mobility for self assembly, larger than the necessary swelling ratio seen from the THF annealing process (218%). This phenomenon may be understood in terms of the solvent selectivity for the two blocks. In order for the block copolymer to have sufficient mobility to self assemble via solvent vapor annealing, both blocks must be sufficiently swollen such that the glass transition temperature (T_g) of the block drops below the annealing temperature (here, room temperature).[37] An extension to Dimarzio *et al.* thermodynamic model explaining the glass transition temperature depression due to a diluent was done by Chow.[38, 39] He showed for small molecule solvents, the size and concentration of the diluents were the main determinants affecting the drop in the glass transition temperature. Further evidence

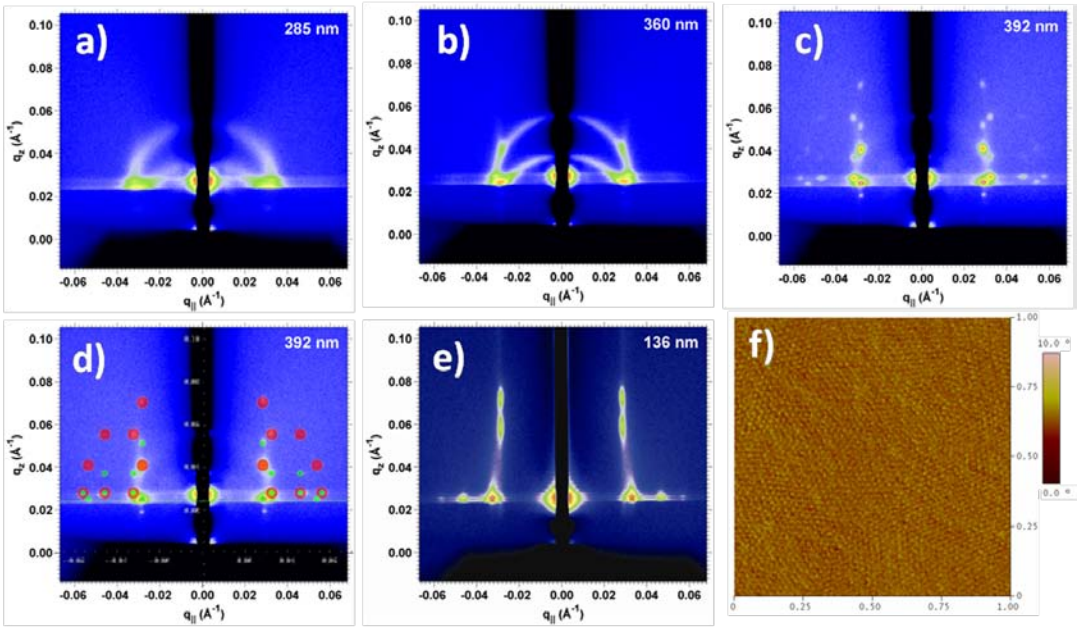

Figure 4.4 a-c) In situ swelling of the block copolymer thin film in acetone vapor. Upon swelling to a ratio of 2.47, a change from cylinders to spheres begins. After keeping the film swelled above 360 nm for one hour, individual peaks can be seen indicating a spherical morphology. d) Scattering from the swollen, spherical film along with an overlay of the modeled scattering from a stretched BCC lattice. e) The GISAXS profile of the dried film. Scattering consistent with a FCO spherical morphology is observed. f) AFM height image after processing in acetone vapor. The height scale is 10 nm.

for the glass temperature depression under solvent vapor uptake and its role in block copolymer thin film kinetics was recently provided be Di *et al*.[40]

The T_g of PHOST was measured to be 180-190˚C,[4] and while the T_g of PαMS is difficult to measure due to its thermal degradation, the value is known to be approximately 170C [41] - hence both values are significantly higher than room temperature. In the case of the nonselective THF solvent, even swelling of both blocks leads to their plasticization with minimal swelling. Acetone, however, would be expected to swell the PHOST block far beyond the value needed for plasticization, before the PαMS block swells sufficiently for its T_g to be suppressed below room temperature. Alongside with the mobility increase, a sufficiently high PHOST volume fraction must be achieved that acts as the driving force for the phase transition.

At the start of the swelling process, the Bragg rods, once again, disappear (not shown). However, rings appear at a thickness of 285 nm, indicating the formation of a phase-separated morphology, though one lacking directional orientation (Figure 4.4a). As the swelling ratio is taken above what is necessary for reordering to occur in THF vapors, the polymer can be sufficiently plasticized to start reorganizing. The film thickness was slowly raised until additional changes were seen to occur in the scattered GISAXS images. Individual peaks replaced the ring structure, beginning when the film is 360 nm thick (Figure 4.4b), and the individual peaks obtain maximum intensity when the film thickness is 392 nm (Figure 4.4c). The films were held at this value for 60 minutes, and no further changes were observed.

Our results indicate that holding the film over time at the same swelling ratio does not lead to changes in morphology; instead, the morphology was found to change at very precise swelling ratios, and that the morphology changes are spontaneous once these swelling ratios are achieved. Also worth noting is that no ordered cylindrical morphology is observed in the GISAXS images before scattering from the formation

of ordered spheres appears. This indicates that the block copolymer swells unevenly enough to direct a transition to a spherical morphology before sufficient swelling for mobility is achieved. Note that the spherical phase reflections are not smeared out into arcs; hence the spherical phase is highly oriented with respect to the substrate.

Interestingly, the scattered peaks in the swollen film cannot be modeled by scattering from a BCC lattice. The model only fits when a BCC lattice is stretched in the z direction by 6%, indicating a face-centered orthorhombic (FCO) morphology. We attribute the stretched lattice to the film being freely swollen along the surface normal, whereas swelling in the lateral direction is restricted. The spheres are able to rearrange in the z direction to accommodate the swelling, while being unable to fully rearrange in the lateral direction, resulting in a stretched BCC lattice. Figure 4.4d shows the theoretical scattered peaks from a stretched BCC lattice mapped on top of the actual scattered peaks, which appear to be in agreement. The red dots signify upward splitting, while the green dots signify downward splitting attributed to refraction/reflection effects associated with the DWBA scattering theory.[36, 42] An orthorhombic morphology was observed by Stein et al. in block copolymer films possessing spherical morphology for various film thicknesses, between 4 and 23 layers, as obtained by spin coating and thermal annealing.[43] In our system, we found the vertical distance between the spherical layers to be 20.3 nm with a film thickness of 392 nm, or about 19 layers of spheres. To our knowledge, this is the first observation of this thin film packing behavior in solvent annealed films.

Upon fast drying of the film, the scattering images show that the stretched FCO geometry of the spheres in the fully swollen film appears to change to a compressed, rather than elongated, FCO geometry (Figure 4.4e). The compression from the drying process in the z direction causes the unit cell to shrink in the same direction, causing the FCO lattice to be compressed compared to the BCC bulk phase.

The elongation of the off-specular peaks is further evidence of solvent evaporation. Ideally, spheres would produce scattered peaks which are symmetric in shape, however the peaks seen from the dried films are elongated along q_z suggesting a compression of the spheres in the direction normal to the film surface.

The AFM images in Figure 4.4f show the surface morphology after annealing in acetone vapor. Although dot-like features can be seen when comparing the AFM images between the as-spun and acetone annealed films, we see increased ordering of the dots in Figure 4.4f. Also, the nearest neighbor spacing of 24.2 nm calculated from the power spectral density from the AFM image is in fair agreement with the 23.3 nm obtained from modeling the FCO geometry in the scattered images obtained from GISAXS.

4.2.3 Reversible Morphology Switching

Switching the morphology between spherical and cylindrical morphology is possible via alternating solvent annealing sessions with THF and acetone.[4, 21] Hence it is more accurate to talk in terms of *solvent vapor processing* rather than a simple anneal. Here we demonstrate the mechanism of morphology switching in comparison to processing a film without solvent anneal history, showing that morphology formation is independent of solvent anneal history.

A film previously annealed in acetone vapor was placed in the solvent annealing chamber and subjected to THF vapor processing to take the polymer from a FCO spherical morphology to parallel cylinders. To perform the opposite transition, a film pre-annealed in THF vapor underwent acetone vapor treatment. As before, GISAXS measurements were performed at an angle of incidence above the polymer critical angle, $\alpha_i = 0.16^\circ$, to probe the whole film interior during swelling. The initial

thickness of the films were 131 nm and 144 nm for the pre-annealed acetone film and pre-annealed THF film, respectively.

Figure 4.5 shows the cycle from spherical morphology after acetone treatment to cylindrical morphology after annealing in THF and back to spherical morphology again. The acetone pre-annealed film (Figure 4.5a) was swollen in THF from an initial thickness of 131 nm to 311 nm (237%) and held above this thickness for 60 minutes. As observed previously for THF annealing of an as-spun film, scattering from the spheres was seen to begin disappearing within two minutes as the film rapidly swelled to 168 nm thickness (not shown). Upon further swelling, a single pair of peaks appear on the Yoneda band consistent with the spacing of the parallel cylindrical morphology, and in contrast to the two sets of peaks visible in the as-spun film annealed in THF (Figure 4.5b).

Peaks consistent with the initial spherical morphology never reappeared - this was expected as the kinetically trapped (metastable) spherical morphology can now relax back towards the thermodynamically stable cylindrical morphology expected from the block volume fraction of the polymer. Upon reaching a thickness of 311 nm, peaks consistent with a parallel cylinder formation emerge, accompanied by the typical peak splitting when the angle of incidence is above the critical angle of the film, though below the critical angle of the substrate (Figure 4.5c). Scattering consistent with parallel cylinders is observed in the film after drying, and the film returns to the same dried-state thickness (Figure 4.5d). The peak positions are also in agreement with THF vapor processing of an as-spun film.

Annealing a THF pre-annealed film (Figure 4.5e) in acetone vapors reveals a subtly different behavior. Instead of the scattered peaks from the parallel cylinders disappearing in the initial couple minutes of rapid swelling, as in the case of the as-spun film, rings slowly appear suggesting the emergence of randomly oriented

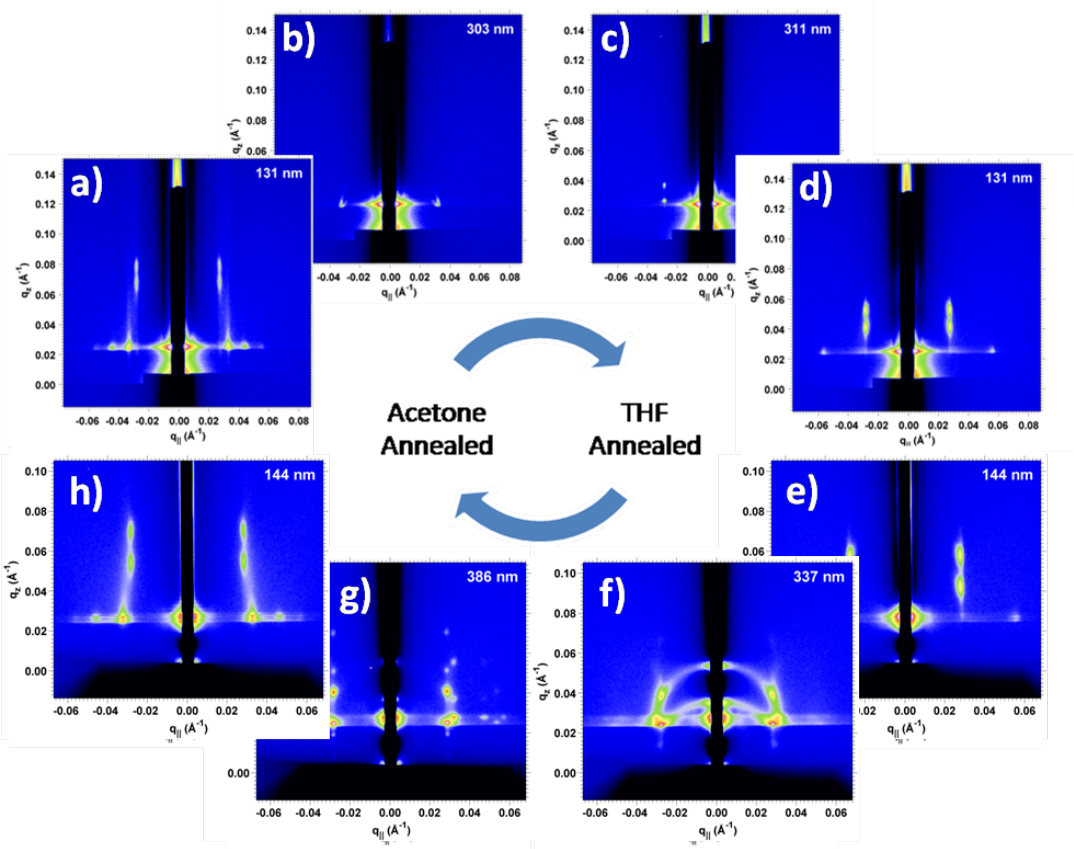

Figure 4.5 Reversible morphology control through solvent processing as probed in situ and in real time with GISAXS. Thin films with spherical morphology obtained through acetone vapor treatment are shown to transition to parallel cylinders upon THF vapor annealing, and returned to a spherical morphology upon successive exposure to acetone vapor.

cylinders. The absence of a sudden transition is not unreasonable, as the cylindrical morphology is stable for this particular block copolymer sample. When the film swelled to 370 nm (257%), additional scattered peaks started appearing while the rings became more faint. The film thickness was sustained above 370 nm for about 1 hour. As seen previously in the as-spun film annealed in acetone, peaks consistent with an FCO lattice appear in the swollen state, corresponding to a BCC lattice stretched in the direction perpendicular to the film plane. Upon drying the film, the observed GISAXS image reveals FCO spheres indicating, again, vertical shrinkage of the film during drying.

The peak positions for the double solvent processed films are in good agreement with the initial structures obtained by vapor processing as-spun films. Comparison of the nearest neighbor (NN) spacings of the self-assembled structures between the solvent processed films is shown in Table 4.1. The relation between NN distances of lying cylinders and BCC (110) spheres is in good agreement with a classic study of the bulk morphology by Hashimoto and coworkers.[44] They studied the thermoreversible morphological transition between cylinders and spheres of polystyrene-*block*-polyisoprene. In their observations, they noticed that the (110) d-spacing of a BCC spheres lattice, d_{110}^{BCC}, was equal to the (100) d-spacing of the hexagonal cylinders lattice, d_{100}^{HEX}. Relating the hexagonal and BCC nearest neighbor distances to the d-spacings results in $d_{NN}^{BCC} = 1.061\ d_{NN}^{HEX}$.

Comparing the lateral NN spacings of our annealed films to the results of Hashimoto's work, we see that they are compatible with each other and that $d_{110}^{BCC} = d_{100}^{HEX}$ holds for our samples as well. In addition we analyzed the associated AFM images of the films, and again arrived at the same conclusion. Hence the phase change in our vapor processed films must have followed a similar mechanism as determined for the thermal cycling in the bulk study.

4.3 Conclusion

Solvent vapor treatment is a powerful processing technique that enables direct control over the morphology and ordering within block copolymer thin films. Not only have we demonstrated with PαMS-b-PHOST the ability to direct the morphology of self-assembled domains to hexagonally packed cylinders or FCO spheres, but we have shown that the process is completely reversible. Moreover, the ability to anneal films on a faster timescale than conventionally needed for thermal annealing offers an additional advantage for solvent annealing.

In order to exploit the benefits of solvent annealing completely, the mechanism must be fully understood. We have shown for the annealing process to take effect, the polymer must be swollen sufficiently for ordering to occur - the polymer must be plasticized sufficiently for the polymer chains to be mobile enough to reorganize at room temperature. For the order-order transition to occur, the additional variable of solvent selectivity enables tuning of the block volume fraction, and thus the morphologies formed. In the response of an acetone annealed film to THF annealing, the quick relaxation away from the kinetically trapped spherical morphology was observed in contrast to the as-spun annealed films. Morphology of films annealed in both acetone and THF from directly spin-coated films are indistinguishable from films solvent processed previously. Evaporation of the solvent results in compression of the film thickness, but the morphology is otherwise maintained in the dried films.

4.4 Acknowledgements

This work was supported by the National Science Foundation Materials World Network (award DMR 0602821) and the NSF NIRT (award CTS 0304159), and the Semiconductor Research Consortium. MYP was supported by the National Science Foundation (award DMR 0518785) and JKB was supported by fellowships from

Motorola and IBM. ELS appreciates support by the Semiconductor Research Corporation. This work was performed using facilities at the Cornell High Energy Synchrotron Source (CHESS), the Cornell Center for Materials Research (CCMR), and The Cornell NanoScale Facility (CNF). CHESS is supported by the NSF and the National Institutes of Health/National Institute of General Medical Sciences under NSF award DMR-0225180. CCMR is supported by NSF award DMR 0520404, part of the NSF MRSEC Program. CNF, a member of the National Nanotechnology Infrastructure Network, is supported by NSF award ECS-0335765.

REFERENCES

1. Segalman, R. A., *Materials Science and Engineering: R: Reports* **2005,** *48* (6), 191-226.

2. Tang, C.; Lennon, E. M.; Fredrickson, G. H.; Kramer, E. J.; Hawker, C. J., *Science* **2008,** *322* (5900), 429-432.

3. Crossland, E. J. W.; Kamperman, M.; Nedelcu, M.; Ducati, C.; Wiesner, U.; Smilgies, D.-M.; Toombes, G. E. S.; Hillmyer, M. A.; Ludwigs, S.; Steiner, U.; Snaith, H. J., *Nano Letters* **2008,** *0* (0), Article ASAP.

4. Bosworth, J. K.; Paik, M. Y.; Ruiz, R.; Schwartz, E. L.; Huang, J. Q.; Ko, A. W.; Smilgies, D.-M.; Black, C. T.; Ober, C. K., *ACS Nano* **2008,** *2* (7), 1396-1402.

5. Park, S.; Lee, D. H.; Xu, J.; Kim, B.; Hong, S. W.; Jeong, U.; Xu, T.; Russell, T. P., *Science* **2009,** *323* (5917), 1030-1033.

6. Xue, C.; Meador, M. A. B.; Zhu, L.; Ge, J. J.; Cheng, S. Z. D.; Putthanarat, S.; Eby, R. K.; Khalfan, A.; Bennett, G. D.; Greenbaum, S. G., *Polymer* **2006,** *47*, 6149-6155.

7. Zhang, R.; Yokoyama, H., *Macromolecules* **2009,** *42*, 3559-3564.

8. Li, M.; Douki, K.; Goto, K.; Li, X.; Coenjarts, C.; Smilgies, D. M.; Ober, C. K., *Chemistry of Materials* **2004,** *16* (20), 3800-3808.

9. Lee, B.; Yoon, J.; Oh, W.; Hwang, Y.; Heo, K.; Jin, K. S.; Kim, J.; Kim, K.-W.; Ree, M., *Macromolecules* **2005,** *38* (8), 3395-3405.

10. Braga, D.; Horowitz, G., *Advanced Materials* **2009,** *21*, 1473-1486.

11. Iovu, M. C.; Zhang, R.; Cooper, J. R.; Smilgies, D. M.; Javier, A. E.; Sheina, E. E.; Kowalewski, T.; McCullough, R. D., *Macromolecular Rapid Communications* **2007,** *28* (17), 1816-1824.

12. Bates, F. S.; Fredrickson, G. H., *Physics Today* **1999,** *52* (2), 32-38.

13. Cochran, E. W.; Garcia-Cervera, C. J.; Fredrickson, G. H., *Macromolecules* **2006,** *39*, 2449-2451.

14. Okumura, A.; Nishikawa, Y.; Hashimoto, T., *Polymer* **2006,** *47*, 7805-7812.

15. Olszowka, V.; Hund, M.; Kuntermann, V.; Scherdel, S.; Tsarkova, L.; Boker, A., *ACS Nano* **2009,** *3* (5), 1091-1096.

16. Kim, S. H.; Misner, M. J.; Xu, T.; Kimura, M.; Russell, T. P., *Advanced Materials* **2004,** *16* (3), 226-231.

17. Kim, T. H.; Hwang, J.; Hwang, W. S.; Huh, J.; Kim, H.-C.; Kim, S. H.; Hong, J. M.; Thomas, E. L.; Park, C., *Advanced Materials* **2008,** *20* (3), 522-527.

18. Cavicchi, K. A.; Berthiaume, K. J.; Russell, T. P., *Polymer* **2005,** *46*, 11635-11639.

19. Peng, J.; Kim, D. H.; Knoll, W.; Xuan, Y.; Li, B.; Han, Y., *The Journal of Chemical Physics* **2006,** *125*, 064702.

20. Kim, T. H.; Huh, J.; Hwang, J.; Kim, H.-C.; Kim, S. H.; Sohn, B.-H.; Park, C., *Macromolecules* **2009,** *42* (17), 6688-6697.

21. Bosworth, J. K.; Black, C. T.; Ober, C. K., *ACS Nano* **2009,** *3* (7), 1761-1766.

22. Smilgies, D.-M.; Busch, P.; Posselt, D.; Papadakis, C. M., *Synchrotron Radiation News* **2002,** *15* (5), 35-42.

23. Xu, T.; Goldbach, J. T.; Misner, M. J.; Kim, S.; Gibaud, A.; Gang, O.; Ocko, B.; Guarini, K. W.; Black, C. T.; Hawker, C. J.; Russell, T. P., *Macromolecules* **2004,** *37* (8), 2972-2977.

24. Kim, S. H.; Misner, M. J.; Yang, L.; Gang, O.; Ocko, B. M.; Russell, T. P., *Macromolecules* **2006,** *39* (24), 8473-8479.

25. Papadakis, C. M.; Di, Z.; Posselt, D.; Smilgies, D.-M., *Langmuir* **2008,** *24* (24), 13815-13818.

26. Smilgies, D.-M.; Li, R.; Di, Z.; Darko, C.; Papadakis, C. M.; Posselt, D., *Materials Research Society Symposium Proceedings* **2009,** *1147*, 1147.

27. Dourdain, S.; Rezaire, A.; Mehdi, A.; Ocko, B. M.; Gibaud, A., *Physica B: Condensed Matter* **2005,** *357* (1-2), 180-184.

28. Du, P.; Li, M.; Douki, K.; Li, X.; Garcia, C. B. W.; Jain, A.; Smilgies, D.-M.; Fetters, L. J.; Gruner, S. M.; Wiesner, U.; Ober, C. K., *Advanced Materials* **2004,** *16* (12), 953-957.

29. Brandrup, J.; Immergut, E. H.; Grulke, E. A., *Polymer Handbook*. 4th ed.; Wiley: New York, 1999.

30. Kim, G.; Libera, M., *Macromolecules* **1998,** *31* (8), 2569-2577.

31. Anastasiadis, S. H.; Russell, T. P.; Satija, S. K.; Majkrzak, C. F., *Physical Review Letters* **1989,** *62* (16), 1852.

32. Busch, P.; Posselt, D.; Smilgies, D. M.; Rauscher, M.; Papadakis, C. M., *Macromolecules* **2007,** *40* (3), 630-640.

33. Busch, P.; Rauscher, M.; Smilgies, D.-M.; Posselt, D.; Papadakis, C. M., *Journal of Applied Crystallography* **2006,** *39* (3), 433-442.

34. Martinelli, E.; Menghetti, S.; Galli, G.; Glisenti, A.; Krishnan, S.; Paik, M. Y.; Ober, C. K.; Smilgies, D.-M.; Fischer, D. A., *Journal of Polymer Science Part A: Polymer Chemistry* **2009,** *47* (1), 267-284.

35. Wan, L.; Yang, X., *Langmuir* **2009,** *25* (21), 12408-12413.

36. Lee, B.; Park, I.; Yoon, J.; Park, S.; Kim, J.; Kim, K.-W.; Chang, T.; Ree, M., *Macromolecules* **2006,** *38* (4311-4323).

37. van Krevelan, D. W.; Hoftyzer, P. J., *Properties of Polymers: Their Estimation and Correlation Length with Chemical Structure*. 2nd ed.; Elsevier Scientific Publishing Company: New York, NY, 1976.

38. Dimarzio, E. A.; Gibbs, J. H., *Journal of Polymer Science Part A: General Papers* **1963,** *1* (4), 1417-1428.

39. Chow, T. S., *Macromolecules* **1980,** *13* (2), 362-364.

40. Di, Z.; Posselt, D.; Smilgies, D.-M.; Papadakis, C. M., *Macromolecules* **2009,** *43* (1), 418-427.

41. Huang, D.; Simon, S. L.; McKenna, G. B., *The Journal of Chemical Physics* **2003,** *119* (7), 3590-3593.

42. Busch, P.; Rauscher, M.; Smilgies, D.-M.; Posselt, D.; Papadakis, C. M., *Journal of Applied Crystallography* **2006,** *39* (3), 433-442.

43. Stein, G. E.; Kramer, E. J.; Li, X.; Wang, J., *Macromolecules* **2007,** *40* (7), 2453-2460.

44. Sakurai, S.; Hashimoto, T.; Fetters, L. J., *Macromolecules* **1996,** *29*, 740-747.

CHAPTER 5

NEXAFS DEPTH PROFILING OF BLOCK COPOLYMER BRUSHES

5.0 Introduction

Polymer thin films have opened up new possibilities towards creating tailored surfaces for numerous applications. These applications include corrosion resistant coatings,[1] anti-fouling coatings for ship hulls,[2-4] biomedical devices,[5, 6] and micro-electronics.[7, 8] Several techniques have been developed to physically adsorb the polymer film to the substrate. Processes such as spin coating, dip coating, doctor blading, and Langmuir-Blodget techniques are commonly used to prepare films from solution.[9] An alternate approach to create polymer thin films that possess long term stability, even in very adverse environments, involves the tethering of the polymer chains to the substrate via chemical bonds. These thin films are referred to as polymer brushes. Polymer brushes offer the control over chemical functionality and density, improved adhesion stability of the polymer layer, and are well suited for micro- and nano- patterning.

In the design and fabrication of these designer surfaces, surface characterization techniques with sub-nanometer depth resolution are required. Polymer thin films, even only a few nanometers thick, can influence the surface properties of a material so greatly that the chemical nature of the underlying material becomes completely hidden.[10] X-ray photoelectron spectroscopy (XPS) has often been used to determine the composition in the near surface region of polymer thin films.[11-13] With XPS, by using an electron emission angle, φ, of 85° measured from the surface normal, sampling depths as low as 0.5-0.75 nm have been achieved.[14]

Near edge X-ray absorption fine structure (NEXAFS) spectroscopy is also a powerful spectroscopic technique for composition depth profiling, well suited for probing molecules with low atomic number atoms such as C, N, O, and F.[15] NEXAFS uses energy tunable, polarized X-rays from a synchrotron light source. The X-rays can excite a core electron to an unfilled molecular orbital, leaving a hole in the core shell which can be filled by a higher energy level electron, producing an emitted Auger electron. These electrons are then collected to give information about the chemical bonds present within the top few nanometers of a surface. Although the sampling depth is limited to below 5 nm, NEXAFS has exceptional sensitivity to sub-nanometer depth variation in atomic concentrations when scanning the C K-edge. Also, because NEXAFS spectroscopy focuses on molecular orbitals rather than individual elements, differentiation between signals from C-C and C=C bonds can be made due to the presence of the π orbital in the double bond, a capability that XPS does not have.

Very few studies have been done thus far using NEXAFS to determine near surface composition profiles in polymer thin films. To accurately characterize the composition depth profiles, the electron escape depth (EED) must be known. Genzer and coworkers experimentally determined the electron grid bias (EGB) dependent EED for NEXAFS using self-assembled monolayers (SAMs) of $-O_{1.5}Si-(CH_2)_2-(CF_2)_8F$.[16] However, their system relied on the small signal from the very short hydrocarbon segment. Kramer *et al.* determined the EED for NEXAFS by attempting to create a model system of a thin perfluoropolyether layer deposited on highly oriented pyrolytic graphite (HOPG).[17] They varied the angle to explore several sampling depths to model the EED. While their study was highly detailed, the HOPG surface was extremely rough and their samples experienced questionable surface contamination from pump oil.

In efforts to more accurately determine the EED for NEXAFS, we developed a model system consisting of a diblock copolymer brush of a polystyrene (PS) lower block with a very thin poly(trifluoroethyl acrylate) (PTFEA) upper block. Angle resolved NEXAFS was done to measure the Auger electron signal from the $1s \rightarrow \pi^*_{C=C}$ signal of the buried PS layer at various emission angles, thus probing several different sampling depths. Polymer brush synthesis was performed using nitroxide mediated controlled free radical polymerization and determination of the film thickness was done using X-ray reflectometry. We show for our system the ability to determine the EED for NEXAFS without the presence of surface contaminants. Also, due to the controlled synthesis of the polymer brush layers, the interface between the two blocks exhibited low roughness, yielding data with more accuracy than previously reported in literature. With an accurate value for the EED, we would be able to do compositional depth profiling studies to characterize the surface composition of our thin films such as the responsive binary brushes mentioned in chapter 3 or surface active block copolymers used for anti-biofouling applications.

5.1 Experimental

Materials and Chemical Reagents. 2-methyl-2-nitropropane, isobutyraldehyde, zinc (powder), ammonium chloride, phenyl magnesium bromide (3.0 M), copper(II)acetate, 4-vinyl benzyl chloride, sodium acetate, sodium borohydride, Jacobsen's catalyst, 11-bromo-1-undecene, sodium hydride, trichlorosilane, hexachloroplatinic acid were purchased from Sigma Aldrich and used without purification unless stated otherwise. Styrene and trifluoroethyl acrylate were obtained from Aldrich and purified by passing through a short column of MEHQ and HQ inhibitor remover packing material. Deionized water with a resistivity of 18.2 MΩ•cm at 25 °C was obtained from Millipore's Milli-Q® Synthesis A10 system. Anhydrous diethyl ether, dichloromethane, anhydrous dimethylformamide, anhydrous

toluene, anhydrous tetrahydrofuran were obtained from Sigma Aldrich. All other solvents for rinsing and cleaning were purchased from Fisher Scientific. Doped silicon wafers were obtained from Montco Silicon Technologies, Inc.

Synthesis of the Alkoxyamine Initiator. TIPNO (4) was synthesized from 2-methyl-2-nitropropane and isobutyaldehyde using a literature procedure.[18] The alkoxyamine initiator was synthesized from TIPNO and 4-vinylbenzyl alcohol (3) using a literature procedure.[19] Synthesis of 4-vinylbenzyl alcohol was carried out in two simple steps. First, 4-vinylbenzyl acetate (2) was synthesized by acetylation of 4-vinylbenzyl chloride (1) which was reacted with KOH soln for 18 h at room temperature to give 4-vinylbenzyl alcohol in quantitative yield.

Immobilization of the Initiator. The immobilization of the alkoxyamine intiator on silicon surface involved three reactions.

Step 1: *Synthesis of* ***(7)***

Sodium hydride (0.278 g, 11.6 mmol) was added to a solution of the alkoxyamine initiator (2.85 g, 12.16 mmol) in 50 mL dry THF and the reaction mixture was stirred under argon for 15 min. A solution of 11-bromo-1-undecene in 5 mL of dry THF was then added dropwise and the reaction mixture was refluxed for 16 h and evaporated to dryness. The residue was partitioned between 125 mL H_2O and 125 mL of CH_2Cl_2. The aqueous layer was extracted with 2x30 mL of CH_2Cl_2. The combined organic extracts were then dried using $MgSO_4$, filtered and solvent was evaporated. The crude product was purified by column chromatography using 4:3 of hexane:CH_2Cl_2.

Step 2: *Hydrosilylation of* ***(7)***

To a solution of **(7)** in 15 mL $HSiCl_3$, was added a 1:1 ethanol/dimethoxyethane solution of chloroplatinic acid. The reaction mixture was stirred under nitrogen in the dark for 14 h. 5 mL of dry toluene was added and the excess $HSiCl_3$ was removed under vacuum. The crude product was passed through a column of anhydrous

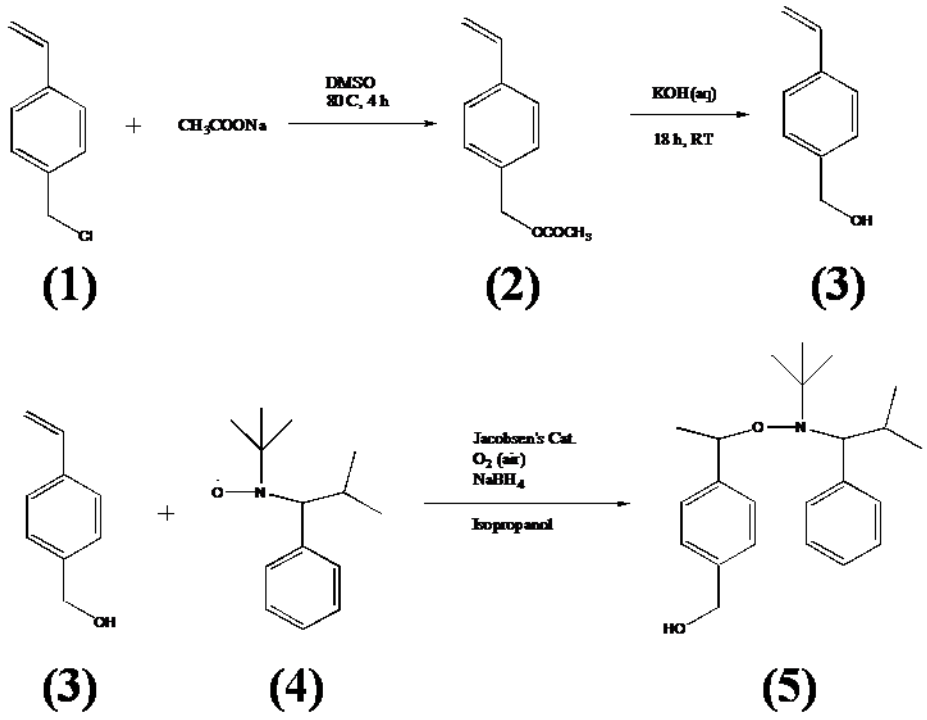

Scheme 5.1 Synthesis of the universal alkoxyamine initiator.

Na_2SO_4, washed with 15 mL CH_2Cl_2. The excess solvent was evaporated off. The product **(8),** dissolved in anhydrous toluene was used without further purification.

Step 3: *Immobilization of the hydrosilated product on silicon surface*

Silicon wafers were diced into 3 cm x 1 cm pieces and cleaned by rinsing with acetone and dried under a nitrogen stream. To remove any organic residues on the surface, the substrates were further cleaned in Piranha solution (3:1 conc. H_2SO_4/30% H_2O_2 soln) for 30 minutes. (*Caution*: piranha solution reacts violently with organic materials and should be handled carefully). After rinsing with copius amounts of deionized water, the substrated were washed with dichloromethane and then dried in a vacuum oven for 10 min at 120 °C. The clean Si wafer pieces were immersed in a toluene solution of the silane initiator (2 mM) and triethyamine (0.05 mM) for 24 h. The wafers were then removed from the solution and washed with dichloromethane and left to stand in dichloromethane for 18 h. The initiator coated wafers were either used immediately or stored under standard conditions. No loss of activity was observed on storage for a couple of weeks.

Preparation of PS Brushes. In a typical reaction, styrene (10.98 g, 105.5 mmol) and DMF were added to a clean, dry air-tight schlenk flask. Four to five freeze thaw cycles were performed. The solution was warmed to room temperature and transferred to another air-tight flask containing the initiator immobilized silicon wafers. Polymerization was carried out for 24 h at 125 °C. After polymerization, the substrates were removed from the flask, washed with toluene and dicholoromethane, and gently sonicated in toluene for one hour and dried under a stream of nitrogen.

Preparation of PS-b-PTFEA Brushes. TFEA monomer (8.13 g, 52.76 mmol) was freeze thawed for four to five cycles in an air-tight schlenk flask. The monomer was then transferred to another air-tight flask containing the PS brushes. Polymerization was done for 30 h at 125 °C. After polymerization, the diblock

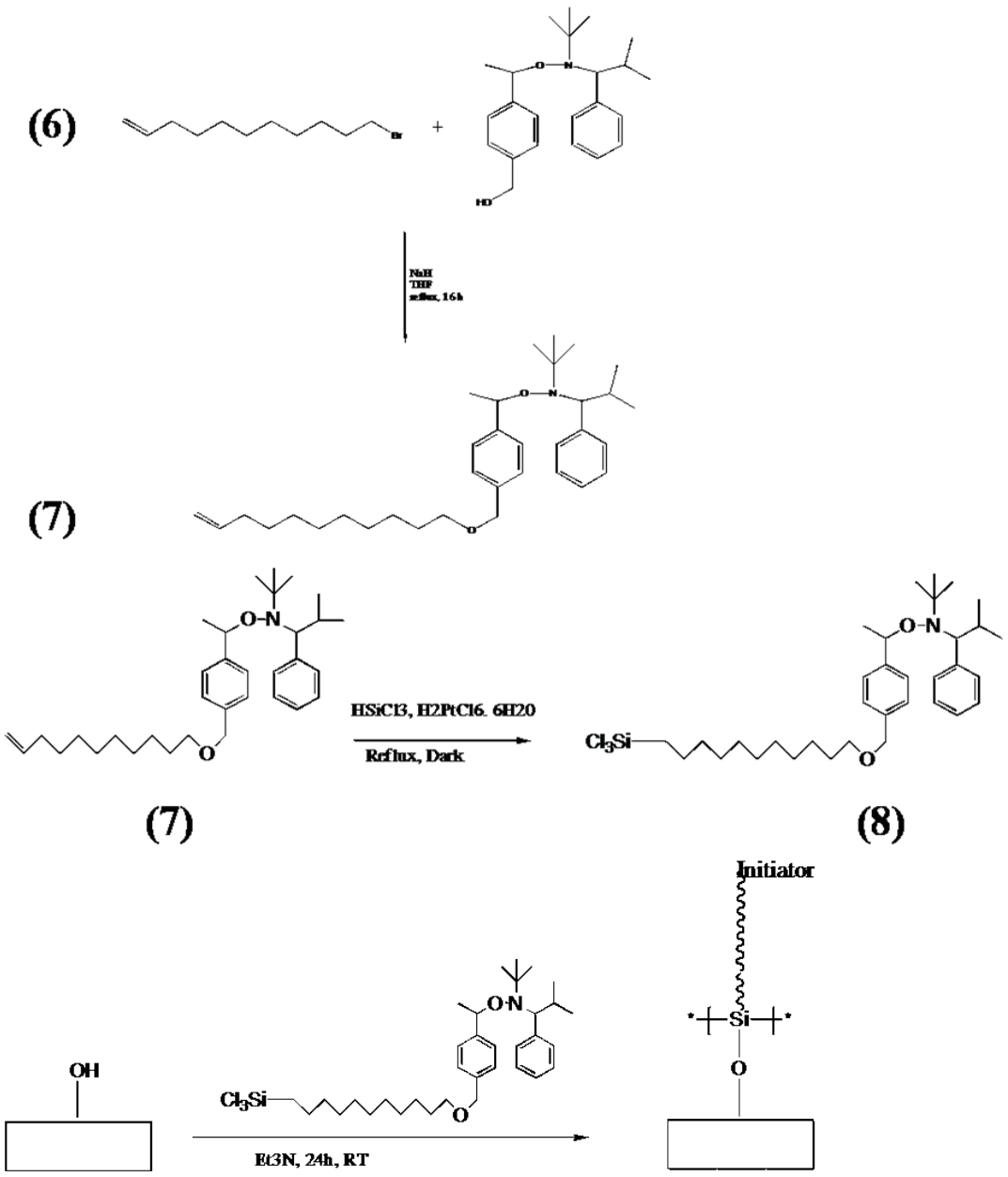

Scheme 5.2 Immobilization of the alkoxyamine initiator on silicon surface.

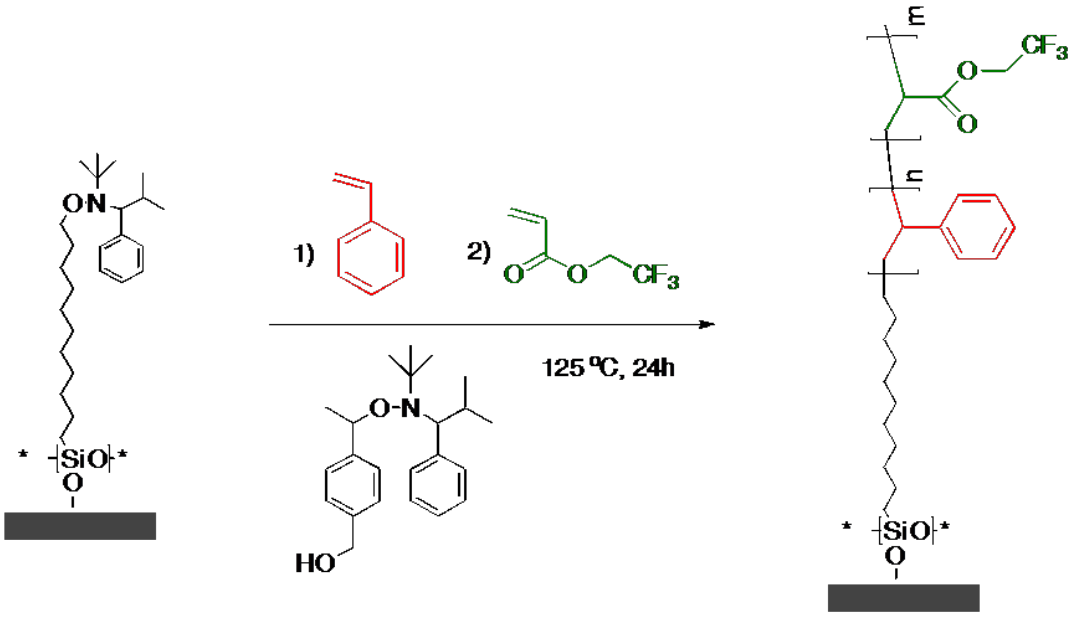

Scheme 5.3 Synthesis of PS-b-PTFEA block copolymer brushes.

copolymer brushes were removed from the flask, washed with toluene, and gently sonicated in toluene for one hour and dried under a stream of nitrogen.

Characterization of Polymer Brushes. Thicknesses of the polymer brushes were measured by X-ray reflectivity (XRR) using a method similar to that of Toney *et al*.[20] Surface topography was analyzed and the root-mean-square (RMS) roughness was measured using a Veeco Dimension 3100 scanning probe microscope. Olympus tapping mode etched silicon probes were used to acquire topographic images in air at room temperature. XPS measurements were performed using a Kratos Axis Ultra with a monochromatic aluminum Kα X-ray source at 1486.6 eV. Charge compensation was carried out using low-energy electrons from a filament.

NEXAFS depth profiling experiments were carried out on the U7A NIST/Dow materials characterization end-station at the National Synchrotron Light Source at Brookhaven National Laboratory. The synchrotron X-ray beam was elliptically polarized (polarization factor, P = 0.85), with the electric field vector predominantly in the plane of the storage ring. The photon flux was about 10^{11} photons/s at a typical storage ring current of 500 mA. A spherical grating monochromator was used to obtain monochromatic soft X-rays at an energy resolution of 0.1 eV. Spectra were acquired at 0.2 eV steps. C K-shell NEXAFS spectra were acquired for photon energy in the range 270-320 eV. The NEXAFS chamber consisted of a sample holder, which was positioned on a computer-controlled goniometer. The sample holder could be rotated about an axis normal to the plane of the storage ring to vary the X-ray incidence angle. NEXAFS spectra were obtained at X-ray incidence angles, θ, varying from 20° to 120°. Each measurement was taken on a fresh spot to minimize possible beam damage effects. Electrons emitted from the surface were collected using a channeltron electron multiplier with an adjustable EGB. The data reported were acquired using a grid bias of -150 V. The negative grid potential prevents

electrons with kinetic energy less than 150 eV from entering the detector. The channeltron partial electron yield (PEY) detector was positioned at an angle, Δ, of 36° with respect to the incoming X-ray beam, and in the equatorial plane of the sample chamber. Thus, the emission angle, φ, is given by $\varphi = \theta + \Delta - 90°$ as seen in Figure 5.1.

To eliminate the effect of incidence beam intensity variations and monochromator absorption features, the PEY signals were normalized by the incidence beam intensity obtained from the photo yield of a clean gold grid. A linear pre-edge baseline was subtracted from the normalized spectra. Energy calibration was performed using an HOPG reference sample. The HOPG C $1s \rightarrow \pi^*_{C=C}$ transition was assigned an energy of 285.5 eV according to the literature value.[21] The simultaneous measurement of a graphite-coated gold grid allowed the calibration of the photon energy with respect to the HOPG sample. The error in the energy calibration is expected to be within ± 0.5 eV. Charge compensation was carried out by directing low-energy electrons from an electron gun onto the sample surface.

5.2 Theory

In depth discussion on the theory can be found in the literature for the interested reader.[17, 22] The absorption of X-rays from a material surface leads to the creation of photoelectrons and Auger electrons. The number of Auger electrons per second generated at a depth z within an increment of dz can be expressed by

$$N_e \, dz = I_o \, A_o \, \mu_E \, dz \qquad (5.1)$$

where I_o is the photon flux density and A_o is the area illuminated by the incident X-rays. The X-ray absorption coefficient, μ_E, is related to the absorption cross section, σ_E (cm^2/atom), the carbon volume density of the sample, $n_v(z)$ (atoms/cm^3), and the angle of incidence, θ.[22]

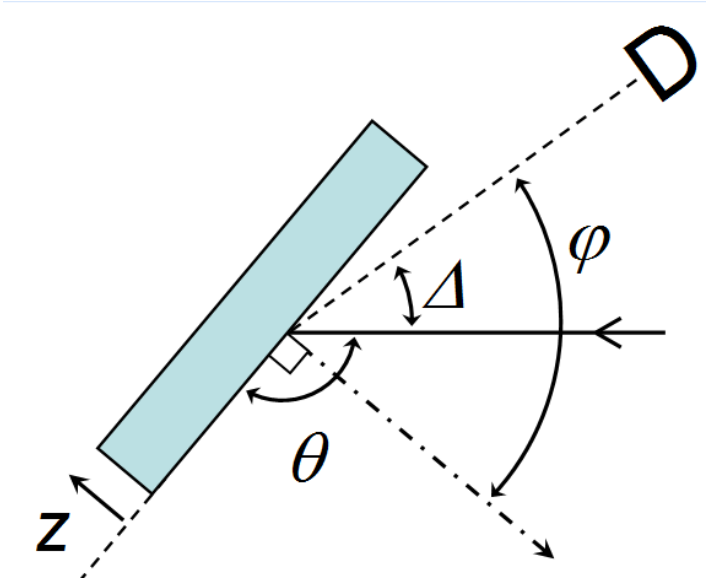

Figure 5.1 Schematic of the experimental geometry. D is the channeltron detector, which is at a fixed angle Δ with respect to the incident X-ray beam. The sample is rotated about an axis normal to the plane of the figure to vary the angle of incidence θ and the emission angle φ.

$$\mu_E = n_v(z)\,\sigma_E / \sin(\theta) \quad (5.2)$$

The volume density n_v of carbon atoms can be determined from the carbon atom mass density of the material, $\rho_m(z)$ (g/cm^3), through the relation

$$n_v(z) = \rho_m(z)\, N_A / A_r \quad (5.3)$$

where N_A is Avagagro's number and A_r is the atomic weight of carbon. The number of electrons at a sample depth z that are able to escape the surface can be described by

$$I = I_o e^{-z/\lambda^*} \quad (5.4)$$

where λ* is the effective EED. By integrating eq 5.1, the number of Auger electrons created throughout the sampling depth which escapes the surface to the detector with solid angle Ω is

$$I_a = \frac{\Omega}{4\pi}\frac{I_o A_o}{\sin(\theta)}\int_0^\infty n_v(z)\sigma_E e^{-(z/[\lambda\cos(\varphi)\cos(\Delta)]}dz \quad (5.5)$$

where λ is the EED.

The absorption cross section for transition to a σ* or a π* final state, however, not only depends on the energy, but also on the orientation of bonds with respect to the electric field of the polarized X-ray beam such that

$$\sigma_E = \sigma(hv)cos^2\delta \quad (5.6)$$

where δ is the angle between the transition dipole moment (TDM) of the final orbital state and the electric field vector.[22] In the case of phenyl rings, the direction of the π* orbital is perpendicular to the plane of the phenyl ring. When the bond orientation exhibits azimuthal symmetry about the surface normal, Eq 5.6 can be expressed in terms of the X-ray incidence angel and the orbital tilt angle, α, as follows:

$$\sigma_E \propto P\,cos^2\theta\left(1-\frac{3}{2}sin^2\alpha\right)+\frac{1}{2}sin^2\alpha \quad (5.7)$$

where P is the degree of polarization of the X-ray beam. The notation can be simplified by defining the bond orientation parameter, S as

$$S = 1-\frac{3}{2}\langle sin^2\alpha\rangle \quad (5.8)$$

where $\langle sin^2\alpha\rangle$ is the average $\sin^2\alpha$ over all the bonds. Thus,

$$\sigma_E = \sigma(hv)\left(PScos^2\theta + \frac{1-S}{3}\right) \quad (5.9)$$

and Eq 5.4 can re-expressed to take into account the bond orientation

$$I_a = \frac{\Omega}{4\pi}\frac{I_o A_o}{\sin(\theta)}\int_0^\infty \mathrm{n_v(z)}\sigma(hv)\mathrm{e}^{-(\mathrm{z}/[\lambda\cos(\varphi)\cos(\Delta)]}\left(PScos^2\theta + \frac{1-S}{3}\right)\mathrm{dz} \quad (5.10)$$

Note that at energies far above the absorption edge, the photoelectron is ejected into the continuum and any dependence on bond orientation is lost such that

$$\sigma_E = \sigma_{cont}(hv) \quad (5.11)$$

The intensity at 320 eV can then be simply expressed by

$$I_{320} = \frac{\Omega}{4\pi}\frac{I_o A_o}{\sin(\theta)}\sigma_{cont}(320eV)\int_0^\infty \mathrm{n_v(z)}\mathrm{e}^{-(\mathrm{z}/[\lambda\cos(\varphi)\cos(\Delta)]}\mathrm{dz} \quad (5.12)$$

The expression can be simplified further assuming a constant carbon density as a function of depth.

$$I_{320} = \frac{\Omega}{4\pi}\frac{I_o A_o}{\sin(\theta)}\sigma_{cont}(320eV)\mathrm{n_v}\lambda\cos(\varphi)\cos(\Delta) \quad (5.13)$$

By plotting $\left(\frac{I_{320}}{I_o}\frac{sin\theta}{cos\Delta}\right)$ vs $\cos(\varphi)$, the slope should be constant and proportional to the EED. However to explain the attenuation from a signal coming from a layer buried beneath a surface layer, a two layer system must be modeled. Using a 2nd material layer with thickness t less than the EED and carbon volume density $\mathrm{n_{2,v}}$ on top of a material with carbon volume density $\mathrm{n_{1,v}}$, Eq 5.12 becomes

$$I_{320} = \frac{\Omega}{4\pi}\frac{I_o A_o}{\sin(\theta)}\sigma_{cont}(320eV)\mathrm{n_{1,v}}\lambda\cos(\varphi)\cos(\Delta)\mathrm{e}^{-\frac{\mathrm{t}}{\lambda\cos(\varphi)\cos(\Delta)}} + \frac{\Omega}{4\pi}\frac{I_o A_o}{\sin(\theta)}\sigma_{cont}(320eV)\mathrm{n_{2,v}}\lambda\cos(\varphi)\cos(\Delta) - \frac{\Omega}{4\pi}\frac{I_o A_o}{\sin(\theta)}\sigma_{cont}(320eV)\mathrm{n_{2,v}}\lambda\cos(\varphi)\cos(\Delta)\mathrm{e}^{-\frac{\mathrm{t}}{\lambda\cos(\varphi)\cos(\Delta)}} \quad (5.14)$$

The postedge intensity can be expressed in terms of the signal from the top layer, the attenuated lower layer, while subtracting the signal from the doubly counted upper layer.

5.3 Results and Discussion

Four brushes of PS-*b*-PTFEA were synthesized in preparation for this study. XRR was carried out on the films after the polymerization of each block to measure

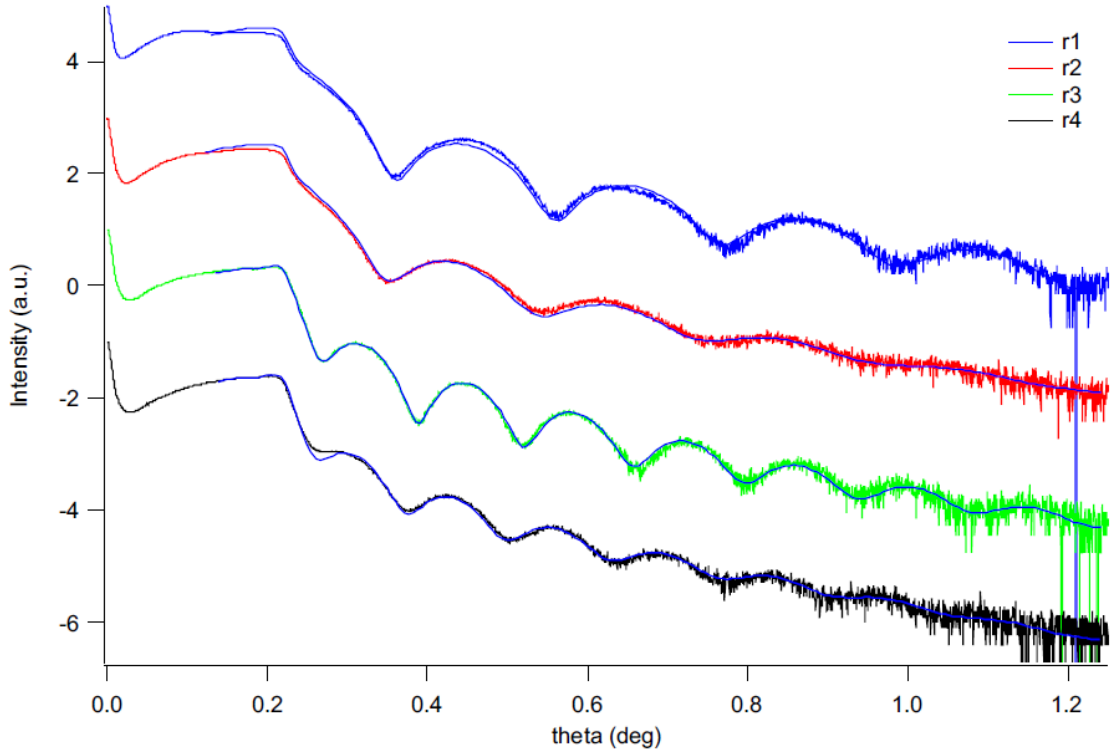

Figure 5.2 X-ray reflectivity measurements of the four block copolymer brushes prepared to determine the thicknesses of the PS and PTFEA layers.

Table 5.1 Thickness measurements of the polystyrene and poly(trifluoroethyl acrylate) layers.

Sample	Polystyrene	PTFEA
R1	18.4 nm	1.37 nm
R2	18.6 nm	1.64 nm
R3	28.9 nm	1.42 nm
R4	29.5 nm	1.77 nm

the thickness of each layer. Figure 5.2 shows the XRR spectra and fits of the four samples, and the modeled thickness of the PS and PTFEA layers are given in Table 5.1. For this study, the sample with the thinnest PTFEA layer, R1, was used to determine the EED for NEXAFS. High resolution C 1s XPS also confirmed the presence of the PTFEA layer, as seen in Figure 5.3. The polymer brush r.m.s. roughness was found to be 0.42 nm as measured by AFM, showing the sample surface is very flat.

NEXAFS spectra at X-ray incident angles between 20° and 125° of the R1 diblock copolymer brush are shown in Figure 5.4. The spectra were normalized to the incident X-ray beam intensity and a linear background was subtracted. Given the thickness, t, of the PTFEA layer is known from XRR, Eq 5.14 can be re-expressed as

$$\frac{I_{320}\sin\theta}{I_o\cos\Delta} = A\left[(1-y)\mathrm{e}^{-\frac{\mathrm{h}}{\cos(\varphi)}} + \mathrm{y}\right]\cos\varphi \qquad (5.15)$$

where $h = t/\left(\lambda\cos(\Delta)\right)$ and $y = \frac{\mathrm{n}_{2,\mathrm{v}}}{\mathrm{n}_{1,\mathrm{v}}}$ and A is a proportionality constant. By fitting the constants A, h, and y, the EED λ can be determined.

The postedge intensity was used to determine the best fit values for h and y, using Eq 5.15. Figure 5.5 shows a plot of $\frac{I_{320}\sin\theta}{I_o\cos\Delta}$ vs $\cos\varphi$. Values of h = 0.90 and y = 0.285 produced the best fit data, and an EED of $\lambda = 1.89$ nm. This value is close to the value of 1.95 nm determine by Kramer *et al.*[17] Genzer and coworkers found an EED of 2.43 nm.[16] It has been argued, however, that the discrepancy could be due to some contamination which might be present at surface, increasing the measured EED that they determined. As our measured EED is slightly lower than the 1.95 nm measured by Kramer's group, we assume the discrepancy is also due to the contamination layer they had observed in their system which is absent in ours.

To check the accuracy of our measurement, analysis using the postedge normalized C1s→$\pi^*_{C=C}$ transition peak intensity found at 285.5 eV from the buried PS

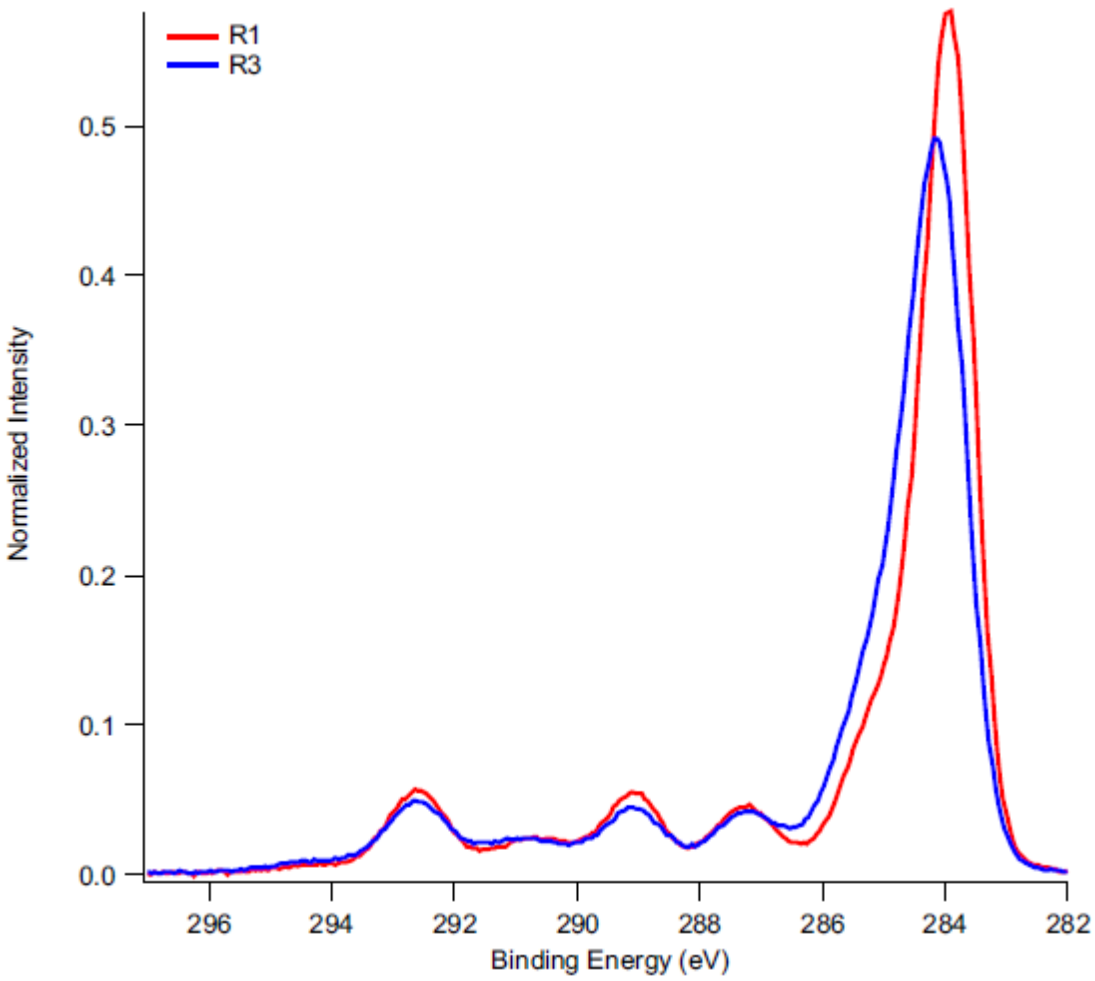

Figure 5.3 High resolution XPS C 1s spectra of the R1 and R3 polymer brushes taken at an emission angle of 0°. The signal at ~293 eV is in good agreement with the characteristic binding energy of the $–CF_3$ group from the PTFEA layer.

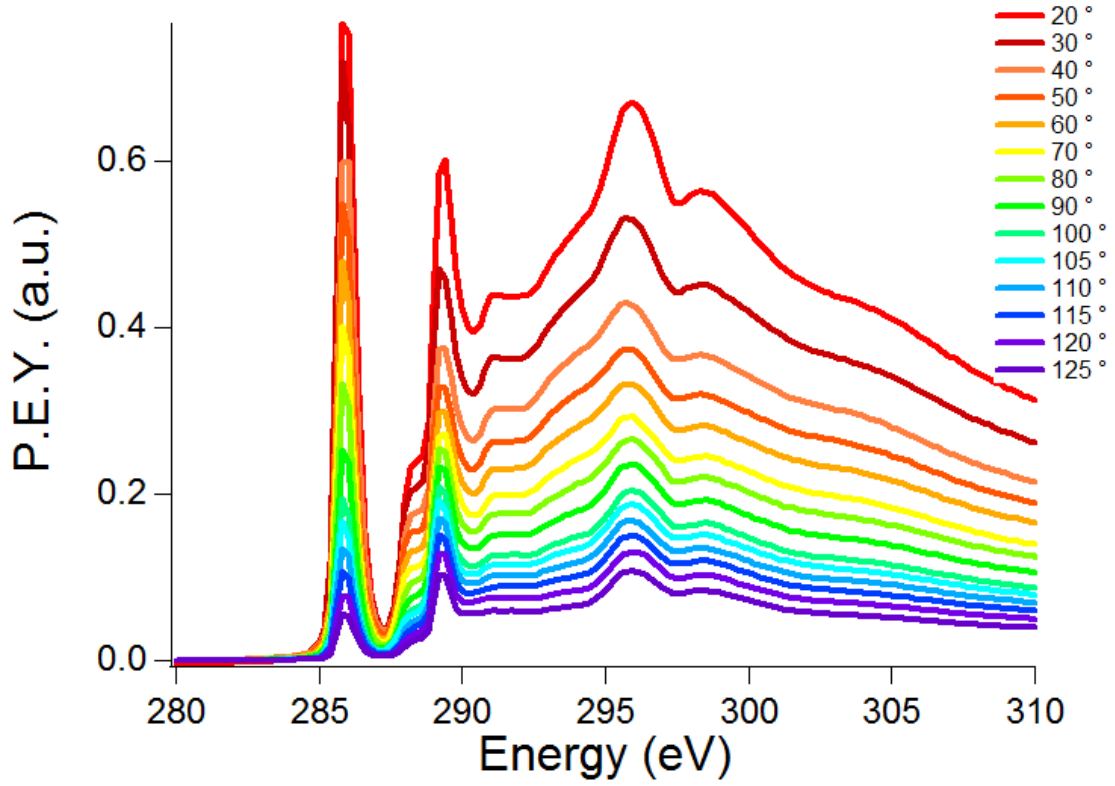

Figure 5.4 Normalized NEXAFS C K-edge spectra of the R1 diblock copolymer brush.

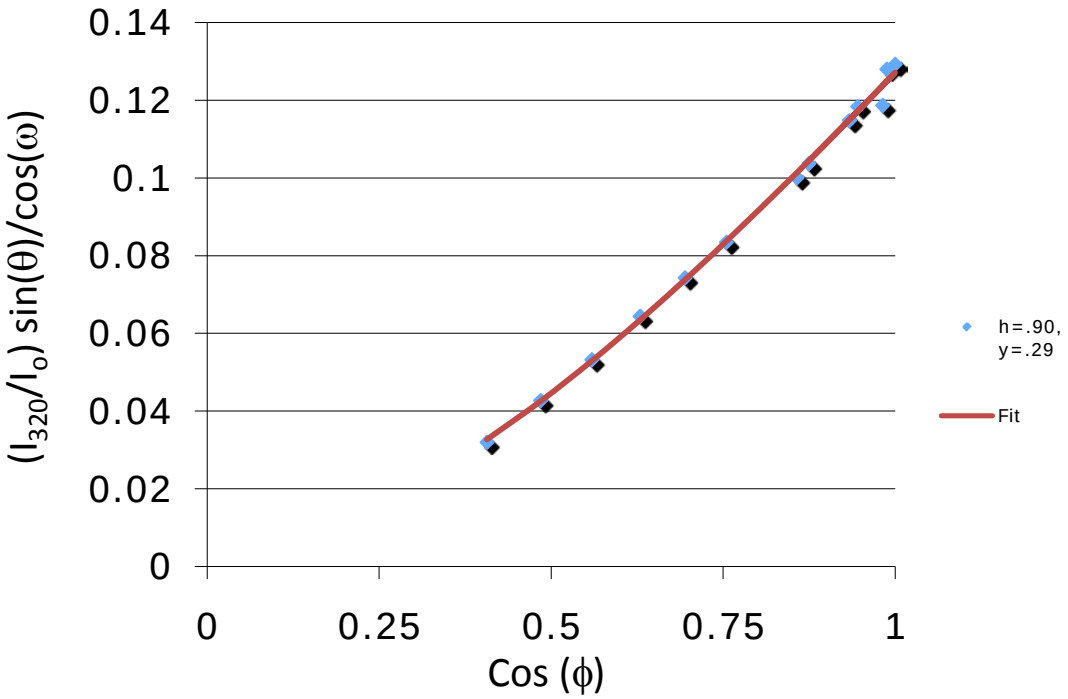

Figure 5.5 Postedge intensity fitted to Eq 5.14.

layer was also done. As this peak lies at an energy that is not far above the absorption edge, Eq 5.10 must be used to fit the data. To begin, the order parameter S was first calculated. Figure 5.6 shows a plot of the C1s→$\pi^*_{C=C}$ transition vs $\cos^2\theta$. The order parameter value of S = 0.074 was calculated using a method described elsewhere in literature.[15] As S is very close to zero, Eq 5.10 can be reduced to a form similar to Eq 5.15. Plotting the C1s→$\pi^*_{C=C}$ peak intensity vs $\cos\varphi$ and fitting h and y to the data (Figure 5.7) produced an h value equal to 0.9, matching what we had seen from the postedge analysis done earlier.

To confirm no surface contamination was present on our sample, analysis of the postedge normalized C1s→$\sigma^*_{C=O}$ transition peak intensity was done. This particular transition can only occur from the top PTFEMA layer as styrene does not possess this bond. So by trying to fit an h value to the C1s→$\sigma^*_{C=O}$ transition peaks, we can determine if any contamination is present at the surface. Figure 5.8 shows the peak intensity vs $\cos\varphi$. The plot also shows the predicted values of a pure PTFEA surface. An h value of 0 produces the best fit curve to the experimental data, which suggests that this system is free of any surface contamination.

5.4 Conclusion

NEXAFS spectroscopy was done on diblock copolymer brushes to more accurately determine the EED for NEXAFS. A very thin block of poly(trifluoroethyl acrylate) was grown on top of polystyrene using nitroxide mediated controlled radical polymerization. Our results showed an EED of 1.89 nm, comparable to that seen previously in literature. However, we believe our system yielded a more accurate measurement of the EED as our surface didn't suffer from the roughness or contamination seen in other studies. Using this information, compositional depth profile measurements can be done with sub-nanometer resolution which is essential for characterizing and fabricating custom made surfaces. NEXAFS depth profiling

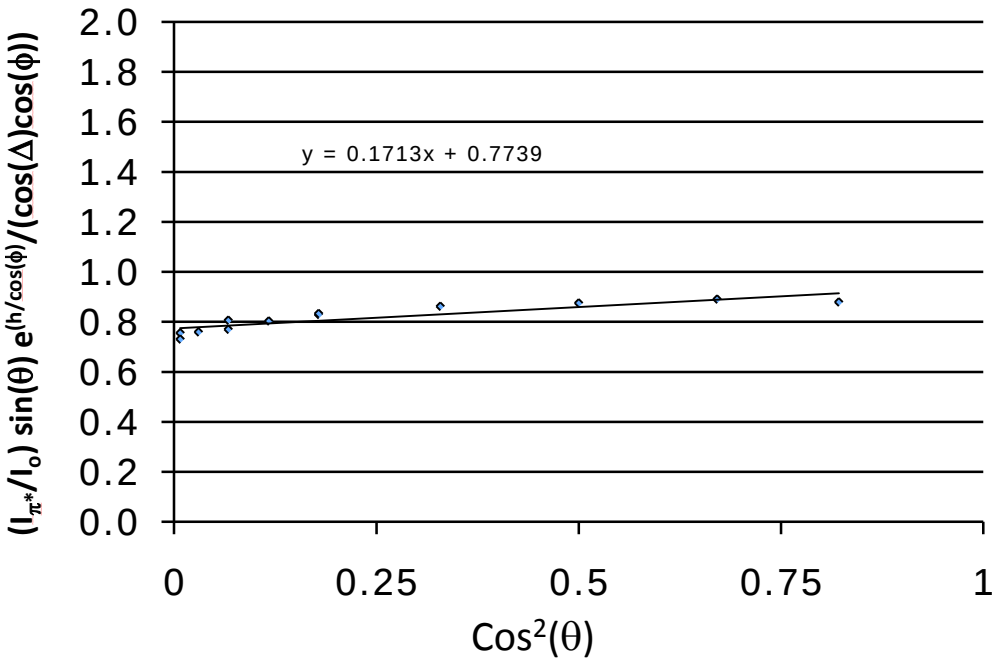

Figure 5.6 Plot of the corrected C1s→$\pi^*_{C=C}$ peak intensity vs $\cos^2\theta$. As the slope of the fit is close to zero, the phenyl groups from the polystyrene layer exhibit no orientational order.

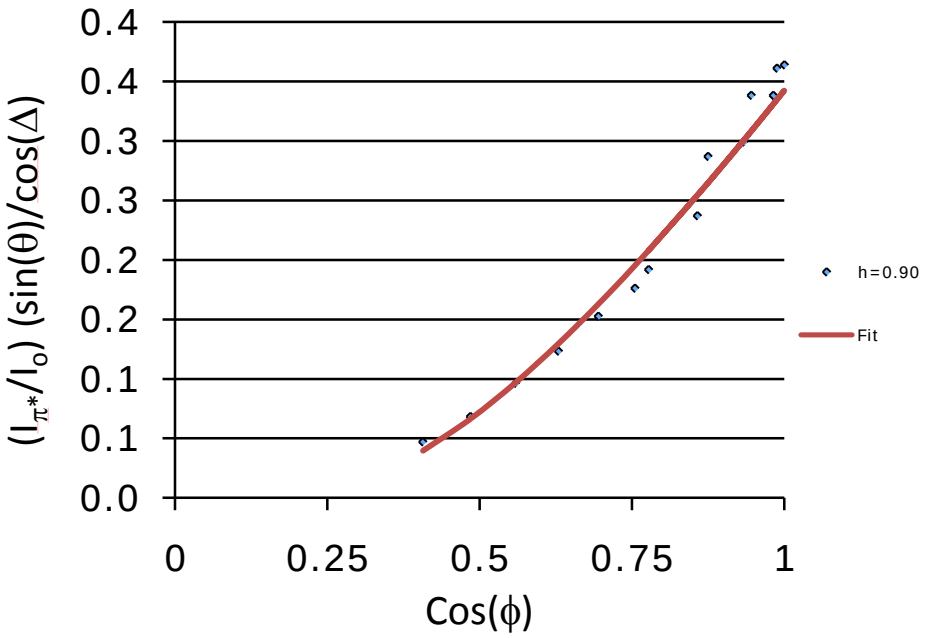

Figure 5.7 The C1s→$\pi^*_{C=C}$ peak intensity vs cos φ. Using an h value of 0.9 gives the best fit curve to the data.

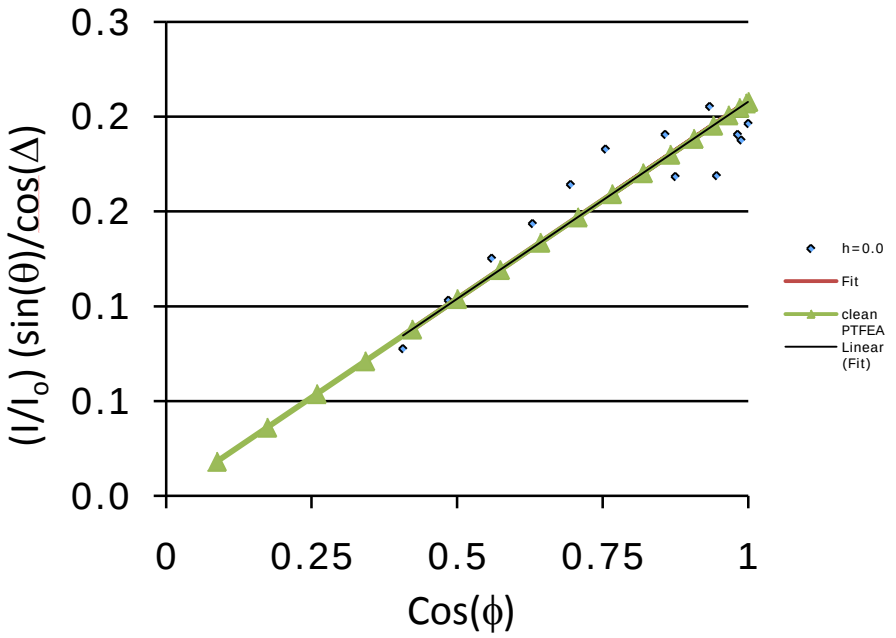

Figure 5.8 The C1s→σ*$_{C=O}$ peak intensity vs cos φ and the predicted values of a clean PTFEA surface.

could then be used as a compliment to techniques such as AFM to characterize what is at the surface such as in samples seen in chapter 3 in addition to block copolymers used in anti-fouling research and block copolymer self-assembly work.

5.5 Acknowledgements

The National Science Foundation (Grant DMR-0518785) is gratefully acknowledged for funding the project. Use of the National Synchrotron Light Source, Brookhaven National Laboratory, was supported by the U. S. Department of Energy Office of Science, Office of Basic Energy Sciences. M. P. would like to thank Prof. Sitaraman Krishnan from Clarkson University and Michael Dimitriou from UCSB for their help with the NEXAFS data analysis. The Cornell Center for Materials Research and Cornell Nanoscale Science & Technology Facility are also thanked for use of their facilities.

REFERENCES

1. Yu, Y.-J.; Kim, J.-G.; Boo, J.-H., *Journal of Materials Science Letters* **2002,** *21* (12), 951-953.

2. Krishnan, S.; Weinman, C. J.; Ober, C. K., *Journal of Materials Chemistry* **2008,** *18* (29), 3405-3413.

3. Li, G.; Cheng, G.; Xue, H.; Chen, S.; Zhang, F.; Jiang, S., *Biomaterials* **2008,** *29*, 4592-4597.

4. Glinel, K.; Jonas, A. M.; Jouenne, T.; Leprince, J.; Galas, L.; Huck, W. T. S., *Bioconjugate Chem.* **2009,** *20*, 71-77.

5. Senaratne, W.; Andruzzi, L.; Ober, C. K., *Biomacromolecules* **2005,** *6* (5), 2427.

6. Okano, T.; Yamada, N.; Okuhara, M.; Sakai, H.; Sakurai, Y., *Biomaterials* **1995,** *16* (4), 297-303.

7. Facchetti, A.; Yoon, M.-H.; Marks, T. J., *Advanced Materials* **2005,** *17* (14), 1705-1725.

8. Park, S.; Lee, D. H.; Xu, J.; Kim, B.; Hong, S. W.; Jeong, U.; Xu, T.; Russell, T. P., *Science* **2009,** *323* (5917), 1030-1033.

9. Advincula, R. C.; Brittain, W. J.; Caster, K. C.; Ruhe, J., *Polymer Brushes*. WILEY-VCH Verlag GmbH & Co.: Weinheim: 2004.

10. Stuart, M. A. C.; Huck, W. T. S.; Genzer, J.; Muller, M.; Ober, C.; Stamm, M.; Sukhorukov, G. B.; Szleifer, I.; Tsukruk, V. V.; Urban, M.; Winnik, F.; Zauscher, S.; Luzinov, I.; Minko, S., *Nat Mater 9* (2), 101-113.

11. Cross, E. M.; McCarthy, T. J., *Macromolecules* **1990,** *23* (17), 3916-3922.

12. Tyler, B. J.; Castner, D. G.; Ratner, B. D., *Surface and Interface Analysis* **1989,** *14* (8), 443-450.

13. Senshu, K.; Yamashita, S.; Mori, H.; Ito, M.; Hirao, A.; Nakahama, S., *Langmuir* **1999,** *15* (5), 1754-1762.

14. Beamson, G.; Alexander, M. R., *Surface and Interface Analysis* **2004,** *36* (4), 323-333.

15. Paik, M. Y.; Krishnan, S.; You, F.; Li, X.; Hexemer, A.; Ando, Y.; Kang, S. H.; Fischer, D. A.; Kramer, E. J.; Ober, C. K., *Langmuir* **2007,** *23* (9), 5110-5119.

16. Genzer, J.; Kramer, E. J.; Fischer, D. A., *Journal of Applied Physics* **2002,** *92* (12), 7070-7079.

17. Sohn, K. E.; Dimitriou, M. D.; Genzer, J.; Fischer, D. A.; Hawker, C. J.; Kramer, E. J., *Langmuir* **2009,** *25* (11), 6341-6348.

18. Benoit, D.; Chaplinski, V.; Braslau, R.; Hawker, C. J., *Journal of the American Chemical Society* **1999,** *121* (16), 3904-3920.

19. Bothe, M.; Schmidt-Naake, G., *Macromolecular Rapid Communications* **2003,** *24* (10), 609-613.

20. Toney, M. F.; Mate, C. M.; Leach, K. A.; Pocker, D. J., *Colloid Interface Sci.* **2000,** *225*, 219-226.

21. Rosenberg, R. A.; Love, P. J.; Rehn, V., *Physical Review B* **1986,** *33* (6), 4034.

22. Stöhr, J., *NEXAFS Spectroscopy*. Springer-Verlag: Berlin/Heidelberg, 1992.